DESIGN AND CHARACTERIZATION OF A VARIABLE STIFFNESS PROSTHESIS FOR BILATERAL TRANSTIBIAL AMPUTEE SPRINTERS

by

AINHOA MURILLO IRAOLA
4509129

MASTER OF SCIENCE THESIS
in MSc Mechanical Engineering
Track Biomechanical Design
Profile Sports Engineering

at **Delft University of Technology**

to be defended publicly on October, 2018

Supervisors: **Prof. dr. Frans C. T. van der Helm** TU Delft / BioMechanical Engineering
Dr.ir. Otto K. Bergsma TU Delft /Aerospace Structures and Materials
Dr. Daan Bregman TU Delft / Coordinator Sports Engineering

TU Delft Delft University of Technology

ACKNOWLEDGEMENTS

This work would not have been possible without the help and supervision of Prof. Dr. van der Helm, Dr. Ir. Bergsma, and Dr. Bregman. I would like to thank Prof. Dr. van der Helm for his valuable feedback, and for directing my project in the right direction. I would like to thank Dr. Ir. Bergsma for his contagious enthusiasm, for sharing his knowledge with me, and for patiently listening and evaluating my suggestions and results. I would like to thank Dr. Bregman for his guidance, for helping me set the right steps to follow, and for listening and supporting my ideas and objectives.

I would also like to thank the people in the DASML lab, mostly Victor and Gertjan, who made the manufacturing and testing of my prototype possible. Always with a smile, they were willing to help and share their expertise with me.

My special thanks goes to my parents, who supported every single academic choice I made during these university years. No serán suficientes todas las veces que os pueda dar las gracias, ni en un millón de vidas, por apoyarme y por creer en mí y en mi felicidad. En este millón de vidas, tened por seguro que os elegiría siempre a vosotros, con los ojos cerrados y el corazón bien abierto. Another big thanks goes for my friends: mi Familia, 65 is life, my flatmates, Punch, and my friends in Spain. They are always there to listen, to support, and to encourage me, no matter the time, no matter the distance. Finally, the biggest thanks goes to Giovanni. Mil gracias por apoyarme y motivarme cada día, por hacerme ver el cielo azul detrás de las nubes, por creer en mí más que yo, y por ansiar mi felicidad tanto como yo. Eres mi mejor suerte y mi mayor triunfo.

CONTENTS

List of Figures

List of Tables

List of Symbols and Abbreviations

Acronyms

β	Shin angle.
γ	Difference between shin and drive angle.
ϕ	Drive angle.
P_A	Point of Force Application.
P_C	Prosthesis-Ground Contact Point.
BTA	Bilateral Transtibial Amputee.
CAD	Computer Aided Design.
CFRP	Carbon Fibre Reinforced Polymer.
CoM	Centre of Mass.
EI	Bending Stiffness.
FEM	Finite Element Method.
GRF	Ground Reaction Force.
I	Area Moment of Inertia.
RP	Running Prosthesis.
TU	Technische Universiteit.

ABSTRACT

The purpose of this thesis project is to design a new concept of sprinting prosthesis to enhance the acceleration phase performance of bilateral transtibial amputees (BTAs) competing in sprinting races. Amputee sprinters are hampered in the acceleration phase of a sprint race by the compliance of their prostheses. Increased contact times, and small and too vertical ground reaction forces limit the acceleration performance of BTAs. A variable stiffness prosthesis, with a higher stiffness at the initial steps of the acceleration phase, would reduce contact times and increase forward propulsion. A new variable stiffness design is proposed in this report. A prototype of this new design is created and characterized by retrieving the stiffness matrices and ellipses. Ottobock's 1E90 prosthesis is also characterized, and the results are compared. For this, a new testing methodology to obtain the stiffness ellipses of running prostheses (RPs) is proposed.

1

INTRODUCTION

Traditionally the main focus of sport science research was on able-bodied athletes and competitions. Lately a research centered on disable-bodied athletes is increasing, aimed at providing handicapped people with the required technology to participate in sports, both recreationally and professionally [1]. Moreover, an important growing area of research involves maximizing the performance of professional disable-bodied athletes at top level competitions such as the Paralympic Games [2, 3].

Different kinds of handicapped athletes take part in the Paralympic Games, divided in five disability groups: spinal injury, amputee, visually impaired, cerebral palsy and others [2]. Amputee athletes, more specifically athletes with a lower limb amputation, are becoming an important area of research for sport scientists [3]. Lower limb amputations can either be transfemoral (above knee) or transtibial (below knee), and can happen in one leg (unilateral) or in both legs (bilateral). All these are represented in Figure 1.1.

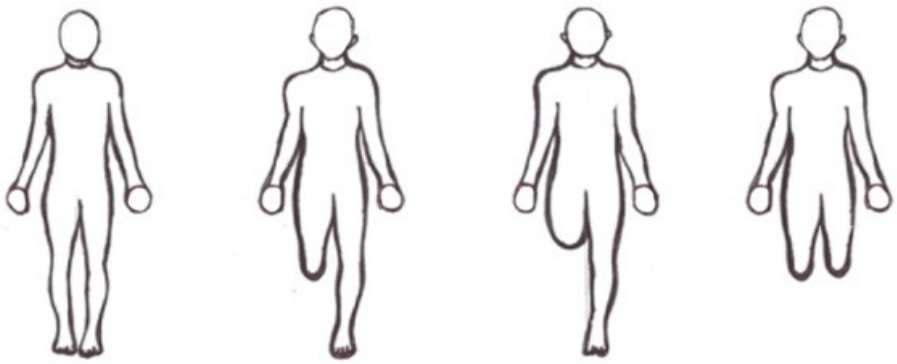

Figure 1.1: From left to right: representation of an able-bodied, a unilateral transtibial amputee, a unilateral transfemoral amputee and a bilateral transtibial amputee.

Lower limb prostheses are used by amputees to walk and to run, but RPs differ from walking prostheses. Unlike many non-sporting prostheses on the market, running prostheses do not include active systems due to regulations imposed by the Paralympic Committee [4]. Such prostheses are shown in Figure 1.2 below.

Figure 1.2: Two transtibial amputee athletes wearing running prostheses.

1.1. RUNNING PROSTHESES - INITIAL OVERVIEW

RPs are passive carbon fibre reinforced polymer (CFRP) composite prostheses with a spring-like behavior [5]. When the RP hits the ground and the body weight moves over it, the RP is compressed and potential energy is stored. When the body weight is lifted off, the RP is decompressed and the energy is released to the center of mass in form of kinetic energy, accelerating it. This mechanism provides the athlete with an effective push-off [1, 5].

Stiffness is one of the most important factors that determine the performance of amputee athletes. Stiffness, K, is the resistance of an elastic object to deflection, as defined in Equation 1.1. The inverse of stiffness is the compliance.

$$K = \frac{\Delta F}{\Delta L} \quad \left[\frac{N}{mm}\right] \tag{1.1}$$

An increasing stiffness leads to a shorter contact time and a larger ground reaction force (GRF) peak but lower energy storage under the same applied force [6, 7]. Since the stiffness is related with the change in length of the prosthesis, a compliant prosthesis will compress more and the contact time will increase, what limits maximum running speed. If, on the contrary, stiffness is increased, less compression of the prosthesis will lead to shorter contact times, allowing for a faster maximum running speed. However, an excessive increase in stiffness may carry an energetic cost [1]. This can be seen in Figure 1.3, which shows the dependency of energy storage on stiffness. More force is needed to store the same amount of energy in a stiffer prosthesis than in a more compliant one.

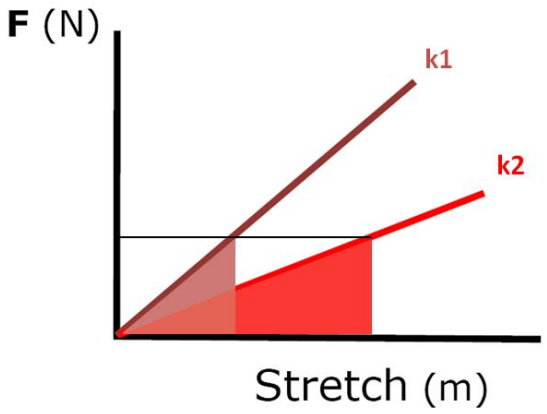

Figure 1.3: The energy stored on the prosthesis is the area under the stiffness curve, and depends on the stiffness and applied force. If the same force is applied on two prostheses with different stiffness, the more compliant prosthesis (k2) will store more energy.

The bending stiffness of the prosthesis is directly related with the laminate thickness. The area moment of inertia, I, of a rectangular section with length h an width b, is seen in Equation 1.2, and determines the bending stiffness (EI) of the prosthesis. It can be observed that the bending stiffness is then proportional to the third power of the thickness.

$$I = \frac{bh^3}{12} \tag{1.2}$$

The stiffness of the prosthesis can be tuned by changing the lamination of the prosthesis, i.e. the laminate thickness, fiber orientation and laminate lay up. Running prostheses are currently laminated with carbon fiber, which is a lightweight, flexible material that provides RPs with exceptional strength to weight characteristics. It also transforms the prostheses into an energy return system and provides them with great fatigue resistance characteristics [8]. The fiber is the primary load carrying element of the composite material, which is only strong and stiff in the direction of the fibers. 0^o plies react to axial loads, $\pm 45^o$ plies react to shear loads, and 90^o plies react to side loads. Therefore, 0^o plies are needed to provide the prosthesis with bending (vertical) stiffness, while $\pm 45^o$ plies are needed to increase torsional (medio-lateral) stiffness to avoid unwanted torsion of the prosthesis. Finally, the laminate lay up refers to the stacking sequence of the plies. The further the ply is located from the middle ply, the bigger its influence on the laminate bending behavior will be.

Different stiffness categories exist for each prosthetic model, and each athlete wears a specific category depending on his weight and physical state: heavier and stronger athletes will wear a higher category, which means a higher stiffness. The different stiffness categories with their corresponding suggested body weight (BW) and bending stiffness for short distance running for the RP 1E90 from Ottobock are shown in Table 1.1.

Stiffness Category	Stiffness [N/mm]	Body Weight [kg]
1	10.5	40-52
2	13.5	53-63
3	16.5	64-79
4	19.5	80-95
5	23.5	96-111
6	27.5	112-125

Table 1.1: Stiffness category recommendations for short distance running based on body weight. The bending stiffness values corresponding to each stiffness category are also shown [9].

This bending stiffness is measured on a static compression test, and is calculated as $k_y = f_y/u_y$. The vertical force, f_y, and displacement, u_y, are represented in Figure 1.4 below.

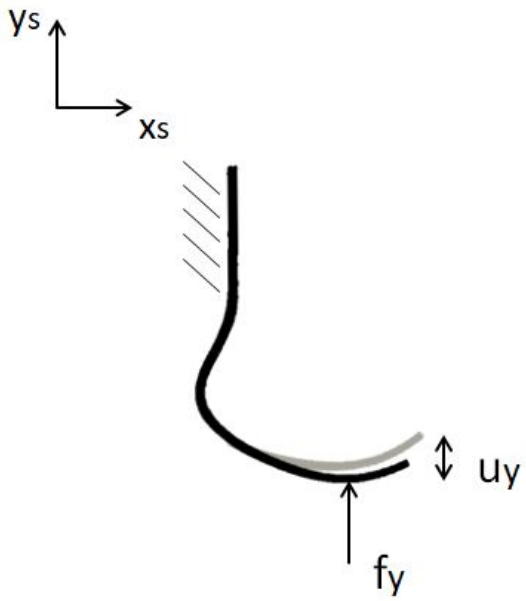

Figure 1.4: Representation of a static compression test used to measure the bending stiffness of the RP. The underformed prosthesis is shown in black. The deformed prosthesis after applying the vertical force, f_y, is shown in grey. The vertical displacement is represented as u_y. The global reference frame xy represents the sagittal plane.

With this method of calculating bending stiffness, only the component of the displacement on the direction of the force (u_y) is considered, but a normal component of this displacement (u_x) is also present. Thus, the relationship between the force and the displacement can be expressed by means of the stiffness matrix, as seen in Equation 1.1.

$$\begin{bmatrix} f_x \\ f_y \end{bmatrix} = \begin{bmatrix} k_{xx} & k_{xy} \\ k_{yx} & k_{yy} \end{bmatrix} \begin{bmatrix} u_x \\ u_y \end{bmatrix} \tag{1.3}$$

The behavior of current running prostheses can be better understood by calculating the stiffness matrix, which has not been calculated yet for any RP.

1.2. PROBLEM DESCRIPTION

Paralympic athletes, like Olympic athletes, take part in short and long sprint events. A 100 meters race is considered a short sprint event and consists of 3 performance phases: acceleration phase, maximum velocity phase, and deceleration phase. The acceleration phase refers to the first phase of a race, from the start until the maximum speed of the athlete is reached. The maximum velocity or steady state phase is the middle phase when the athlete runs at a constant velocity, which is the maximum velocity. And the deceleration phase is the last phase when the athlete slows down, decreasing the speed. The distribution of these phases depends on the sprinting ability of the athlete [10]. Mackala et al. found out that able bodied athletes showed approximately the following distribution in a 100 meters sprint: acceleration phase from 0 to 60 meters, maximal velocity phase from 60 to 80 meters, and deceleration phase from 80 to 100 meters. This differs for amputee sprinters. Hobara et al. showed that athletes running with prostheses spend 100% of the 100 meters race accelerating, which means that they never reach their maximum velocity. An approximation of the velocity profile for able-bodied and amputee athletes during a 100 meters race can be seen in Figure 1.5.

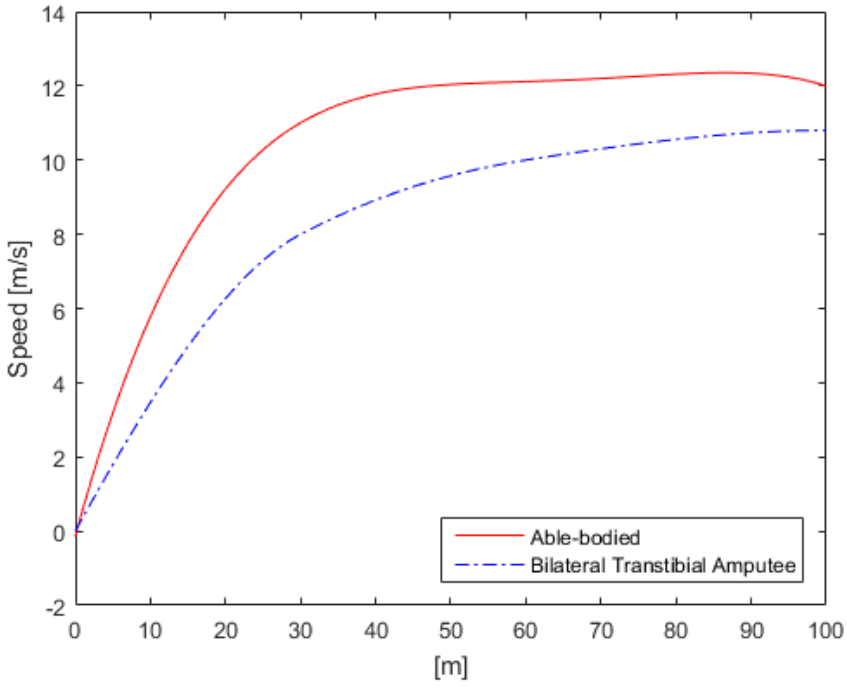

Figure 1.5: Approximation of the velocity profile in a 100 meters sprint for able-bodied and bilateral transtibial amputee athletes. The profile of the able-bodied corresponds to Usain Bolt's velocity during the final of the Beijing 2008 Olympics [11]. The velocity at every 10 meters interval was known; these points were fit with a 5th order polynomial. Since no data was found for bilateral transtibial amputees, an assumption was made based on Oscar Pistorius's 100 meters time.

This perceived disadvantage for amputee Paralympic athletes compared to Olympic athletes is confirmed looking at the 100 meters record times shown in Table 1.2. It can be observed that Olympic athletes are faster in 100 meters than Paralympic athletes.

	Olympic athletes	Paralympic athletes
Men	9.63 s	10.57 s
Women	10.62 s	12.79 s

Table 1.2: 100 meters male and female Olympic and Paralympic record times. The Paralympic record times belong to amputee athletes competing in categories T42 (unilateral transfemoral amputees), T43 (bilateral transtibial amputees) or T44 (unilateral transtibial amputees).

Looking at the results of the male finals of 100, 200 and 400 meters races in the Paralympics of London 2012, it can be noticed that differences in the amputation categories also lead to differences in performance. Firstly, in 100 meters three unilateral amputees were in the top three. Secondly, in 200 meters, three bilateral amputees made it to the top three. Finally, in 400 meters, two bilateral amputees (gold and silver medal) and one unilateral amputee (bronze medal) were in the top three [12]. For the case of able-bodied athletes, while for a 100 meters sprint the acceleration phase accounts for approximately 60% of the race and the steady state phase accounts for 20%, in a 400 meters race these phases account for 25% and 50% respectively [13]. The remaining percentages correspond to the deceleration phase of the sprint. From these numbers it can be deduced that the acceleration phase is the most important phase in a short sprint, while the steady state phase is more important in a log sprint. Unilateral amputees performing better than bilateral amputees in short sprints, and worse in long sprints, shows how RPs are not optimized for fast accelerations. On the contrary, due to their low weight and high energy return at higher speeds, they can be optimally used during the steady state phase of a race, where running economy plays a major role [13, 14].

In order to better understand the acceleration performance of amputee athletes, the performance predictors that ensure a fast acceleration should be analyzed. These performance predictors are the horizontal velocity of the centre of mass (CoM) of the athlete (which is defined as the product of stride frequency and stride length), short push-off durations (or contact times) and efficient GRFs (which should be high and oriented in the running direction) [15, 16]. Figure 1.6 shows the comparison of the block step performance of a BTA and able-bodied. This double amputee, compared to athletes with the same performance, had a slow horizontal CoM velocity at block clearance due to lower rear and front leg average resultant forces. This outcome can be reasoned by the fact that double amputees cannot take advantage of their prostheses at the start of the race, so the force on the blocks is exerted only by the proximal muscles [17]. This BTA also showed longer block times, as a result of the compliance of the RPs [17].

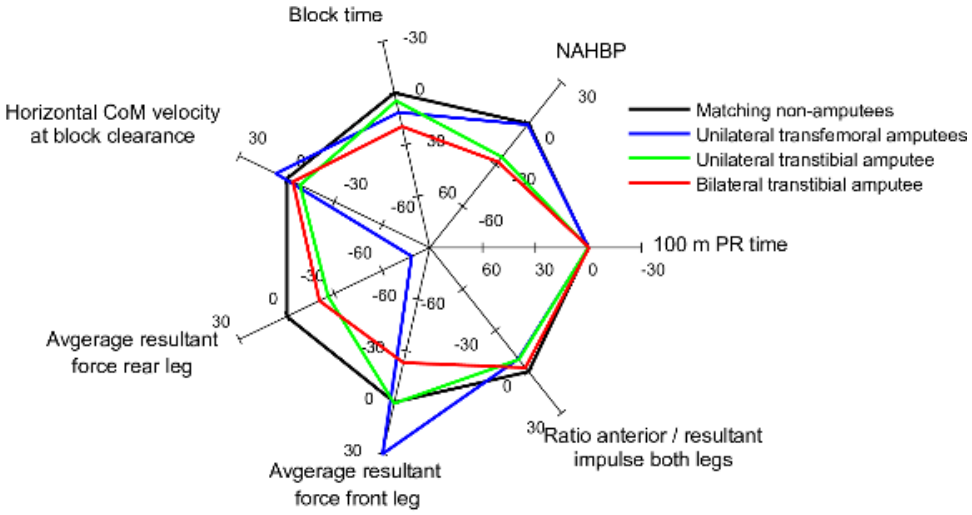

Figure 1.6: Radar chart representation of the relative difference between amputee athletes and matching controls. For each amputee athlete, three non-amputee athletes were matched with respect to their absolute 100m personal record. The results are displayed as relative differences (%) with respect to the matching controls. Positive axis directions were defined such that better performances in a certain parameter are outside of the zero difference (non-amputee) line and worse performances are inside that line. The parameters analysed were horizontal CoM velocity at block clearance, average resultant force in the rear leg, average resultant force in the front leg, ratio anterior/resultant impulse in both legs, normalized average horizontal block power and block time [18].

Figure 1.7 also shows that a BTA produces a smaller and more vertical force than able-bodied sprinters. It is also noticed that unilateral amputees develop more force with their unaffected leg than with their affected leg [17].

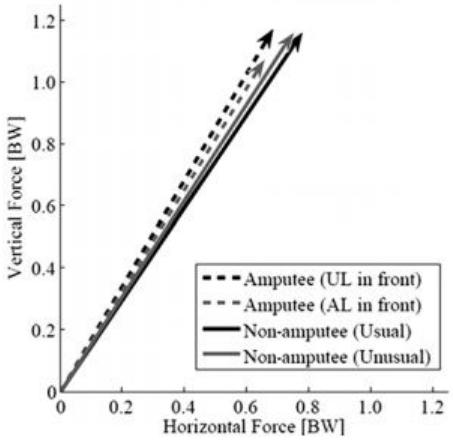

Figure 1.7: Mean combined resultant front block force vectors (average values) for unilateral amputee (n=9) and non-amputee (n=7) sprinters in unaffected leg (UL) versus affected leg (AL) in front and usual versus unusual, respectively. Right panel: mean resultant force vectors (average values) for virtual non-amputee (n=9), unilateral amputee with the unaffected leg in front (n=9) and virtual bilateral amputee (n=9) sprinters. Forces expressed as multiples of BW. [17].

Apart from creating lower GRFs in the running direction, amputees keep their CoM higher than able-bodied athletes during the first steps of the race.

Figure 1.8: The drive angle is the angle in the sagittal plane between the vertical axis and the vector pointing from the point of support to the CoM. It is measured as negative if clockwise, with the running direction towards the right. Thus, the drive angle depicted in this Figure is negative.

A more negative drive angle would result in higher horizontal GRF and, thus, more propulsion in the running direction [15].

Apart from an effective initial push-off, an effective landing after block clearance is also important to further develop forward acceleration [19]. Maintaining a big drive angle at the start is important to keep the contact point posterior to the CoM too. When the trunk is raised, resulting in a positive drive angle, the CoM position is shifted posterior to the contact point. This positive drive angle creates a horizontal braking force, which limits forward acceleration. This can be seen in Figure 1.9.

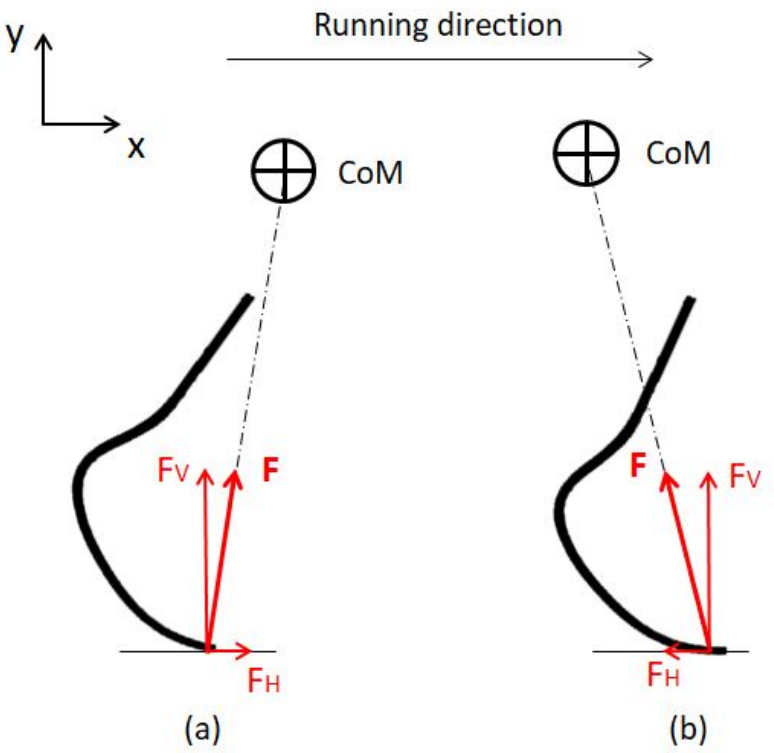

Figure 1.9: (a) If the CoM is anterior to the contact point, a positive horizontal force is obtained. (b) A horizontal negative force appears when the body CoM is shifted posterior to the contact point. This braking force limits forward acceleration.

The findings by Noorozi et al. about the inability of BTAs to reach maximum speed in a 100 meters sprint can be explained by the compliance of their RPs. The low stiffness of their prostheses leads to too long contact times and a small step frequency. Moreover, the compliance of their prostheses, together with the lack of proprioception, make amputee athletes feel like falling at the start of the race, inhibiting large and positive drive angles during the first steps of the sprint and, therefore, introducing the braking force shown in Figure 1.9. A stiffer prosthesis would result in shorter contact times and a larger step frequency, increasing initial acceleration. It is proven that an extra propulsion is supplied by a stiffer prosthesis [20]. Thus, increasing start step stiffness is also expected to result in larger drive angles and higher more efficient GRFs (directed towards the CoM).

Current prostheses work optimally after the first steps, providing a high energy return. Thus, the behavior of the prostheses in this phase should not be altered. As a result, in order to design a prosthesis that behaves optimally during the whole race, a variable stiffness prosthesis is needed. The stiffness during the first accelerating steps should be increased, but the stiffness for the steps after the CoM is shifted posterior to the initial ground-prosthesis contact point should remain unchanged.

Assuming that such a variable stiffness prosthesis helped BTAs reach their maximum speed after the first 60 meters, the velocity profile would look like that seen in Figure 1.10 below. This improvement would lead to a total 100 meters time reduction of 0.68s. Considering that the total time of a 100 meters sprint for male BTAs is now 10.57s, it would mean a decrease of 6.43% of the total time.

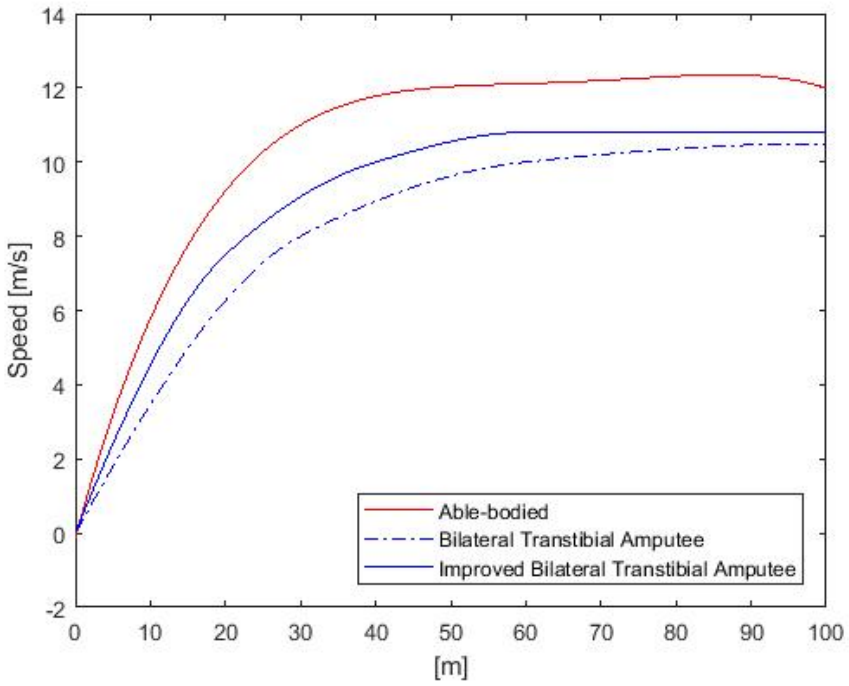

Figure 1.10: Approximation of the velocity profile in a 100 meters sprint for able-bodied and bilateral transtibial amputee athletes. The profile of the able-bodied (red) corresponds to Usain Bolt's velocity during the final of the Beijing 2008 Olympics [11]. The dotted blue line is assumption of BTAs velocity profile based on Oscar Pistorius's 100 meters time, considering that the maximum velocity is not reached by the athlete. The solid blue line represents the assumption of a BTAs velocity profile if maximum speed was reached at 50% of the total distance.

Regarding the state-of-the-art in the field of variable stiffness prostheses, an inverse RP was previously designed, which is represented in Figure 1.11. At the first steps of the race the contact point of the prosthesis is closer to the origin or stump. Due to the shortened distance to the origin, the prosthesis has a higher stiffness than at its furthest point, which is the contact point used when the body is upright. Therefore, the prosthesis has proved to be able to provide a variable stiffness. However, a negative (braking) horizontal GRF is created by this design, as shown in Figure 1.11. The determination of the direction of the GRF of this inverse prosthesis can be seen in Appendix A. The backwards pointing reaction force results in a rotational moment around the CoM. If the contact point is posterior to the position of the CoM ((a) in Figure 1.11), the rotational moment cannot be counteracted. This means that the inverse RP will rotate, giving the runner a non stable behavior, as this happens at the smallest force. If the contact point is anterior to the position of the CoM ((b) in Figure 1.11), this rotational moment might or might not be counteracted by gravity.

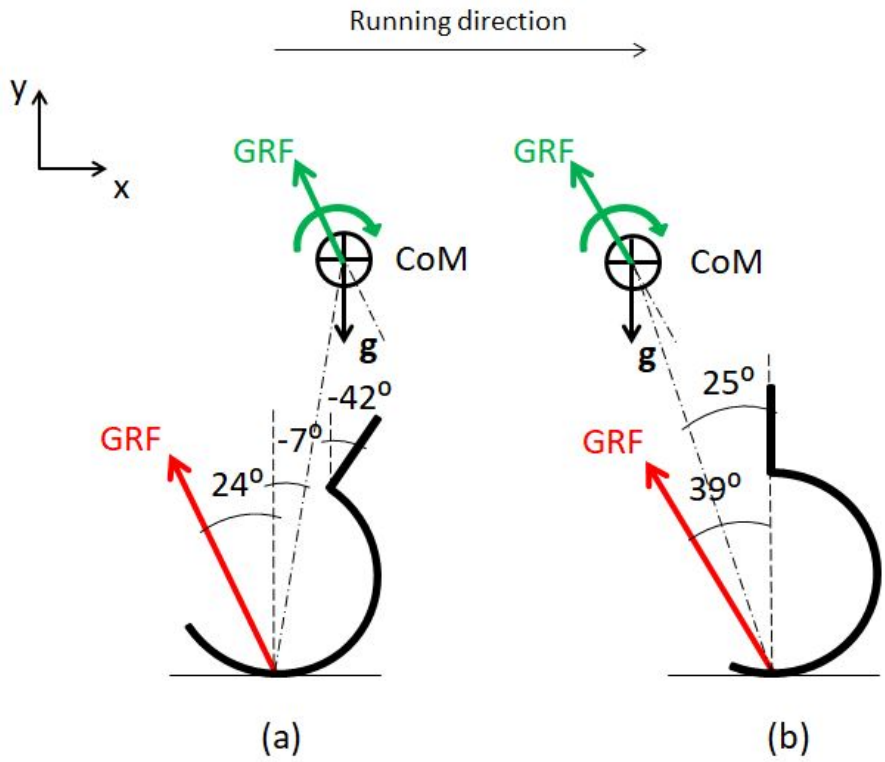

Figure 1.11: (a) If the CoM is positioned anterior to the contact point, the rotational moment created around the CoM cannot be counteracted, creating an unstable behavior for the athlete. (b) If the CoM is posterior to the contact point, the rotational moment might be counteracted by gravity.

This negative force returned by the inverse prosthesis creates a braking horizontal GRF, which hampers forward acceleration. Moreover, during the first steps of the acceleration phase where the CoM is positioned anterior to the contact point, the rotational moment created around the CoM cannot be counteracted, making the athlete fall forward.

Thus, a new variable stiffness design that ensures a positive horizontal GRF in the running direction is needed.

1.3. RESEARCH QUESTIONS

This project aims at designing a variable stiffness prosthesis that will enhance the acceleration performance of BTA sprinters, as well as developing a methodology to retrieve the stiffness matrix.

As a preliminary step, various research questions were formulated. The research questions that this research aims to answer are:

1. How do current prosthetic companies design their prostheses? Which methods do they follow? What is the validity of these methods?

2. Can the methods used by prosthetic companies be used to design a variable stiffness prostheses? If not, which other methods can be used to design a variable stiffness prosthesis?

3. Which are the advantages and disadvantages of the new design compared to previous variable stiffness designs? And compared to currently used prostheses?

4. How are athletes expected to perform with the new design?

5. How can the stiffness matrices of a prosthesis be experimentally measured? What is the validity of the methodology? What is the accuracy of the results?

1.4. THESIS OUTLINE

First of all, the RP design methodology used by a prosthetic leader company (which was learned during an internship at this company) is analyzed in Chapter 3. This analysis led to the creation of a new design methodology focused on designing a variable stiffness prostheses based on the kinematics given at the different steps. This new methodology is presented and proposed in Chapter 4. A Computer Aided Design (CAD) model of the new design is then created, and the Finite Element Method (FEM) results of the stiffness are compared to those of Ottobock's 1E90 in Chapter 5. After the FEM simulations, a prototype of the new design is created. The prototyping process is explained in Chapter 6. Together with the 1E90, the new design is tested on a static compression test bench to retrieve the stiffness matrices. Since the stiffness matrices of RPs have never been measured before, a new testing method was proposed for this aim. The results of the stiffness of the new design compared to the 1E90 are shown in Chapter 7. Finally, a discussion addressing the validity of the methodologies created and the usability of the new design proposed are addressed. Future steps on how to further develop these methodologies and the new design are also proposed.

2

METHODS

In this section the methods used for the design and characterization of a variable stiffness RP are shown.

2.1. DEFINITIONS

First of all, some definitions are introduced, which are needed in order to understand the research carried out.

2.1.1. COORDINATE SYSTEMS

Two different coordinate systems will be used in this report: the global reference frame, and the shin reference frame.

The global reference frame, xy in Figure 2.1, is a fixed reference frame with the y axis vertically oriented and the x axis horizontally oriented in the running direction.

The shin reference frame is a local reference frame, with the y axis aligned with the shank of the prosthesis, and is represented as $x_s y_s$ in Figure 2.1.

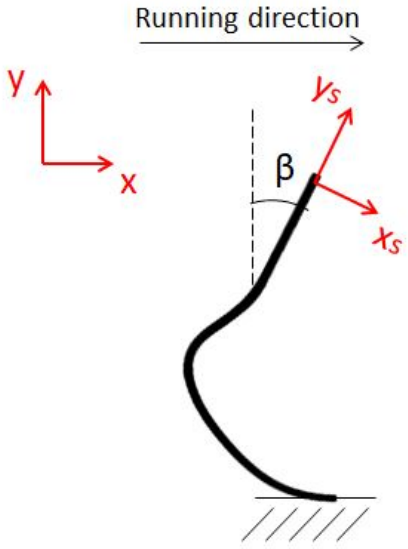

Figure 2.1: Definition of global and local reference frames (in red). The global reference frame, xy, represents the sagittal plane and the positive x axis is directed in the running direction. $x_s y_s$ is the local shin reference frame, with the positive y axis in the direction of the shank of the prosthesis.

2.1.2. KINEMATIC PARAMETERS

The kinematic parameters considered in this study are the shin angle and the drive angle, which are measured with respect to the global reference frame.

The shin angle is described as the angle of the shank of the prosthesis with respect to the vertical, measured as negative if clockwise. The shin angle is depicted in Figure 2.2 below.

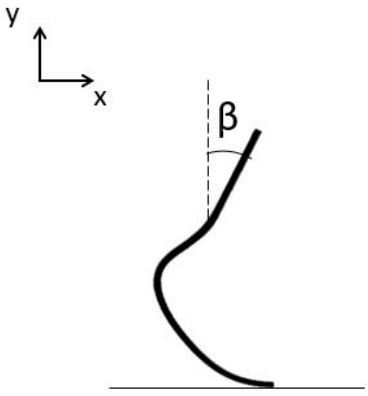

Figure 2.2: Definition of shin angle, β. The shin angle is the angle of the shank of the prosthesis with respect to the vertical. Positive shin angles are measured counterclockwise with respect to the vertical, and negative shin angles, clockwise. The xy plane of the global reference frame represents the sagittal plane, with running direction to the right.

The direction of the GRF is determined by the position of the CoM as well as the inertial acceleration of the athlete. As a simplification, since no data about the GRF direction could be found in literature, during this analysis it was assumed that the GRF is directed towards the CoM. Thus, the drive angle has to be considered too, which is the angle of the line connecting the contact point, Pc, with the CoM of the athlete with respect to the vertical. The drive angle is depicted in Figure 2.3. This drive angle, thus, determines the direction of the force applied on the RP.

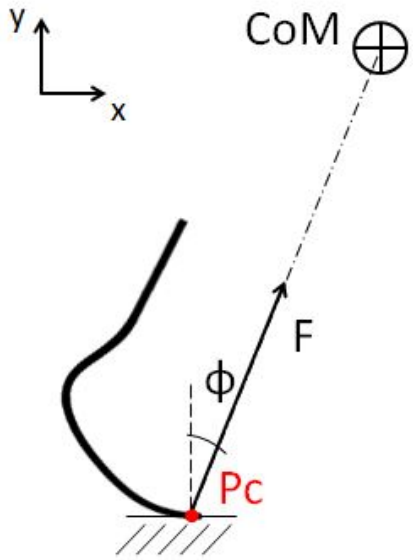

Figure 2.3: Definition of drive angle, ϕ. The drive angle is the angle in the sagittal plane between the vertical axis and the vector pointing from the contact point, Pc, to the center of mass, CoM. It is measured as negative if clockwise, with the running direction towards the right.

2.1.3. KINEMATICS OF START STEPS

The shin and drive angles vary for each step and for each athlete. Since no data on these kinematic parameters was available, the shin and drive angles for the block steps (rear and front block), step 1 (when the ground contact point is posterior to the position of the CoM) and step 2 and 3 (when the ground contact point is anterior to the position of the CoM) were retrieved from pictures and videos of the paralympic sprinter Oscar Pistorius and used as reference for the computations. The retrieval of the rear block parameters can be seen in Figure 2.4 below. The rest of the steps are shown in Appendix B.

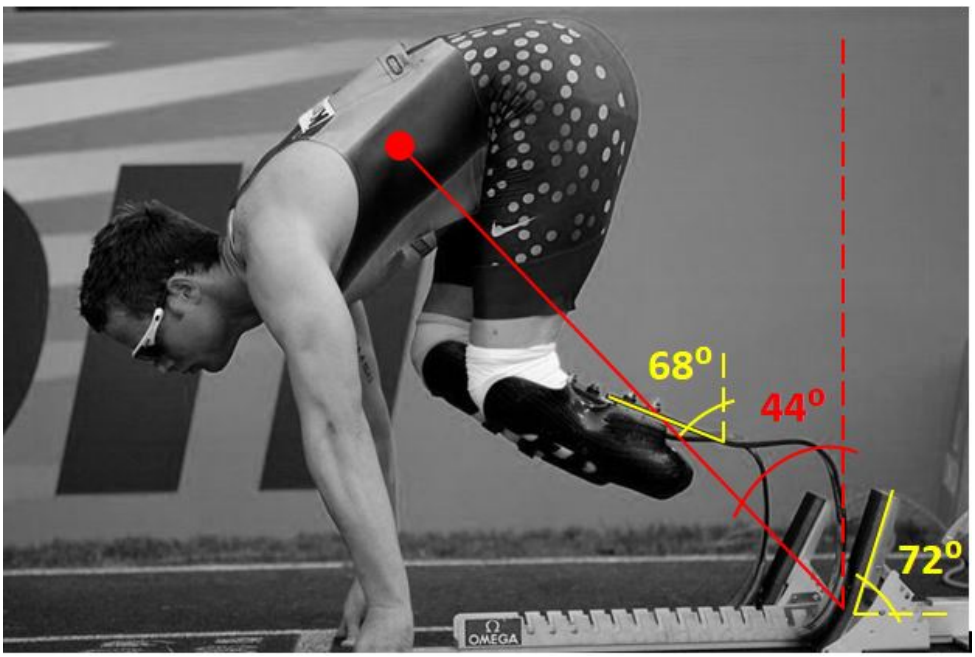

Figure 2.4: Retrieved shin, drive and block angles at rear block step.

This method is not accurate for the retrieval of the kinematic parameters. However, accurate kinematics were not required for an initial validation of the proposed design methodology. Thus, the retrieved values were considered to be valid for this purpose.

2.1.4. 2D STIFFNESS

As learned during the internship carried out at Ottobock, the vertical stiffness of RPs is calculated as $k_y = f_y/u_y$, with the vertical force, f_y, and displacement, u_y, represented in Figure 2.5 below.

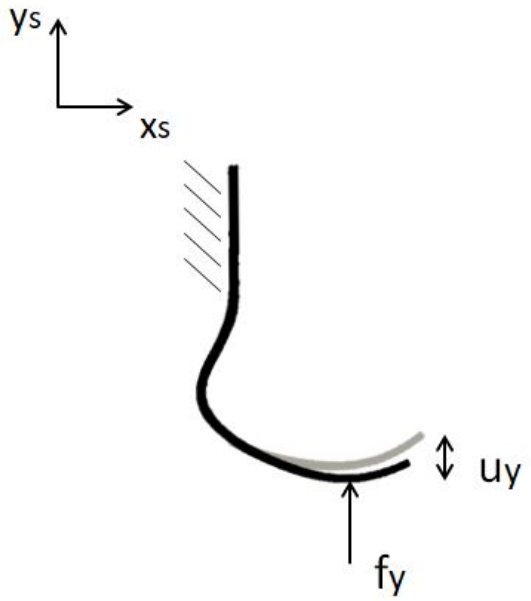

Figure 2.5: Definition of the vertical stiffness measured by prosthetic companies. The underformed prosthesis is shown in black. The deformed prosthesis after applying the vertical force, f_y, is shown in grey. The vertical displacement is represented as u_y. The stiffness is measured with respect to the local shin reference frame, $x_s y_s$, which is the same as the global reference frame xy since the shank of the prosthesis is vertically oriented.

It is observed that the kinematics of the athletes are not considered in this measurement. Moreover, only the component of the displacement in the direction of the force is considered, but a normal component of this displacement is also present. This behavior can be represented by the stiffness matrix measured with respect to the local shin reference frame. The stiffness matrix can be graphically represented as an ellipse, the so called stiffness ellipse, which gives an overview of the stiffness in all directions of the sagittal plane.

STIFFNESS MATRIX

Assuming a linear relation between the components u_{x_s} and u_{y_s} of the displacement vector $\mathbf{u_s}$, and the components f_{x_s} and f_{y_s} force vector $\mathbf{f_s}$, the components of the force vector can be expressed as:

$$f_{x_s} = k_{xx} u_{x_s} + k_{xy} u_{y_s} \tag{2.1}$$

$$f_{y_s} = k_{yx} u_{x_s} + k_{yy} u_{y_s} \tag{2.2}$$

These equations can be expressed in a vector/matrix notation as

$$\mathbf{f_s} = \mathbf{K u_s} \tag{2.3}$$

where:

$$\mathbf{f_s} = \begin{bmatrix} f_{x_s} \\ f_{y_s} \end{bmatrix} \tag{2.4}$$

$$\mathbf{K} = \begin{bmatrix} k_{xx} & k_{xy} \\ k_{yx} & k_{yy} \end{bmatrix} \tag{2.5}$$

$$\mathbf{u_s} = \begin{bmatrix} u_{x_s} \\ u_{y_s} \end{bmatrix} \tag{2.6}$$

where, due to the passive nature of RPs:

$$k_{xy} = k_{yx} \tag{2.7}$$

The 3 elements of the stiffness matrix can be computed by using standard linear least squares regression procedures with the data of the force, f_{x_s} and f_{y_s}, and displacement, u_{x_s} and u_{y_s}, from at least 2 tests.

STIFFNESS ELLIPSE

The stiffness matrix can be geometrically represented by multiplying a rotating input displacement of unit amplitude vector, $\mathbf{u_s}$, (see Equation 2.8) by the stiffness matrix, $\mathbf{K}$, and plotting the resulting force vectors, $\mathbf{f_s}$. The trajectory of these force vectors then describes an ellipse, which is known as the stiffness ellipse.

$$\mathbf{u_s} = \begin{bmatrix} cos(\alpha) \\ sin(\alpha) \end{bmatrix} \qquad 0 < \alpha < 2\pi \tag{2.8}$$

The eigenvectors and eigenvalues of the symmetric stiffness matrix are calculated to determine the shape, size, and orientation of the stiffness ellipse. An example of a stiffness ellipse can be seen in Figure 2.6. The shape is quantified as the ratio of the maximum eigenvalue to the minimum eigenvalue, i.e. the ratio of lengths of the axes of the ellipse. This ratio provides an indication of the anistropy of the stiffness: the greater this value, the more anisotropic the stiffness is. Only in the main axes of the ellipse the force and the displacement have the same direction. The orientation is represented by the angle ρ, which is the angle between the long axis of the ellipse, i.e. the direction of largest stiffness, and the +y axis. Similarly, the orientation of the minor axis would correspond with the direction of minimum stiffness. If a line is drawn through the origin in a certain direction, it will intersect the ellipse (red dot in Figure 2.6). The length of this line represents the stiffness of the RP in that direction, and this is called the directional stiffness.

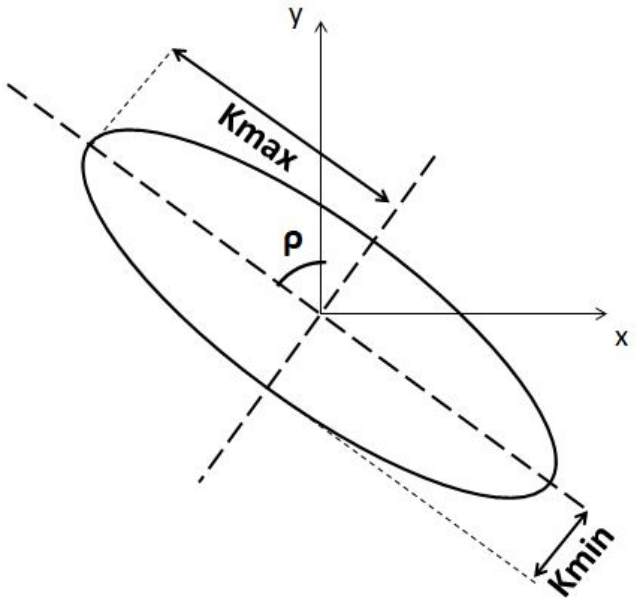

Figure 2.6: Definition of stiffness ellipse. The stiffness ellipse is defined by its orientation, which determined by ρ, the two axes of the ellipse, which determine the maximum and minimum stiffness ($K_{max} and K_{min}$, respectively), and .

Thus, knowing the stiffness ellipse of the different contact points of the prosthesis, it is possible to understand the behavior of these prostheses under the kinematics given at each step of a race.

2.2. DESIGN OF RPS - DEFLECTION DIRECTION METHODOLOGY

In this section the design methodology used by a prosthetic leader company is shown, which was learned during the internship carried out at this company. methodology was called the deflection Direction Methodology. This methodology consists of locally decreasing the thickness of the laminate by means of ply-dropping, in order to decrease local bending stiffness and tune the deflection behavior of the prostheses.

As already explained in the introduction, the amount of carbon fiber layers stacked determines the thickness of the prosthesis, and the thickness determines the bending stiffness of the prosthesis. The direction, amplitude and localization of the deformation of the prosthesis can thus be influenced by the local thickness. An illustration of ply-dropping is shown in Figure 2.7 below.

Figure 2.7: Illustration of a laminate ply drop on a flat laminate.

The idea behind this hypothesis is that by decreasing the thickness of a section, the local area moment of inertia (I), and thus the local bending stiffness (EI) are decreased, changing the deflection behavior of the prosthesis. Different locations of the ply-dropping area, or deformation area, lead to different deflection directions, as seen in Figure 2.8 below. Prosthetic companies locate this ply-dropping area as low as possible on the prosthesis ((c) in Figure 2.8) in order to obtain a GRF which is as vertical as possible with respect to the local shin reference frame.

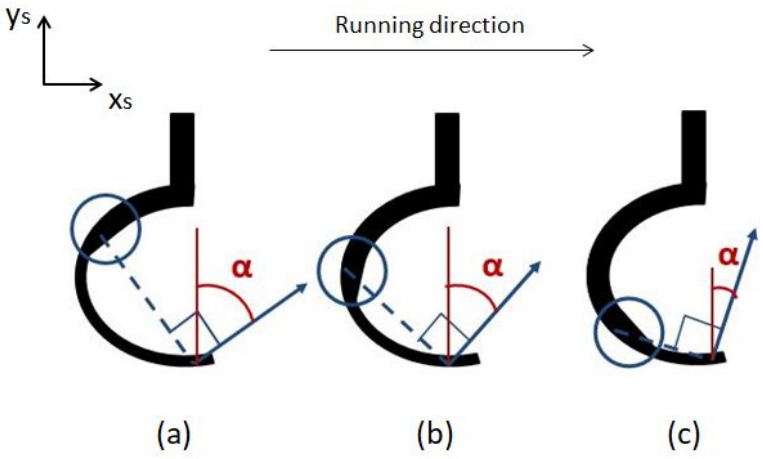

Figure 2.8: Deflection direction of the prosthesis contact point defined by the deformation area. The deformation areas are marked by circles, and the lower or the more distal from the shank this area is located, the more vertical the deflection direction is, i.e. the smaller the angle α is.

2.3. VARIABLE STIFFNESS RP - DEFORMATION POINT METHODOLOGY

The method proposed in this section, which is used to design a variable stiffness prosthesis, is based on the hypothesis that the stiffness of RPs changes for the different contact points and varies with force direction.

It was hypothesized that, if the distance between the deformation and contact point decreases, or if the angle of the applied force with respect to the vertical increases, the stiffness increases (see distances and angles in Figure 3.6). Considering this, a model was done to find the positions of the deformation point that, given the fixed shin and drive angle configurations of each step, will lead to a higher stiffness at step 1 than at step 3. Thus, the model proposed will only focus on step 1 and step 3. Steps 1 and 3 were previously explained in Section 2.1.3.

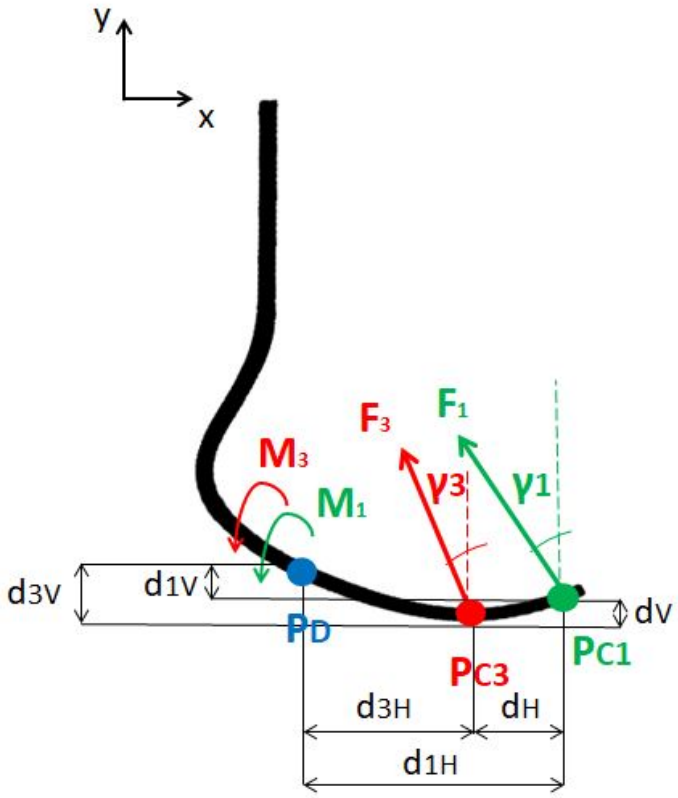

Figure 2.9: Illustration of the moments (M_1, M_3) created around the deformation point by the force at step 1 (F_1) and at the steady step (F_3). A is the contact point at step 1, B is the contact point at the steady step, and D is the deformation point of the RP. γ_1 and γ_3 define the direction of the forces with respect to the vertical. The vertical and horizontal distances between the deformation point and the contact points are represented (d_{3H}, d_{3V}, d_{3H}, d_{3V}), as well as the horizontal and vertical distance (d_H, d_V) between step 1 and step 3 contact points (P_{C1} and P_{C3}, respectively).

The objective of this model is to find the different positions of the deformation point (P_D in Figure 2.9) in the space where $M_1 < M_3$.

The moments created by the force in P_{C1} and the force in P_{C3} around P_D are expressed as:

$$M_1 = F_{1V} d_{1H} + F_{1H} d_{1V} \tag{2.9}$$

$$M_3 = F_{3V} d_{3H} + F_{3H} d_{3V} \tag{2.10}$$

Where F_{1H} and F_{3H} are negative. Equation 2.9 can be rewritten as:

$$M_1 = F_{1V}(d_{3H} + d_H) + F_{1H}(d_{3V} - d_V) \tag{2.11}$$

Considering that the constraint of this model is $M_1 < M_3$:

$$F_{1V}(d_{3H} + d_H) + F_{1H}(d_{3V} - d_V) < F_{3V} d_{3H} + F_{3H} d_{3V} \tag{2.12}$$

What leads to:

$$d_{3V} > \frac{F_{1V}d_H - F_{1H}d_V - (F_{3V} - F_{1V})d_{3H}}{F_{3H} - F_{1H}} \tag{2.13}$$

Defining:

$$q = \frac{F_{1V}d_H - F_{1H}d_V}{F_{3H} - F_{1H}} \tag{2.14}$$

$$m = \frac{F_{1V} - F_{3V}}{F_{3H} - F_{1H}} \tag{2.15}$$

We reach the following inequality:

$$d_{3V} > md_{3H} + q \tag{2.16}$$

A model based on this inequality was developed in Matlab (the code can be found in Appendix C). Since a linear force-displacement relation was assumed, it was considered in this model that the stiffness was not dependent on the force magnitude. For this reason, the force magnitude is not accounted as a variable in this analysis, and it is assumed that both contact points are subjected to an identical force magnitude. Thus, replacing the forces results in the following expressions for m and q.

$$m = \frac{Fcos\gamma_1 - Fcos\gamma_3}{Fsin\gamma_3 - Fsin\gamma_1} \tag{2.17}$$

$$q = \frac{Fcos\gamma_1 d_H - Fsin\gamma_1 d_V}{Fsin\gamma_3 - Fsin\gamma_1} \tag{2.18}$$

Which equals:

$$m = \frac{cos\gamma_1 - cos\gamma_3}{sin\gamma_3 - sin\gamma_1} \tag{2.19}$$

$$q = \frac{cos\gamma_1 d_H - sin\gamma_1 d_V}{sin\gamma_3 - sin\gamma_1} \tag{2.20}$$

Since the inputs of this model (shin and drive angles) are uncertain, there is also an inherent uncertainty associated with the output of the model. Thus, some deviations of γ ($\delta\gamma$) were derived for steps 1 and 3 (Appendix D explains in detail the process of the derivation of these angles).

If rewritten with the deviations, the inequality in Equation 2.20 can be expressed as:

$$d_{3V} > \frac{cos(\gamma_1 \pm \delta\gamma_1) - cos(\gamma_3 \pm \delta\gamma_3)}{sin(\gamma_1 \pm \delta\gamma_1) - sin(\gamma_3 \pm \delta\gamma_3)} d_{3H} + \frac{cos(\gamma_1 \pm \delta\gamma_1)d_H + sin(\gamma_1 \pm \delta\gamma_1)d_V}{sin(\gamma_1 \pm \delta\gamma_1) - sin(\gamma_3 \pm \delta\gamma_3)} \tag{2.21}$$

2.4. FEM MODELLING OF RPS

A CAD model of different RP designs was created in Abaqus in order to compute the 2D stiffness explained in Section 2.1.4, and several assumptions were done for the simulations. First, a linear relation between force and displacement of the contact point was assumed, that is, a constant stiffness. Second, rollover and blade deflection were not considered, and thus a single contact point was assumed in which the force was applied. Finally, a non-following load was applied on the contact point, keeping a constant orientation with respect to the global reference frame, as seen in Figure 2.10 below.

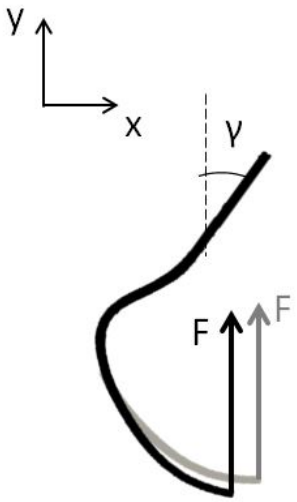

Figure 2.10: Non-following load simulated in the Abaqus models of the different RPs designs. After RP deflection (in grey), the force direction is kept unchanged. The orientation of the prosthesis is defined as $\gamma = \beta - \phi$, where β is the shin angle, and phi is the drive angle.

The carbon fiber/epoxy properties used in the simulations can be seen in Table 2.1 below.

E1 [MPa]	E2 [MPa]	E3 [MPa]	G12 [MPa]	G13 [MPa]	G23 [MPa]	U12	U13	U23
138000	9500	9500	5200	5200	1450	0.28	0.28	0.4

Table 2.1: Carbon fiber/epoxy properties used in the FEM simulations: tensile modulus (E), shear modulus (G) and Poisson's ratio. CITE!

For the simulations, the upper shank was encastred ($\Delta x = \Delta y = \Delta z = 0$), mimicking the attachment to the stump. The force was applied on the corresponding contact point for each of the steps analysed. The magnitude of the forces at block, start and steady are shown below, in Table 2.2, [9].

Block steps	**Start steps**	**Steady steps**
1.5xBW	3xBW	3.5xBW

Table 2.2: GRFs measured at the block steps, start steps and steady steps [7].

No displacement restrictions were set on the toe, in order to analyse the 2D displacement. Thus, the displacement in both, the vertical and horizontal direction, was measured under the applied force. An overview of the boundary conditions can be seen in Figure 2.11(a). Different load orientations were tested to calculate the stiffness matrix at each contact point.

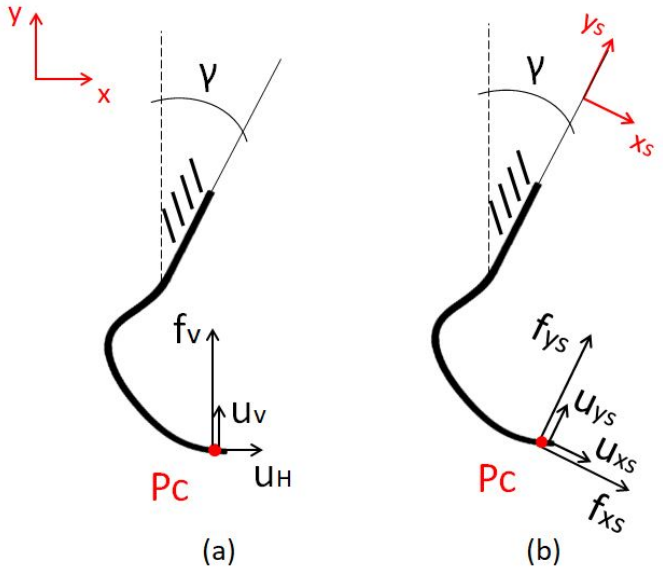

Figure 2.11: Boundary conditions, inputs and outputs of the FEM model. (a) The shank was encastred, a force (f_V) was applied, and the displacements (u_H and u_V) of the contact point (Pc) were extracted from the simulations, all of them measured with respect to the global reference frame. (b) The force and displacement expressed in the local shin reference frame (f_{x_s}, f_{y_s}, u_{x_s}, u_{y_s}) are used to compute the stiffness matrix and ellipse of the prostheses at Pc.

The force f_V and the displacements u_H and u_V are measured with respect to the global reference frame (xy reference frame seen in Figure 2.11). In order to express them in the local reference frame ($x_s y_s$ reference frame seen in Figure 2.11), the rotation matrix seen below is needed.

$$R_c = \begin{bmatrix} cos(\gamma) & -sin(\gamma) \\ sin(\gamma) & cos(\gamma) \end{bmatrix} \tag{2.22}$$

Then, the resulting f_{x_s}, f_{y_s}, u_{x_s}, and u_{y_s} of at least 2 simulations with different γ, are used to calculate the stiffness matrices and ellipses of each of the contact points of the prostheses, as previously explained in Section 2.1.4.

2.5. LAB TESTING OF RPS

In order to retrieve the 2D stiffness of RPs, these prostheses need to be tested on a static compression test bench. For this, considering that such test has not been carried out before, a new testing methodology is proposed.

The ideal test method for characterizing a prosthesis would be to clamp it at the contact point, as seen in Figure 2.12 below. In this way, it is ensured that the point of force application (P_A) and contact point (P_C) are aligned.

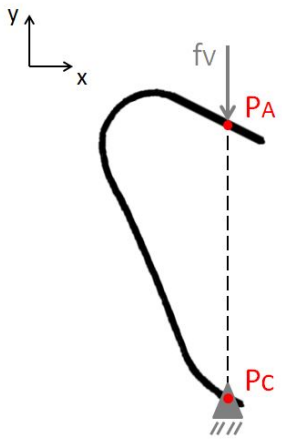

Figure 2.12: Clamped new prosthesis design. It ensures that the point of force application, P_A, and the contact point, P_C, are always aligned, since the horizontal displacement of the contact point is constraint.

Constraining the displacement of the contact point leads to a horizontal and a vertical reaction force. The vertical reaction force is measured by the test bench, but in this case the horizontal force could not be measured. Therefore, a set up with a slider is suggested instead. A representation of the set up is shown in Figure 2.13, and the real set up can be seen in Figure 2.14.

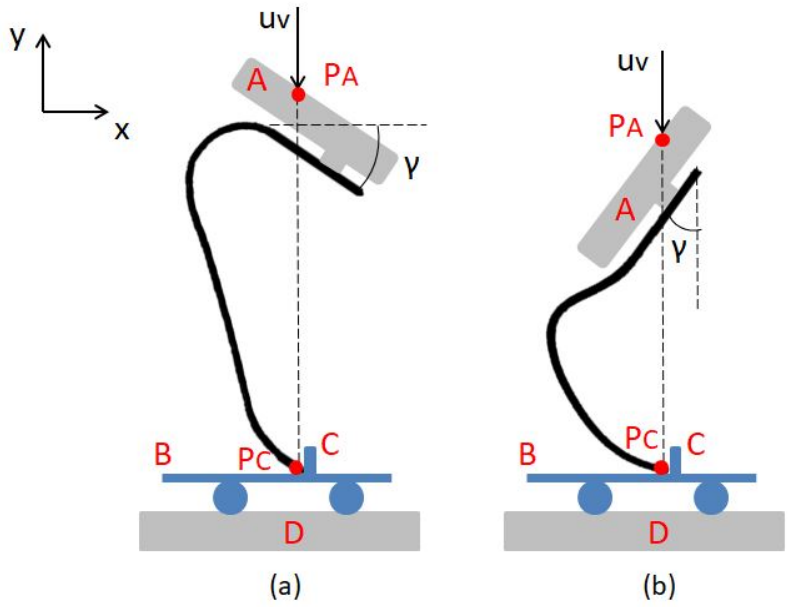

Figure 2.13: Representation of the static compression test set-up (a) for the new design and (b) for the 1E90. A is the attachment to the prosthesis that allows the rotation of the prosthesis ensuring that the point of attachment to the test bench (P_A) and the contact point (P_C) are vertically aligned. B is the slider that allows the horizontal displacement ensuring that the contact point does not change during the test. C is the vertical aluminum profile that ensures that there is no relative movement between the prosthesis and the slider. And D is the aluminum profile over which the slider translates.

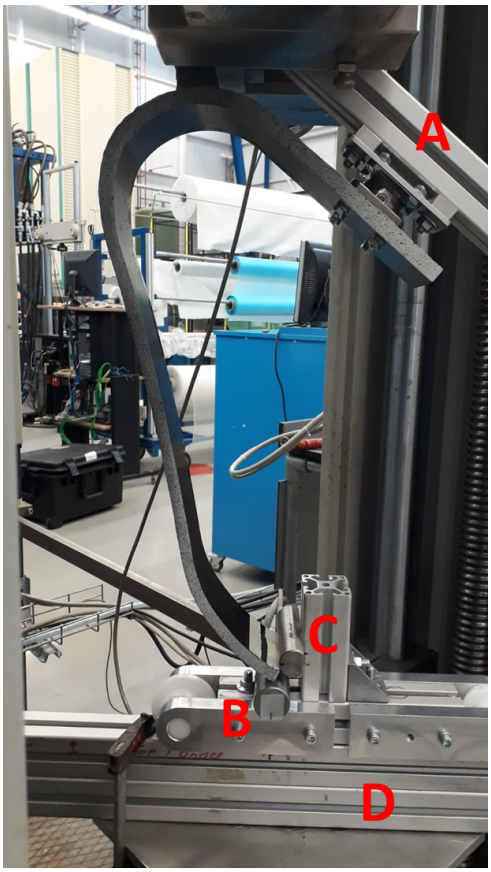

Figure 2.14: Static compression test set-up. A is the attachment to the prosthesis that allows the rotation of the prosthesis ensuring that the point of attachment to the test bench and the contact point are vertically aligned. B is the slider that allows the horizontal displacement ensuring that the contact point does not change during the test. C is the vertical aluminum profile that ensures that there is no relative movement between the prosthesis and the slider. And D is the aluminum profile over which the slider translates.

The displacement applied by the test bench and the measured returned force are aligned with the vertical axis of the global reference frame. An attachment between the prosthesis and the test bench was made (A in Figure 2.14), which enabled positioning the prosthesis in different angles with respect to the vertical. This attachment also ensured that the connection to the bench (P_A in Figure 2.13) was vertically aligned with the contact point (P_C in Figure 2.13). A cylinder on top of the slider was used in order to ensure that the right contact point was used. The slider (B) allowed the horizontal displacement of the contact point. The vertical aluminum profile (C) ensures that the prosthesis and the slider translate together along the horizontal aluminum profile (D).

The stiffness measured by the test bench is $k_{testbench} = f_y/u_y$, which was measured with respect to the global reference frame. In order to measure the 2D stiffness, both the horizontal and vertical force and displacement need to be considered. In order to obtain the horizontal displacement, a Digital Image Correlation (DIC) analysis method was used, which allowed to track the 3D displacement of the speckles drawn in the profile of the prostheses. Figure 2.15 shows a top view of the set-up of the tests using the DIC.

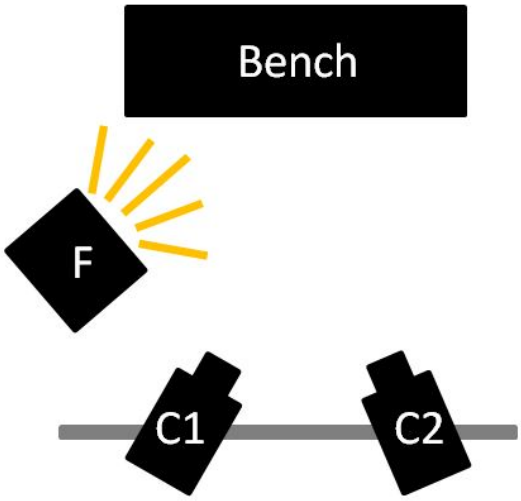

Figure 2.15: DIC set-up. 2 cameras (C1 and C2), together with a flash unit (F), are located in front of the test bench (Bench) with the prostheses.

If an ideal slider was assumed, the horizontal displacement, u_H, of the contact point would not be constrained, and the horizontal force could be assumed to be zero ($f_H = 0$). However, the presence of friction initially constraints u_H.

Figure 2.16 represents the test set up for $u_H > 0$. If $u_H > 0$, the point of force application, P_A, and the contact point, P_C, are not aligned anymore. This leads to the presence of a couple ($M = f_y u_H$) which influences the deflection of the prosthesis.

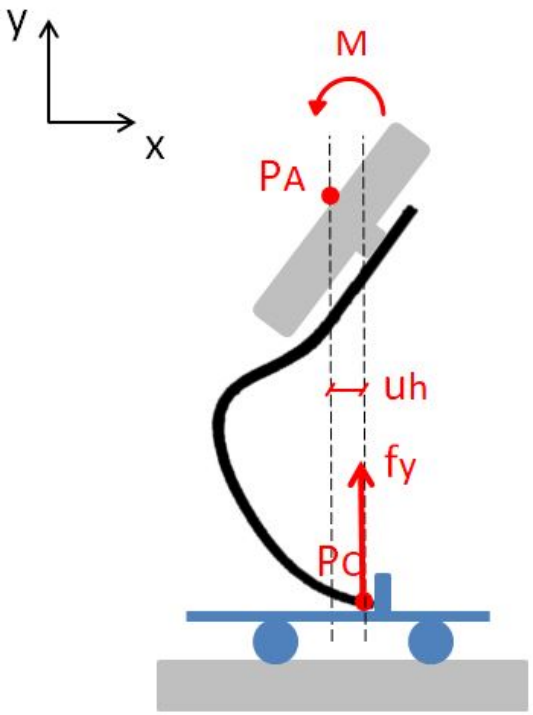

Figure 2.16: Moment ($M = f_y u_H$) present on test if the point of force application, P_A, and the contact point, P_C, are not aligned. This misalignment is a result of the horizontal displacement ($u_H > 0$) of the contact point.

In order to avoid this moment, it was decided to analyze the data where $u_H = 0$ only, i.e. where the point of force application, P_A, and the contact point, P_C, are still aligned. It must be considered that this test configuration differs from that in the FEM simulations.

The presence of friction leads to a constraint of u_H and, thus, to a reaction force in the horizontal direction, f_H, which needs to be calculated. It is observed that the presence of this horizontal force also creates a moment around P_A, which was neglected despite the large lever arm, assuming that the horizontal force, f_H, is small compared to the vertical force.

Following the law of the Coulomb friction:

$$f_H \leq \mu f_N \tag{2.23}$$

where, as seen in Figure 2.17:

$$f_N = f_v + w_s \tag{2.24}$$

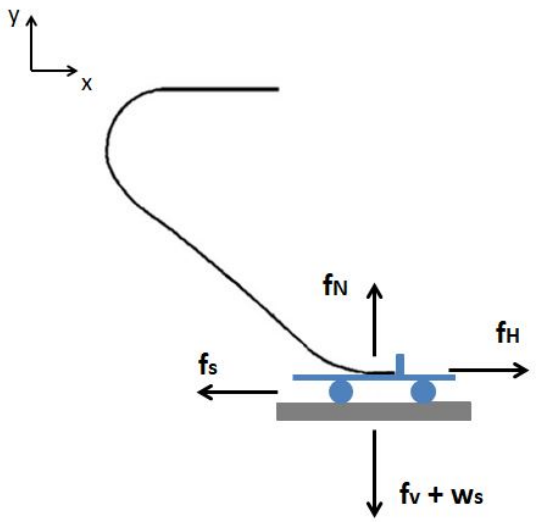

Figure 2.17: Contact between slider (blue) and aluminum profile (grey). f_s is the friction force between slider and aluminum profile; f_H and f_V are the horizontal and vertical reaction forces, respectively; w_s is the weight of the slider; and f_N is the normal force. xy is the global reference frame.

μ is the static friction coefficient of the system, and can be experimentally measured by following the procedure observed in Figure 2.18 below.

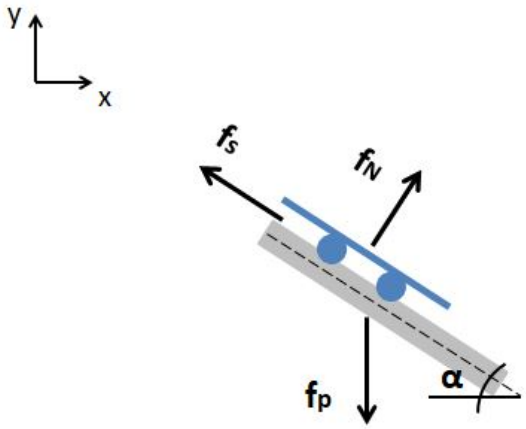

Figure 2.18: Experimental method to calculate the static friction coefficient. The aluminum profile, with the slider on it, is tilted until the slider starts translating. An angle meter attached to the aluminum profile measured the angle. Videos of this procedure are recorded and analysed in order to retrieve the angle, α, at which the slider starts translating. xy is the global reference frame.

From Figure 2.18 it can be seen that:

$$f_s = f_p sin(\alpha) \tag{2.25}$$

$$f_N = f_p cos(\alpha) \tag{2.26}$$

Knowing that:

$$f_s = \mu f_N \tag{2.27}$$

The following expression for μ can be obtained:

$$f_p sin(\alpha) = \mu f_p cos(\alpha) \tag{2.28}$$

$$\mu = tan(\alpha) \tag{2.29}$$

With this, the expression for the horizontal force returned by the prostheses can be obtained, when the horizontal displacement of the contact point is zero. Thus,

$$f_H \leq \mu(f_V + w_s) \tag{2.30}$$

when:

$$u_H = 0 \tag{2.31}$$

The horizontal force is known only at points $t = 0$ and $t = ts$ (ts is the time when the slide starts translating).

If t=0:

$$f_H = 0 \tag{2.32}$$

And if t=ts:

$$f_H = \mu(f_V + w_s) = f_{Hmax} \tag{2.33}$$

It is known that f_H increases in the interval $0 < t < ts$, but the exact evolution of f_H in time is not known. Therefore, 2 different assumptions were made and compared to each other: in the first one, the force was assumed to be constant and equal to zero while $u_H = 0$; in the second one, the force was assumed to be constant and equal to f_{Hmax} while $u_H = 0$.

The forces f_V and f_H, and the displacement u_V are measured with respect to the global reference frame (xy reference frame seen in Figure 2.11). In order to express them in the local reference frame ($x_s y_s$ reference frame seen in Figure 2.11), the rotation matrix seen below is needed.

$$R_c = \begin{bmatrix} cos(\gamma) & -sin(\gamma) \\ sin(\gamma) & cos(\gamma) \end{bmatrix} \tag{2.34}$$

Then, the resulting f_{x_s}, f_{y_s}, u_{x_s}, and u_{y_s} of at least 2 simulations with different γ, are used to calculate the stiffness matrices and ellipses of each of the contact points of the prostheses, as previously explained in Section 2.1.4.

3

ANALYSIS OF CURRENT RPS

In this chapter, in order to better understand the behavior of current RPs during the first steps, a running prosthesis imitating current RPs was created and simulated in Abaqus. The stiffness matrices and ellipses of the different contact points were retrieved, and are shown in this chapter.

The shape of the prosthesis modelled is copied from the Cheetah RP, while the lamination modelled tries to imitate that of the 1E90, and was created following the lamination rules in Appendix E. Marlou van Rhijn, member of the Dutch Paralympic team, runs with a category 3 prosthesis at the beginning of each season. As already shown in Table 1.1, the bending stiffness measured under the static compression test conditions should be around 16.5N/mm for a category 3 spring. Thus, a lamination providing such a bending stiffness had to be found. The explanation of how the model was created in Abaqus in explained in Appendix F. The drawing of the model with all the dimensions can be found at Appendix G. This model was created following Ottobock's Deflection Direction Method, explained in Section 2.2. Thus, this model was called 1E90 since, despite of having a different shape, it is trying to mimic the behavior of the 1E90. Figure 3.1 shows the Abaqus model of the 1E90 RP.

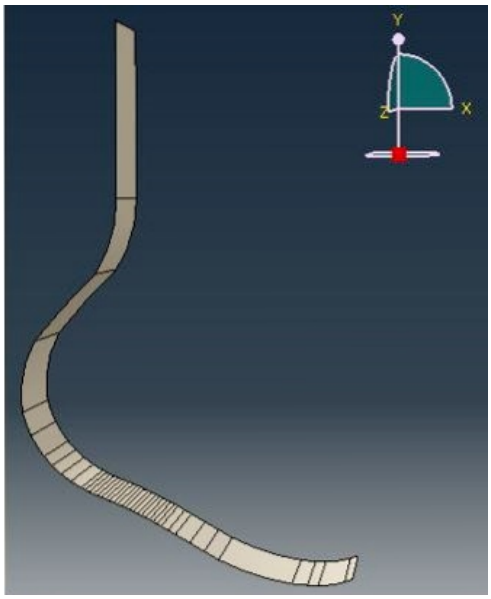

Figure 3.1: Abaqus model of Ottobock's 1E90. Further explanations about the model can be found in Appendix F.

The stiffness matrices and ellipses of the 3 different contact points seen in Figure 3.2 were calculated, following the procedure explained in Section 2.1.4. For this, different force directions (γ in Figure 3.2) were simulated for each contact point, and the resulting vertical and horizontal displacements of the different contact points were calculated. The three contact points analyzed are shown in Figure 3.2.

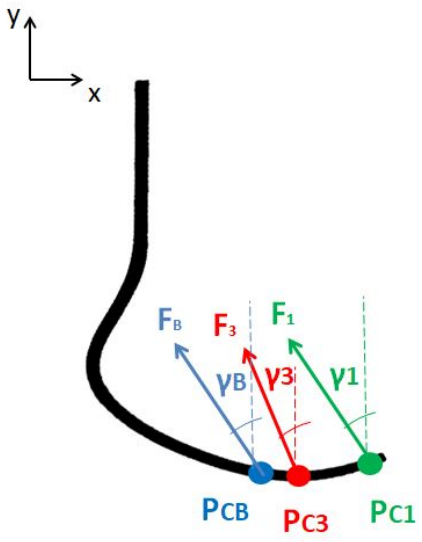

Figure 3.2: Step 1 (P_{C1}), step 3 (P_{C3}), and block (P_{CB}) contact points in 1E90. Bear in mind that both, rear and front block steps, have the same contact point, as learned from the kinematics shown in Figure 3.3. The γ angles represent the different force directions applied on each contact point.

With the data obtained from the simulations, the following stiffness matrices for the 3 different contact points of the 1E90 model were computed:

$$K_{1E90-step1} = \begin{bmatrix} 92.67 & -47.42 \\ -47.42 & 36.87 \end{bmatrix} \tag{3.1}$$

$$K_{1E90-step3} = \begin{bmatrix} 102.03 & -63.72 \\ -63.72 & 56.82 \end{bmatrix} \tag{3.2}$$

$$K_{1E90-block} = \begin{bmatrix} 105.27 & -71.4 \\ -71.4 & 68.38 \end{bmatrix} \tag{3.3}$$

With these matrices, the stiffness ellipses of each contact point were obtained, and are shown in Figure 3.4. The kinematics of the athletes were also considered, which are shown in Figure 3.3 below. In this Figure it can be observed that the CoM is posterior to the ground contact point at the second step after the block steps.

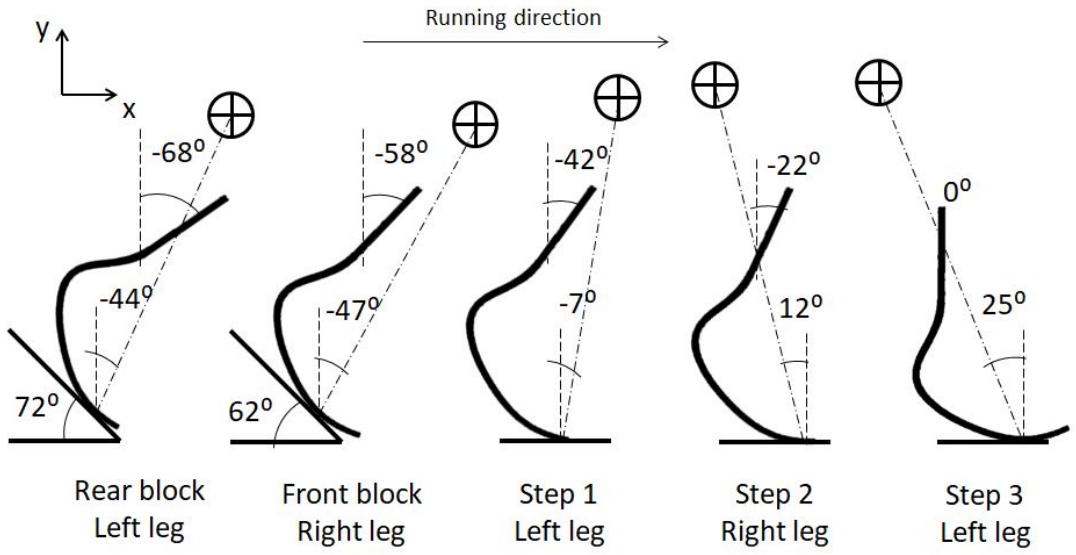

Figure 3.3: Representation of shin and drive angles on the first 5 actions of a sprint: rear block, front block, step 1, step 2 and step 3. Data measured from photos and videos of the BTA paralympic athlete Oscar Pistorius. The xy plane of the global reference frame represents the sagittal plane.

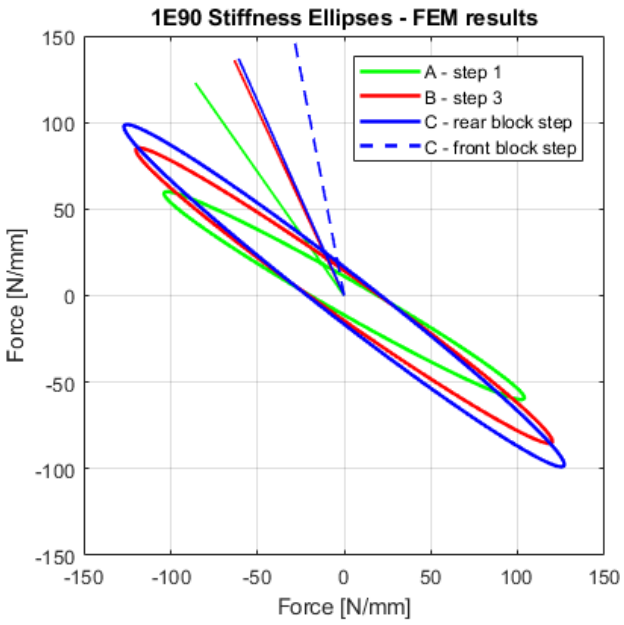

Figure 3.4: FEM results of the stiffness ellipses of the prosthesis 1E90 for the 3 different contact points. A (in green) is the contact point of step 1, B (in red) is the contact point of step 3, and C (in blue) is the contact point of both, rear and front block steps. The lines represent the direction of the force at each of the steps, based on the results in Figure 3.3. The green line represents the force direction at step 1; the red, at step 3; the solid blue, at the rear block step; and the dotted blue line, at the front block step.

The radius of each ellipse at the interception with its corresponding line defines the stiffness of each of the steps. A close-up from the intersections in Figure 3.4 can be seen in Figure 3.5

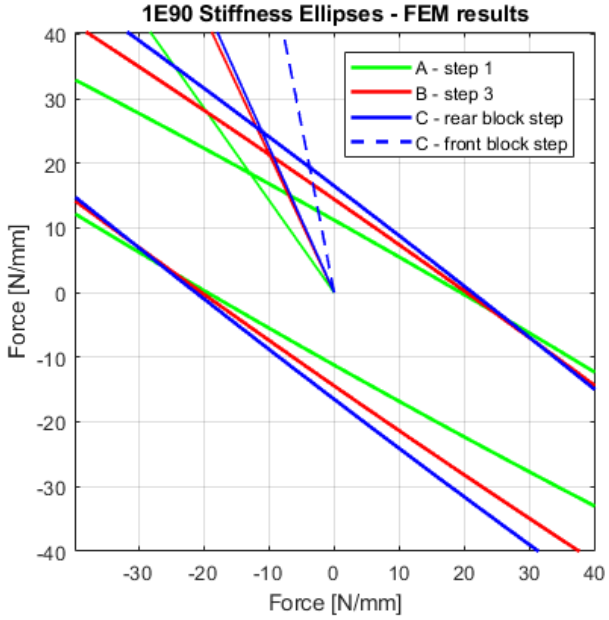

Figure 3.5: Close up of the FEM results of the stiffness ellipses of the prosthesis 1E90 for the 3 different contact points.

The values of these radius, together with the orientation and maximum and minimum stiffness values of each ellipse can be seen in Table 3.1.

	Directional Stiffness [N/mm]	ρ [deg]	K max [N/mm]	K min [N/mm]
Step 1	22.54	60.23	119.79	9.75
Step 3	23.56	54.76	147.04	11.81
Rear block step	27.33	52.24	160.56	13.08
Front block step	19.76	52.24	160.56	13.08

Table 3.1: Directional stiffness, orientation (rho, measured anticlockwise with respect to the y axis), maximum stiffness and minimum stiffness of the 1E90 stiffness ellipses at the 3 different contact points. These results were obtained from the FEM simulations.

From Table 3.1 it can be observed that the directional stiffness (which is explained in Section 2.1.4) of the step 1 contact point at the kinematics given at this step is slightly smaller than that of the step 3. As for the block contact point, it can be seen that the rear block step is the stiffest among all steps, while the front block step is the most compliant. It is known that the force application in the rear block is one of the most relevant aspects for a good sprint start. Thus, being the rear block step the stiffest of all the analysed steps is favourable. However, the stiffness of the other steps should be improved.

It is observed that the orientation seems to be influenced by the location of the deformation area, since a bigger angle is observed as the contact point is moved further from the deformation area. It is also noticed that the proximity of the contact points to the deformation area affects the maximum stiffness, as it increases as the contact point is closer to the deformation area.

If the deflection area is simplified and reduced to a deformation point, the moments created by the forces at each step around the deformation point can be calculated. The moments on the 1E90 are illustrated in Figure 3.6, which only focuses on the steps 1 and 3. P_{C1} is the contact point for the step 1, and P_{C3}, for the step 3. Two factors influence the directional stiffness: the distance from the contact point (P_{C1} or P_{C3}) to the deformation point (P_D), and the direction of the force. The further the contact point is located from the deformation point, the bigger the moment created around the deformation point will be, decreasing the stiffness. As for the force direction, the smaller the angle depicted (γ), the larger the moments around the deformation point and the smaller the stiffness will be too.

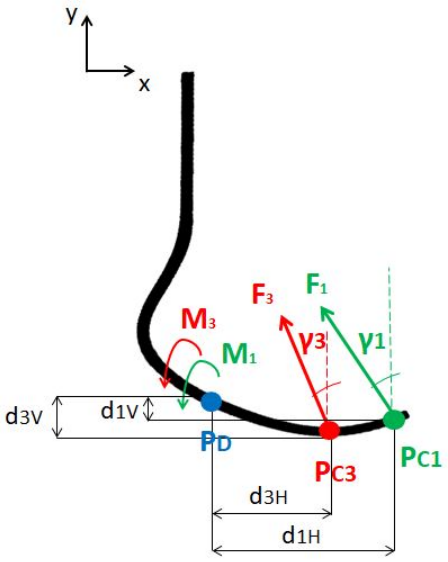

Figure 3.6: Illustration of the moments (M_1, M_3) created around the deformation point by the force at step 1 (F_1) and at steady step (F_3). P_{C1} is the contact point at step 1, P_{C3} is the contact point at a steady step, and P_D is the deformation point of the RP. γ_1 and γ_3 define the direction of the forces with respect to the vertical. The vertical and horizontal distances between the deformation point and the contact points (d_{3H}, d_{3V}, d_{3H}, d_{3V}) are also represented.

The results of the moments M_1 and M_3 can be seen in Table 3.2. The calculation of these moments is shown in Appendix H.

M_1 [Nmm]	M_3 [Nmm]
131.48	120.7

Table 3.2: Moments created at steps 1 and 3 around deformation point of the 1E90.

It can be observed that the moment created by the force in step 1 around the deformation point is bigger than the moment created by the force in step 3. This larger moment leads to a larger deflection, decreasing the stiffness at step 1.

Based on these results, it was hypothesized that a design methodology based on the position of the deformation point could be developed in order to create a variable stiffness prostheses. This variable stiffness prosthesis could be defined by locating the deformation and contact points in such a way that, given the configuration of shin and drive angles shown in Figure 3.3, the moment created by the force in the contact point of step 1 is smaller than the moment created by the force in the contact point of a step 3. As a result, this new design would provide a higher stiffness at step 1 than at step 3.

4

DEFORMATION POINT METHODOLOGY

In this chapter the method proposed in Section 2.3 to design a variable stiffness prosthesis is developed, and a new RP design is proposed, which would provide a higher directional stiffness at step 1 compared to step 3.

The method proposed is based on the hypothesis that the directional stiffness of RPs changes for the different contact point and varies with force direction, as learnt from the model of the 1E90 presented in Chapter 3.

From this model it was discovered that the stiffness is dependent on the position of the contact point and the angle of the force applied on the prosthesis. If the distance between the deformation and contact point decreases, or if the angle of the applied force with respect to the vertical increases, the stiffness increases (see distances and angles in Figure 3.6). Considering this, a model was made to find the positions of the deformation point that, given the fixed shin and drive angle configurations previously mentioned and shown in Figure 3.3, will lead to a higher directional stiffness at step 1 than at step 3. Thus, the following model will only focus on step 1 and step 3.

The kinematic variables of the model are shown in Table 4.1.

ϕ_1 [deg]	ϕ_3 [deg]	β_1 [deg]	β_3 [deg]	γ_1 [deg]	γ_3 [deg]	d_H [mm]	d_V [mm]
7	-25	42	0	-35	-25	36.71	7.04

Table 4.1: Variables of the deformation point model. ϕ is the drive angle, β is the shin angle, $\gamma = \phi - \beta$, is the direction of the force with respect to the vertical, and d_H and d_V are the horizontal and vertical distances between the start and steady contact points.

For the variables shown in Table 4.1, the modelled inequality in Equation 2.3 in Section 2.3 leads to the results shown in Figure 4.1.

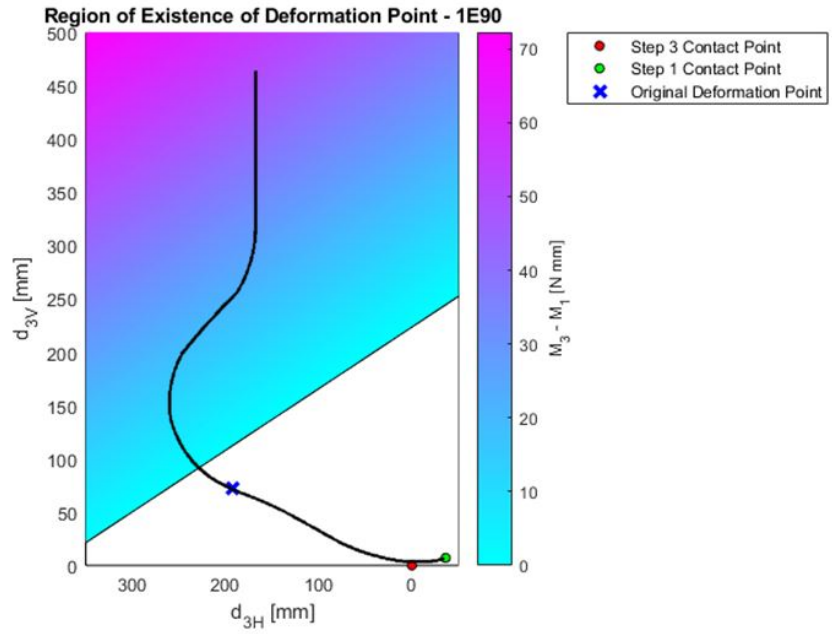

Figure 4.1: The coloured region is the area of existence of the deformation point, P_D, that leads to $M_1 < M_3$. The reference line, where $M_1 = M_3$, separates the acceptable (coloured) from the non-acceptable (white) area. P_{C3} (in red) is the step 3 contact point. P_{C3} (in green) is the step 1 contact point. d_{3H} is the horizontal distance between point P_D and P_{C3}. d_{3V} is the vertical distance between point P_D and P_{C3}. The distances between P_{C1} and P_{C3} are $d_H = 36.24mm$ and $d_V = 7.04mm$. The side view of the original prosthesis model is also inserted. It is noticeable from the colour gradient in the acceptable area that the further top-left the deformation point is located from the contact points, the bigger the difference between the moments is.

Since the inputs of this model (shin and drive angles) are uncertain, there is also an inherent uncertainty associated with the output of the model. The following deviations were derived for the step 1 and step 3 drive and shin angles (Appendix D explains in detail the process of the derivation of these angles):

$$\delta\phi_1 = \pm 1.7^\circ \tag{4.1}$$

$$\delta\phi_3 = \pm 1.86^\circ \tag{4.2}$$

$$\delta\beta_1 = \pm 2.13^\circ \tag{4.3}$$

$$\delta\beta_3 = \pm 2.31^\circ \tag{4.4}$$

These ϕ and β deviations led to the following force direction (γ) deviations:

$$\delta\gamma_1 = \pm 2.72^\circ \tag{4.5}$$

$$\delta\gamma_3 = pm2.97^\circ \tag{4.6}$$

If the inequality 2.3 in Section 2.3 is rewritten with the deviations, this inequality can be expressed as:

$$d_{3V} > \frac{cos(\gamma_1 \pm \delta\gamma_1) - cos(\gamma_3 \pm \delta\gamma_3)}{sin(\gamma_1 \pm \delta\gamma_1) - sin(\gamma_3 \pm \delta\gamma_3)} d_{3H} + \frac{cos(\gamma_1 \pm \delta\gamma_1) d_H + sin(\gamma_1 \pm \delta\gamma_1) d_V}{sin(\gamma_1 \pm \delta\gamma_1) - sin(\gamma_3 \pm \delta\gamma_3)} \tag{4.7}$$

4 different combinations can be simulated from this inequality, as seen in Table 4.2.

Table 4.2: Combinations of force direction deviations.

Case	$\delta\gamma_1$	$\delta\gamma_3$
1	+	-
2	-	+
3	+	+
4	-	-

The results of the inequality in each of the 4 cases are shown in Figure 4.2.

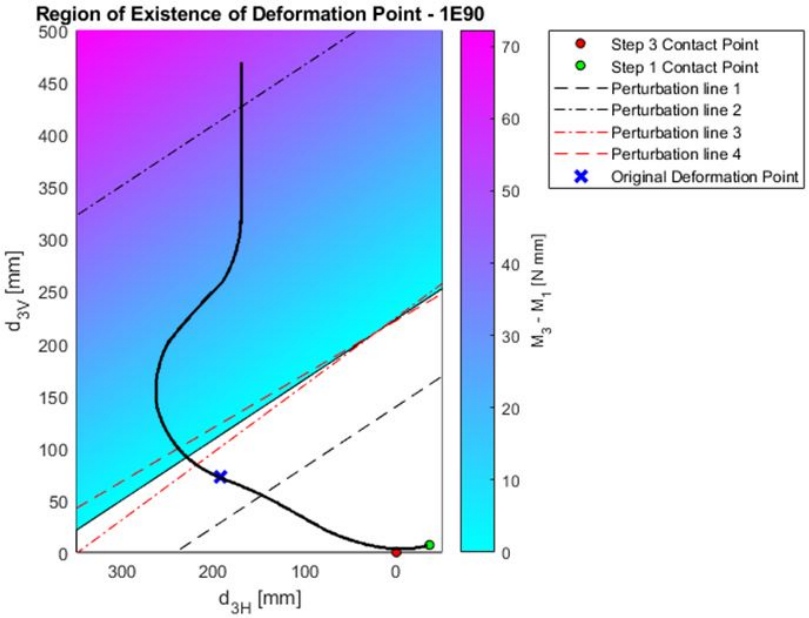

Figure 4.2: Results of applying perturbations on the force direction of the model. Each perturbation line represents each of the cases shown in Table 4.2. The coloured region is the area of existence of the deformation point, P_D, that leads to $M_1 < M_3$. The reference line, where $M_1 = M_3$, separates the acceptable (coloured) from the non-acceptable (white) area. P_{C3} (in red) is the step 3 contact point. P_{C1} (in green) is the step 1 contact point. d_{3H} is the horizontal distance between P_D and P_{C3}. d_{3V} is the vertical distance between point P_D and P_{C3}. The distances between P_{C1} and P_{C3} are $d_H = 36.24mm$ and $d_V = 7.04mm$. The side view of the original prosthesis model is also inserted.

It is observed that the most restrictive perturbation line, which corresponds to case 2 in the Table 4.2, is very far from the reference line compared to the rest of the perturbation lines. The distance to the reference line varies for each perturbation line due to the non linearity of the function modeled (see again Equation 4.7). In the function, with the construction of $y = mx + q$, q is the constant setting the distance of the perturbed lines from the reference line. And the expression for q in the second perturbation case is:

$$q = \frac{cos(\gamma_1 - \delta\gamma_1)d_H + sin(\gamma_1 - \delta\gamma_1)d_V}{sin(\gamma_1 - \delta\gamma_1) - sin(\gamma_3 + \delta\gamma_3)} \tag{4.8}$$

If attention is paid to the denominator, it is observed that adding the deviations of the case 2 (-$\delta\gamma_1$ and +$\delta\gamma_3$), the denominator gets closer to 0, what makes q increase.

Since this perturbation line is the most restrictive one, only this perturbation case was considered in the design process.

4.1. NEW SHAPE

Figure 4.3 now also shows the approximate height at which the stump is located from the ground [21], which should be preserved in order to comply with the rules of the Paralympic committee.

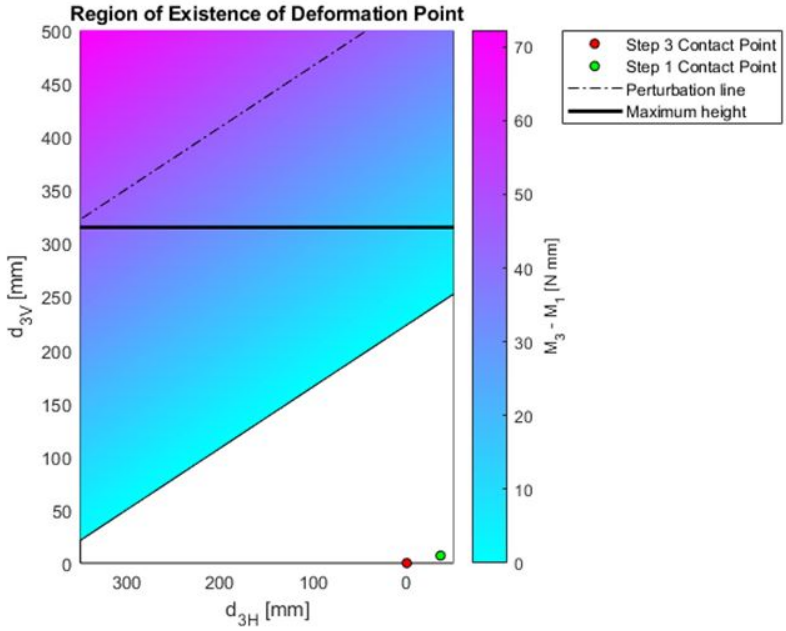

Figure 4.3: Coloured is the region of existence of the acceptable deformation point. The horizontal line at $d_{3V} = 315mm$ sets the approximate height of the stump. The distances between P_{C1} and P_{C3} are $d_H = 36.24mm$ and $d_V = 7.04mm$.

It can be observed that, with this distance between P_{C1} and P_{C3}, no deformation point can be fit in the ideal region due to the height constraint. Thus, in order to lower the perturbation line, the distance between the contact points P_{C1} and P_{C3} has to be decreased. The explanation for this is that, by reducing the distance from P_{C1} to P_{C3}, the toe is shortened, and P_{C1} is located closer to the deformation point, decreasing the magnitude of the moment created around it. Figure 4.4 shows that by moving P_{C1} closer to P_{C3}, it is now possible to fit a deformation point in the ideal area. A new shape also had to be created based on the location of this new deformation point, P_{D2}, which is drawn in Figure 4.3.

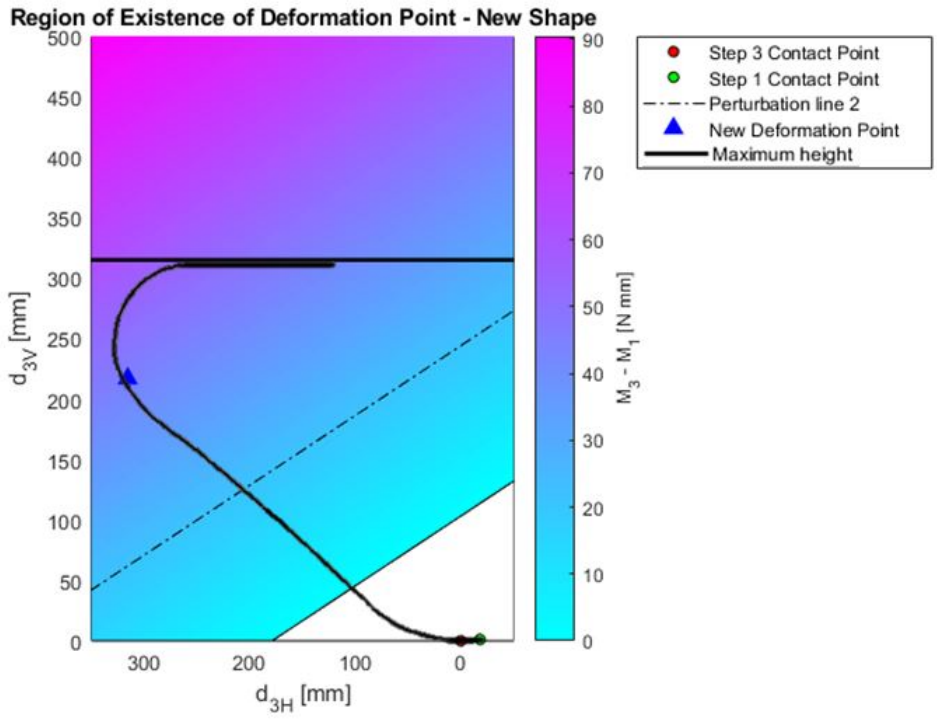

Figure 4.4: New prosthesis shape based on optimized deformation point, and size limitations. The distances between P_{C1} and P_{C3} are $d_H = 18.18mm$ and $d_V = 1.19mm$.

This new shape was inspired by the existing prosthesis of Ottobock, 1E91, but in this case with the purpose of providing a variable stiffness. It can be noticed that this design will be attached below and not behind the stump.

A comparison between the shapes the AG11 and the model of the 1E90 can be seen in Figure 4.5 below. It can be observed that the new shape of the AG11 allows positioning the deformation point further from the contact point.

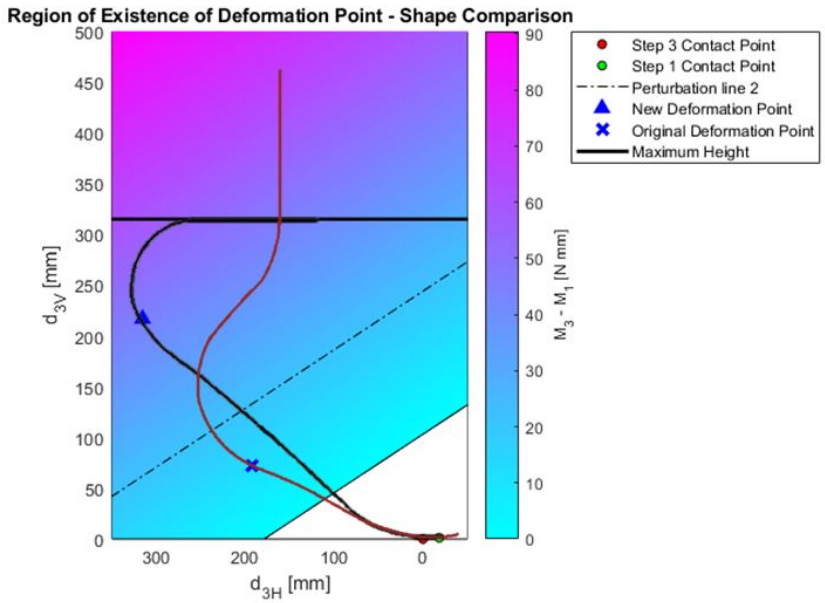

Figure 4.5: Shape comparison between the AG11 (black) and the 1E90 (red) models.

5

FEM Results

A model of the new design, the AG11, was made in FEM. The stiffness results of the new design are shown and compared to those of the model of the 1E90 from Ottobock in this chapter.

Buckling and failure analyses of the new design were also carried out. The results proving the absence of buckling or failure under the maximum loads given are shown in Appendix I.

5.1. 2D Stiffness Results

The Abaqus model was used to compute the displacements of the prostheses under several forces with different directions. These forces and displacements, which are measured with respect to the local shin reference frame, were then used for the computation of the stiffness matrices for the 3 different contact points considered (block contact point, step 1 contact point, and step 3 contact point) for the AG11 following the method explained in Section 2.1.4. The resulting stiffness matrices can be seen below.

$$K_{AG11-step1} = \begin{bmatrix} 216.52 & -149.19 \\ -149.19 & 114.55 \end{bmatrix} \tag{5.1}$$

$$K_{AG11-step3} = \begin{bmatrix} 242.47 & -182.54 \\ -182.54 & 151.1 \end{bmatrix} \tag{5.2}$$

$$K_{AG11-block} = \begin{bmatrix} 258.33 & -205.91 \\ -205.91 & 179.43 \end{bmatrix} \tag{5.3}$$

From these stiffness matrices, the stiffness ellipses of each of the contact points of each of the prostheses could be obtained as explained in Section 2.1.4. The results are shown in Figure 5.1.

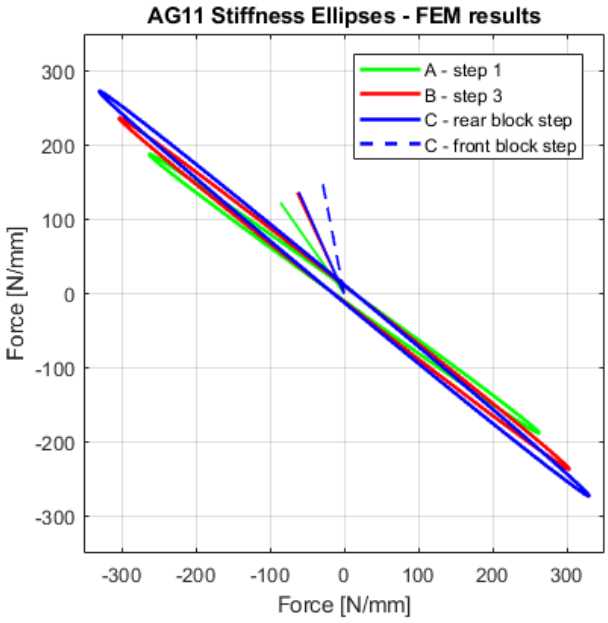

Figure 5.1: FEM results of the stiffness ellipses of the prosthesis AG11 for the 3 different contact points. P_{C1} (in green) is the contact point of step 1, P_{C3} (in red) is the contact point of step 3, and P_{CB} (in blue) is the contact point of both, rear and front block steps. The lines represent the direction of the force at each of the steps. The green line represents the force direction at step 1; the red, at step 3; the solid blue, at the rear block step; and the dotted blue line, at the front block step.

The close-up of the intersection can be seen in Figure 5.2.

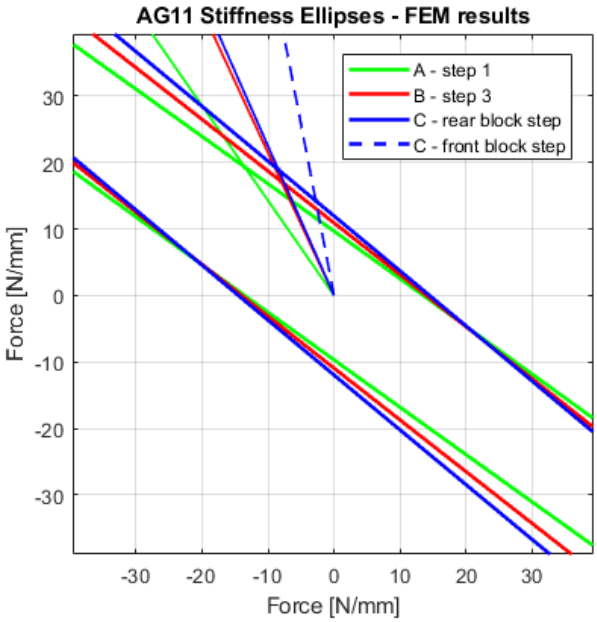

Figure 5.2: close up of the FEM results of the stiffness ellipses of the prosthesis AG11 for the 3 different contact points.

A representation of the ellipses at their corresponding contact points P_{C1}, P_{C3}, and P_{CB} of the AG11 prosthesis is shown in Figure 5.3.

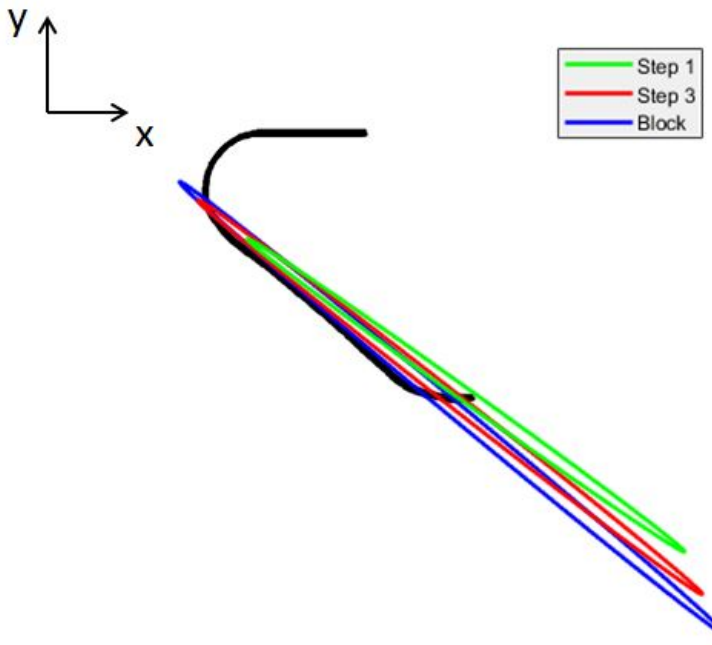

Figure 5.3: Representation of stiffness ellipses of step 1, step 3 and block contact points of the AG11, obtained from the FEM simulations.

It can be observed from Figure 5.3 that the orientation is determined by the position of the deformation area. This behavior was expected since theoretically the structure is stiffest when the force is directed towards the deformation area, creating the minimum moment. It is also noticed that the maximum stiffness increases as the contact point is closer to the deformation area. This was also expected due the decreased moment as as a consequence of reducing the distance.

Table 5.1 shows a comparison between the directional stiffness, orientation and maximum and minimum stiffness values of between the AG11 and 1E90 FEM results.

	Directional Stiffness [N/mm]		ρ [degrees]		K max [N/mm]		K min [N/mm]	
	AG11	1E90	AG11	1E90	AG11	1E90	AG11	1E90
Step 1	23.61	23.68	54.63	63.80	323.2	78.96	7.87	11.92
Step 3	18.94	23.70	52.02	55.07	384.95	140.70	8.61	12.00
Rear block	20.72	28.07	50.42	52.15	428.53	157.7	9.22	13.41
Front block	14.52	20.28	50.42	52.15	428.53	157.7	9.22	13.41

Table 5.1: Directional stiffness, orientation (rho, measured anticlockwise with respect to the y axis), maximum stiffness (major axis) and minimum stiffness (minor axis) of the AG11 and 1E90 stiffness ellipses at the 3 different contact points. These results were obtained from the FEM simulations.

From Table 5.1 it can be observed that the stiffest step provided by the 1E90 is the rear block step, followed by step 3, and then step 1. This is changed with the new design, since it provides the highest stiffness at step 1, followed by the rear block step and step 3. The stiffness at the front block step is the lowest in both designs. Thus, the aim of the model, which is to obtain a higher stiffness at step 1 than at step 3, seems to be fulfilled based on the results of the simulations.

A bigger ρ is observed for the 1E90 than for the AG11, due to the difference in the location of the deformation area. Moreover, the angle also changes accordingly for the different contact points. A larger anisotropy, due to the larger maximum stiffness, is noticed in the AG11 than in the 1E90. This could be a consequence of the thicker laminate used to simulate the AG11 compared to the laminate of the 1E90. Why a thicker laminate was needed in the model of the AG11 is explained later in this Section.

As mentioned in the introduction of this report, only the behavior of the initial steps of current prostheses should be improved. Thus, ideally, the AG11 should provide a similar stiffness at step 3 compared to the 1E90 model. As seen in Table 5.1, the stiffness in step 1 was matched instead. Thus, if the values of the directional stiffness are scaled to have a similar step 3 directional stiffness in both models, the resulting directional stiffness values of all the steps would be ones seen in Table 5.2.

	Directional Stiffness [N/mm]	
	AG11	1E90
Step 1	29.51	23.68
Step 3	23.70	23.70
Rear block	25.93	28.07
Front block	18.17	20.28

Table 5.2: Directional stiffness of AG11 and 1E90 if the directional stiffness of the AG11 is scaled to match the step 3 directional stiffness of both models.

In order to match the directional stiffness (of any step) of the AG11 model to the 1E90 model, the thickness of the AG11 model has to be increased. This happens because the deformation point is located further from the contact point in the case of the AG11 compared to the 1E90 model (this can be seen in Figure 4.5). Thus, since the lever arm is increased, the same force will lead to a bigger momentum around the AG11 deformation point, decreasing the stiffness behavior of this design. In order to compensate for this, a thicker laminate which increases the stiffness of the structure is needed. Figures 5.4 and 5.5 show the displacement along the modelled 1E90 and AG11, respectively, as a result of the deformation area.

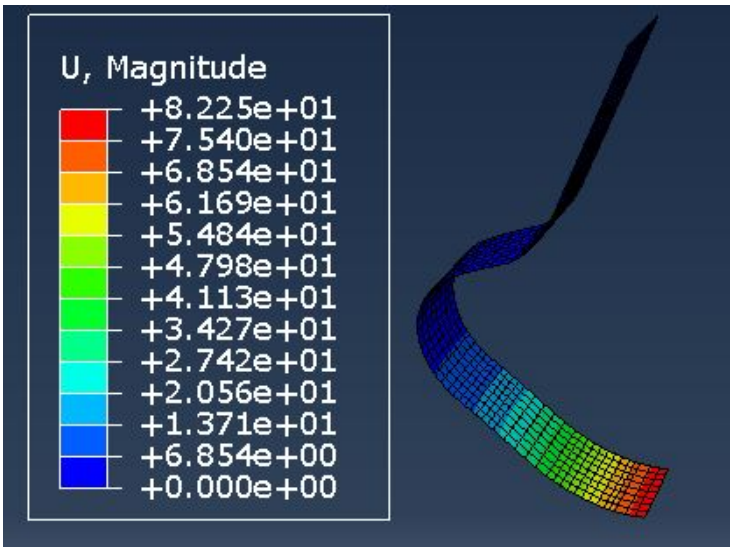

Figure 5.4: Displacement [mm] along the shape of the modelled 1E90.

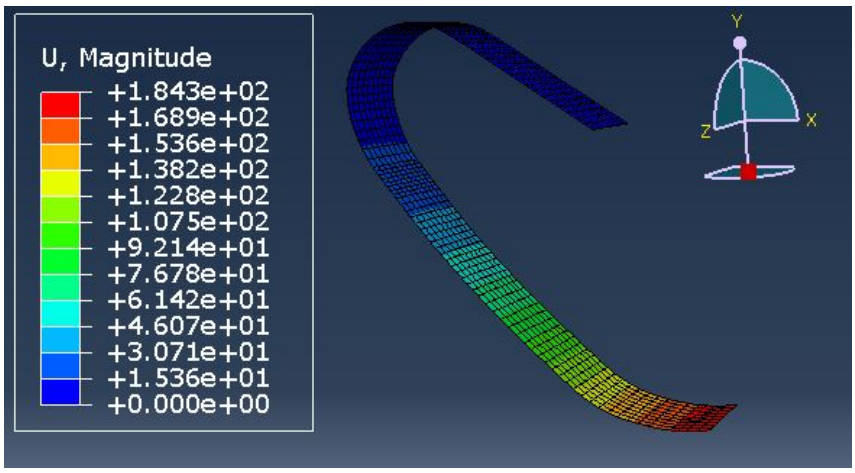

Figure 5.5: Displacement [mm] along the shape of the modelled AG11.

In this case, in order to match the step 1 directional stiffness, the thickness of the AG11 FEM model had to be increased, as seen in Table 5.3. In this table it can also be observed that the full length (from top to toe) of the AG11 is longer than that of the 1E90 modelled. This leads to an increase in the volume, and thus, in the weight of the prosthesis of about 30% compared to the modelled 1E90. Further details of the lamination of the FEM models can be found in Appendix J.

Prosthesis	Thickness [mm]	Full length [mm]	Volume [mm3]
1E90	9.12	682	350453.6
AG11	10.08	724	459043,2

Table 5.3: Thickness, full length and volume of the modelled 1E90 and AG11.

All the 2D stiffness FEM results had to be validated in the test bench and, for this, a prototype of the AG11 was created and tested together with Ottobock's 1E90.

6

AG11 Prototype Production

In order to validate the simulation results presented in the previous chapter, the AG11 was built and tested. This chapter introduces some manufacturing considerations and explains how the prototype was produced.

6.1. Manufacturing Considerations

Three different ways were considered to build the lamination of the prosthesis: prepreg, dry lamination of dry fiber, and wet lamination of dry fiber.

The term prepreg is used to address the reinforcing fabric which has been preimpregnated with the resin. Thus, the prepreg is ready to be directly laminated on the mold without adding any resin. As a consequence, areas with either an excess or a lack of resin can be avoided. Even if it ensures the best cosmetic and mechanical properties, curing at the autoclave oven is needed, what requires a very strong mold that is expensive and very time-consuming to build.

The alternative to prepreg is dry fiber. This dry fiber can be laid up either dry or wet on the mold. If a dry lay up is done, the resin has to later be infused by vacuum infusion. From previous experiences it was known that, for a large laminate thickness, placing the flow mesh on top of the product in the vacuum infusion is not sufficient to impregnate with resin the layers on the mold side. Adding a flow mesh on the mold side could solve this problem, but the risk of having a bobbly surface is increased, what is detrimental for the stiffness of the prosthesis. Therefore, a wet layup was chosen. In this case, each ply is impregnated with resin before being laid up.

Regarding the mold, either a positive or a negative mold could be used. Considering that the cosmetic side is the outer side of the prosthesis, a negative mould would have been preferred. However, due to the limited space inside, it was not possible to properly hand laminate inside the mold. Therefore, a positive mold was made.

6.2. Prototype Manufacturing

First of all, the positive mold was built. The drawing of this mold can be seen in Appendix G. The mould was machined out of a sikablock M945, which is a green polyurethane (PUR) block. Machining was preferred to decrease production times and increase the accuracy of the shape. The mold was built wide enough to create two prostheses out of the same lamination. Due to the porosity of the mold, a sealer agent was applied on the surface of the block to avoid resin absorption. Then a release agent was applied too to facilitate the release of the prostheses from the mold once finished.

The resin, which is the matrix of the laminate, supports the fibers and bonds them together in the composite material. The matrix transfers any applied loads to the fibers, and keeps the fibers in their position and chosen orientation. Thus, a proper resin distribution is very important. A 50% resin content would be ideal, but in a hand lamination this is hard to attain. A thermoset epoxy resin was used, containing Epikote (the hardener) and Epikure (the curer). The hardener and the curer were mixed in a ratio of 10:3. This mix was then impregnated on each of the plies, which were laid up over the mold one by one. The final lay up can be seen in Figure 6.1 below. The exact lamination is shown in Appendix J, together with a detailed explanation of it.

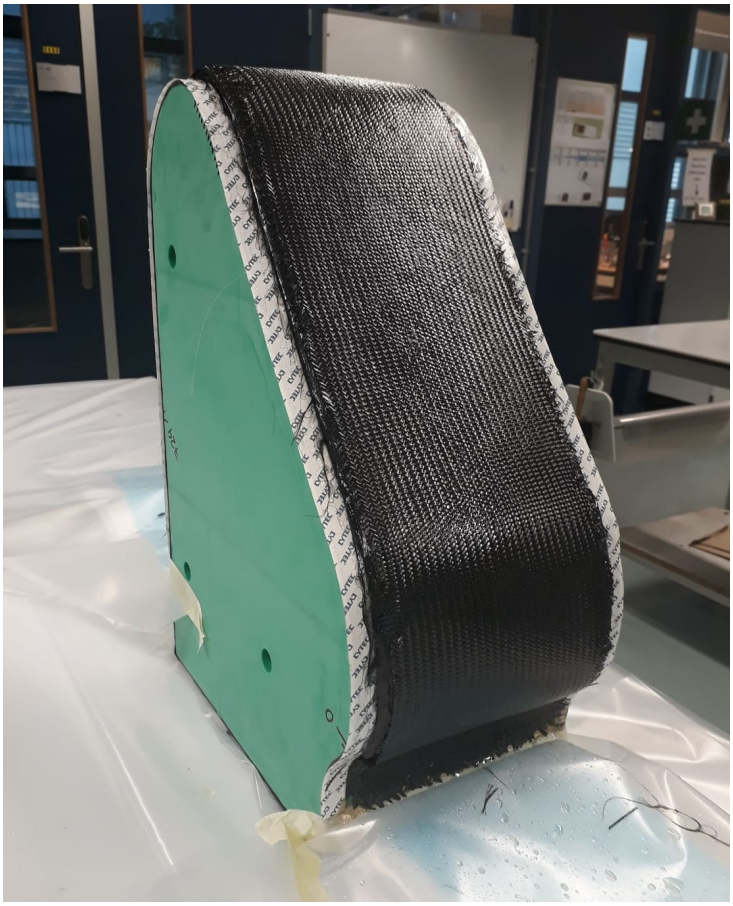

Figure 6.1: Wet lamination of dry fiber over positive mold.

The prostheses were finally left in vacuum for 24 hours, cured in the oven and cut. The final product can be seen in Figure 6.2 below.

Figure 6.2: Prototype of the AG11.

It is observed that the prototypes turned out too thick. The maximum thickness is 14mm, when it was expected to be 10.14mm. Apart from the extra thickness provided by the resin, an early curing of the resin could have also led to an increase of the thickness. Since 39 layers were individually preimpregnated in resin and laminated on the mold, before the lamination of the 39 layers was finished and the vacuum was applied, the resin on the first layers might have started curing, what prevented a proper compaction between layers, leading to voids in the structure. These voids could have also increased the thickness of the prototypes.

The laminate is formed by weave layers with ±45 degrees orientation in the top and bottom of the laminate, and UD layers with 0 degrees orientation in the middle. The exact lamination of the prosthesis can be seen in Appendix J. A weave of a nominal weight of 300g/m2 and a layer thickness of 0.26mm was used, while the UD carbon fiber used had a nominal weight of 226g/m2 and a layer thickness of 0.265mm.

7

COMPRESSION TESTS RESULTS

With the aim of validating both, the new design and the testing methodology proposed for characterizing RPs, Ottobock's 1E90 (stiffness category 4) and the new design AG11 (stiffness category 3) were tested on the static compression bench (with the set up proposed in Section 2.5, and shown in Figure 7.1). The results of the static compression tests and the 2D stiffness of the 2 prostheses are shown in this Section.

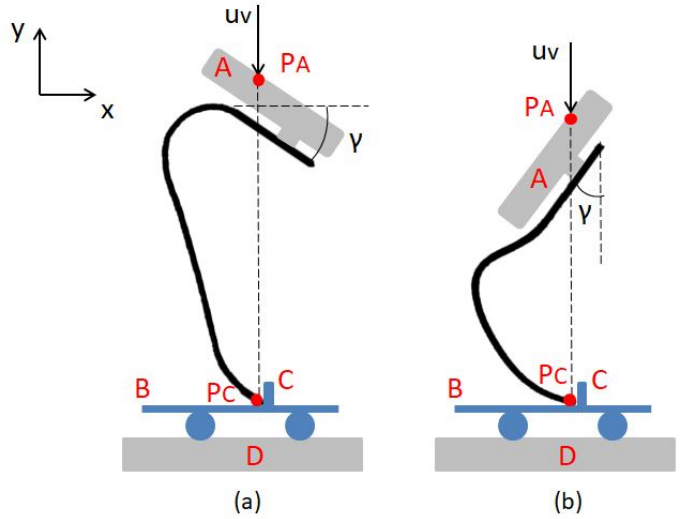

Figure 7.1: Representation of the static compression test set-up (a) for the new design and (b) for the 1E90. A is the attachment to the prosthesis that allows the rotation of the prosthesis ensuring that the point of attachment to the test bench (P_A) and the contact point (P_C) are vertically aligned. B is the slider that allows the horizontal displacement ensuring that the contact point does not change during the test. C is the vertical aluminum profile that ensures that there is no relative movement between the prosthesis and the slider. And D is the aluminum profile over which the slider translates.

7.1. TEST BENCH RESULTS

Static compression tests were carried out in order to validate the new design. In these tests a vertical displacement was applied and the force returned by the prosthesis in the vertical direction was measured. In this way, the stiffness was calculated by the test bench. Different contact points and prosthesis rotations were tested. All the tested variations are shown in Table 7.1 below.

Prosthesis	Contact Point	γ
AG11	Step 1	$-35°$
AG11	Step 3	$-25°$
1E90	Step 1	$-35°$
1E90	Step 3	$-25°$

Table 7.1: Test variations to measure the stiffness of the AG11 and 1E90 at steps 1 and 3.

The results of these tests are shown in Figures 7.2 and 7.3.

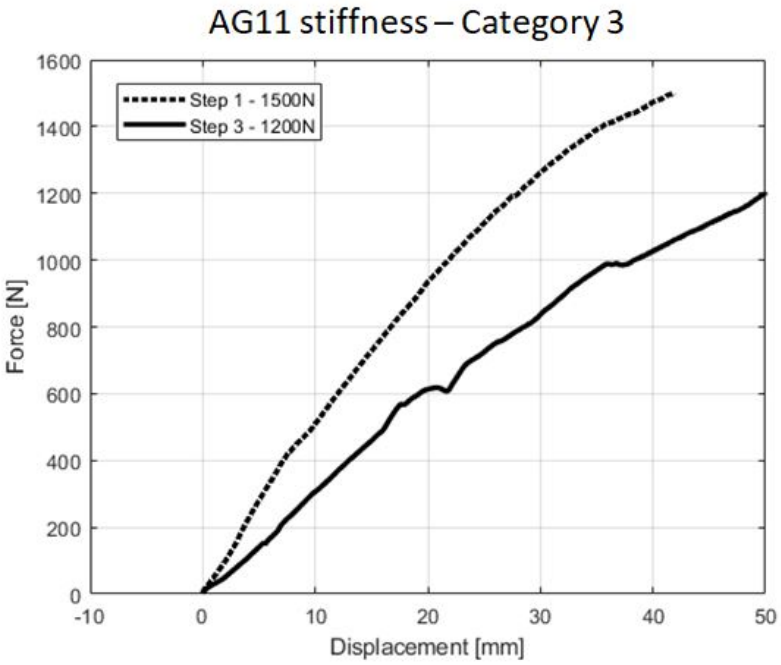

Figure 7.2: Test bench results of the stiffness for the prosthesis 1E90 in step 1 and step 3. A higher stiffness at step 1 is noticed.

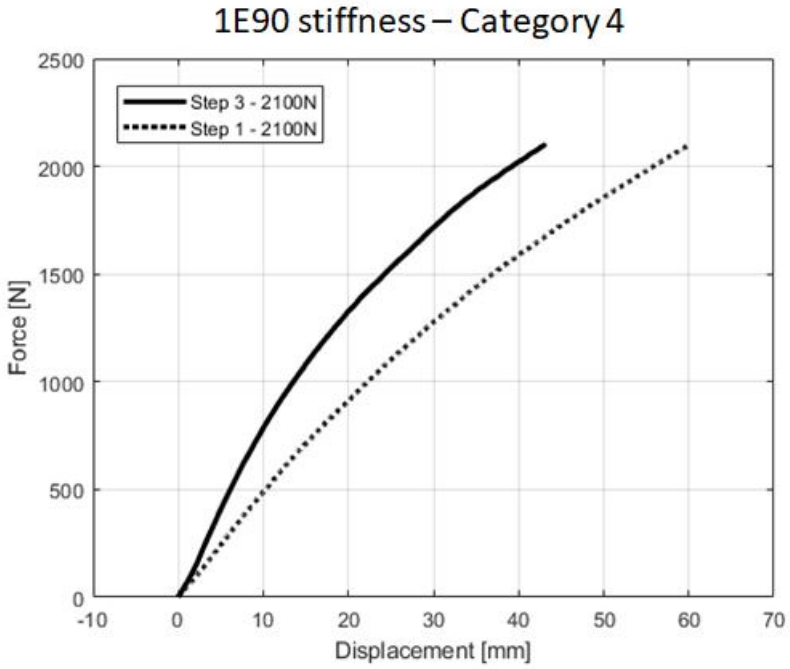

Figure 7.3: Test bench results of the stiffness for the prosthesis 1E90 in step 1 and step 3. A higher stiffness at step 3 is noticed.

From these figures it can be observed that, for the case of the AG11 prosthesis, the stiffness at step 1 is higher than that at step 3, and the opposite holds true for the 1E90. Thus, the main goal of this project is fulfilled, since a variable stiffness prosthesis with higher stiffness at step 1 compared to step 3 was built.

A non-linearity of the force-displacement relation is noticed in the last figures. This non-linearity can be explained by the increased lever arm resulting from the deflection of the prosthesis, as seen in Figure 7.4 below.

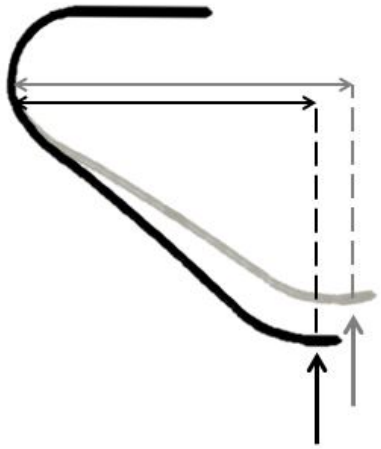

Figure 7.4: AG11 at 2 different compression stages. The black shape is the non-deformed stage, and the grey is the deformed stage. If deformed, the prosthesis has a longer lever arm. Thus, the deformed prosthesis will have a more compliant behavior.

Regardless of this non-linearity, the test bench results show that the expected variable stiffness is provided by the AG11.

7.2. STIFFNESS ELLIPSE RESULTS

In order to characterize the prostheses, the 2D stiffness was also calculated. Figure 7.5 shows one raw data set obtained from the DIC that was used to calculate the stiffness matrices. All the raw data sets can be found in Appendix K.

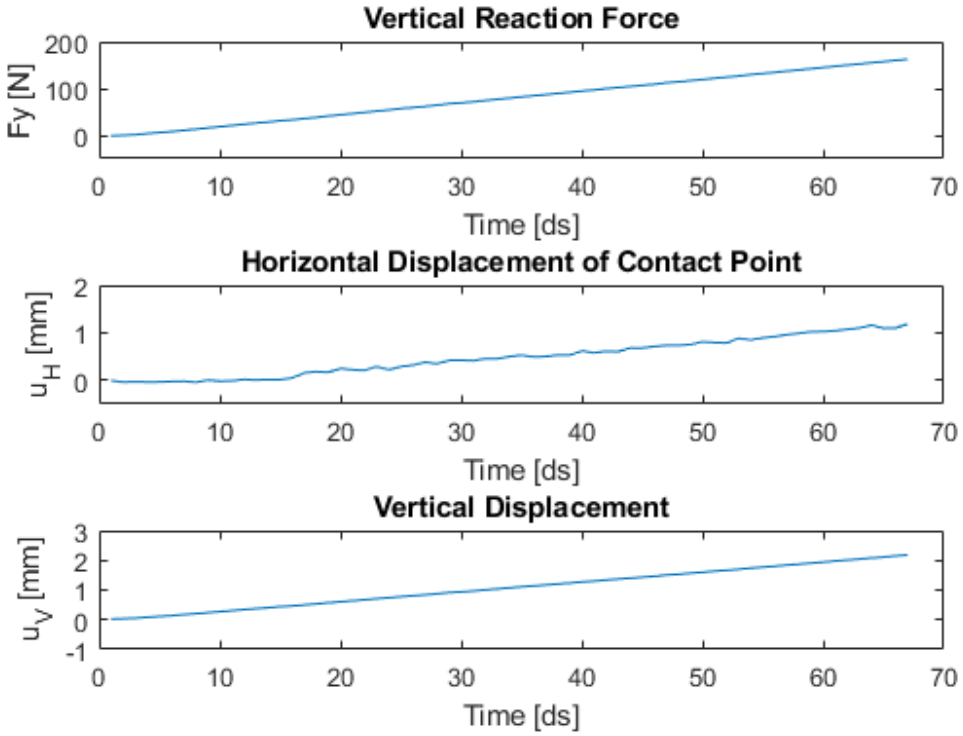

Figure 7.5: Data retrieved from the DIC. Top: vertical reaction force, f_V, as a result of the applied vertical displacement, u_V. Middle: horizontal displacement, u_H, of the contact point. Bottom: vertical displacement, u_V, of the prosthesis. It is observed that the slider starts translating ($u_H > 0$) when $f_V = 33N$. The slider starts translating at time ts=16ds.

A friction coefficient of 0.88 was measured between the slider and the aluminum profile. The effect of this friction can be seen in Figure 7.5, where the horizontal displacement of the contact point is initially constrained.

As mentioned in Section 2.5, the data in the interval $0 < t < ts$ was analyzed, i.e. when $u_H = 0$. The horizontal reaction force was assumed to be either $f_H = 0$, or $f_H = f_{Hmax}$ if the friction was considered. These forces and displacements were rotated in order to measure them with respect to the local shin reference frame: f_{x_s}, f_{y_s}, u_{x_s}, and u_{y_s}. These results were used for the retrieval of the stiffness matrices and ellipses of each of the contact points of the AG11 and 1E90.

The 2D stiffness analysis was carried out for the 3 different contact points (step 1, step 3, and block). Each contact point was tested in 3 different prosthesis inclinations, i.e. at different γ angles (see Figure 7.1 for the representation of this angle).

All the tests carried out with the different γ angles are shown in Table 7.2.

Prosthesis	Contact point	Angle 1 [deg]	Angle 2 [deg]	Angle 3 [deg]
AG11	Step 1	-32.4	-44.3	-49.2
AG11	Step 3	-26.6	-31	-39.8
AG11	Block steps	-28.8	-38.9	-
1E90	Step 1	-35.1	-46.4	-51
1E90	Step 3	-27	-32.4	-39
1E90	Block steps	-27.4	-34.4	-41.8

Table 7.2: Test variations to measure the 2D stiffness of the AG11 and 1E90 at steps 1, 3 and block steps.

The resulting stiffness matrices were non symmetric. All these stiffness matrices, for the 3 contact points of the AG11 and 1E90 considering the 2 different f_H assumptions can be seen below.

$$K_{AG11-step1-f_H=0} = \begin{bmatrix} 161.72 & -106.23 \\ 75.28 & -22.8 \end{bmatrix} \tag{7.1}$$

$$K_{AG11-step3-f_H=0} = \begin{bmatrix} 123.09 & -76.41 \\ 34.5 & 18.02 \end{bmatrix} \tag{7.2}$$

$$K_{AG11-block-f_H=0} = \begin{bmatrix} 208.34 & -183.62 \\ 81.45 & -40.77 \end{bmatrix} \tag{7.3}$$

$$K_{1E90-step1-f_H=0} = \begin{bmatrix} 127.42 & -65.71 \\ 59.3 & -2.56 \end{bmatrix} \tag{7.4}$$

$$K_{1E90-step3-f_H=0} = \begin{bmatrix} 123-44 & -103.94 \\ 43.19 & -14.06 \end{bmatrix} \tag{7.5}$$

$$K_{1E90-block-f_H=0} = \begin{bmatrix} 142.06 & -96.3 \\ 58.73 & -9.76 \end{bmatrix} \tag{7.6}$$

$$K_{AG11-step1-f_{Hmax}} = \begin{bmatrix} 148.1 & -133.46 \\ 78.31 & -32.91 \end{bmatrix} \tag{7.7}$$

$$K_{AG11-step3-f_{Hmax}} = \begin{bmatrix} 130.12 & -82.14 \\ 51.94 & 22.9 \end{bmatrix} \tag{7.8}$$

$$K_{AG11-block-f_{Hmax}} = \begin{bmatrix} 195.74 & -208.64 \\ 89.38 & -46.36 \end{bmatrix} \tag{7.9}$$

$$K_{1E90-step1-f_{Hmax}} = \begin{bmatrix} 113.74 & -85.23 \\ 52.36 & -14.25 \end{bmatrix} \tag{7.10}$$

$$K_{1E90-step3-f_{Hmax}} = \begin{bmatrix} 125.95 & -113 \\ 55.81 & -12.83 \end{bmatrix} \tag{7.11}$$

$$K_{1E90-block-f_{Hmax}} = \begin{bmatrix} 108.07 & -136.83 \\ 45.57 & -30.57 \end{bmatrix} \tag{7.12}$$

The resulting stiffness ellipses can be seen in Figures 7.6, 7.7, 7.8, and 7.9.

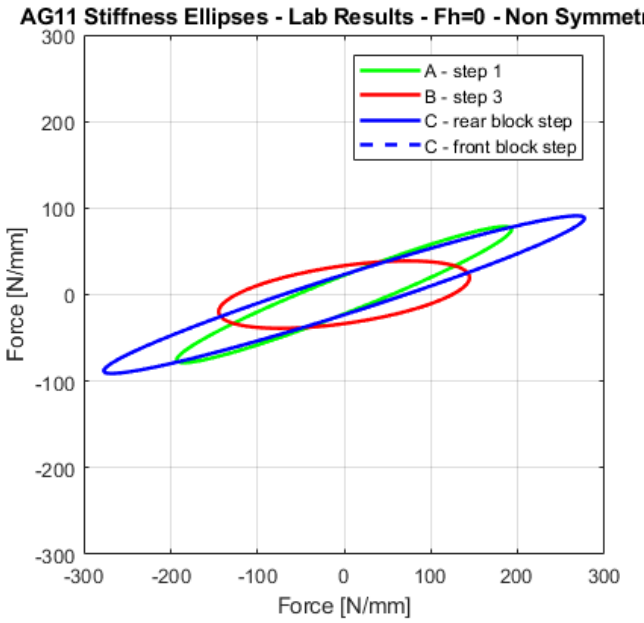

Figure 7.6: Experimental results of the stiffness ellipses (for the non symmetric matrices) of the prosthesis AG11 for the 3 different contact points for the assumption $f_H = 0$.. A (in green) is the contact point of step 1, B (in red) is the contact point of step 3, and C (in blue) is the contact point of both, rear and front block steps. The lines represent the direction of the force at each of the steps. The green line represents the force direction at step 1; the red, at step 3; the solid blue, at the rear block step; and the dotted blue line, at the front block step.

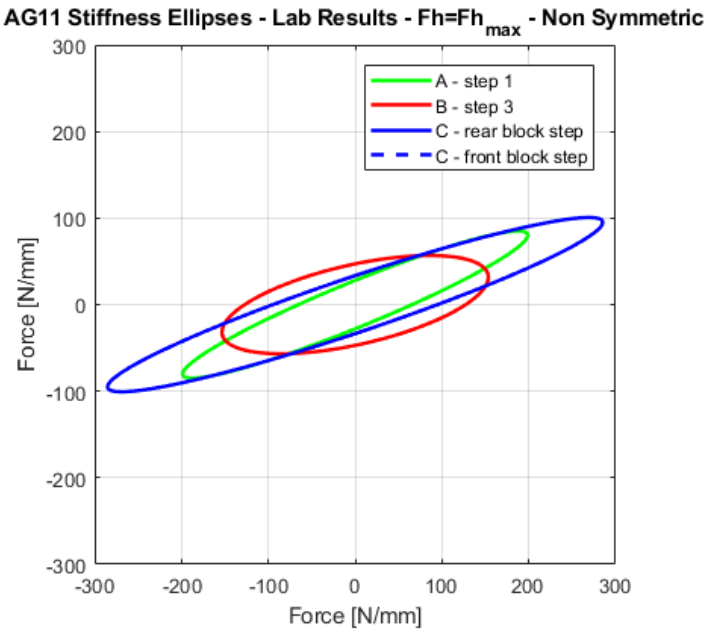

Figure 7.7: Experimental results of the stiffness ellipses (for the non symmetric matrices) of the prosthesis AG11 for the 3 different contact points for the assumption $f_H = f_{Hmax}$.. A (in green) is the contact point of step 1, B (in red) is the contact point of step 3, and C (in blue) is the contact point of both, rear and front block steps. The lines represent the direction of the force at each of the steps. The green line represents the force direction at step 1; the red, at step 3; the solid blue, at the rear block step; and the dotted blue line, at the front block step.

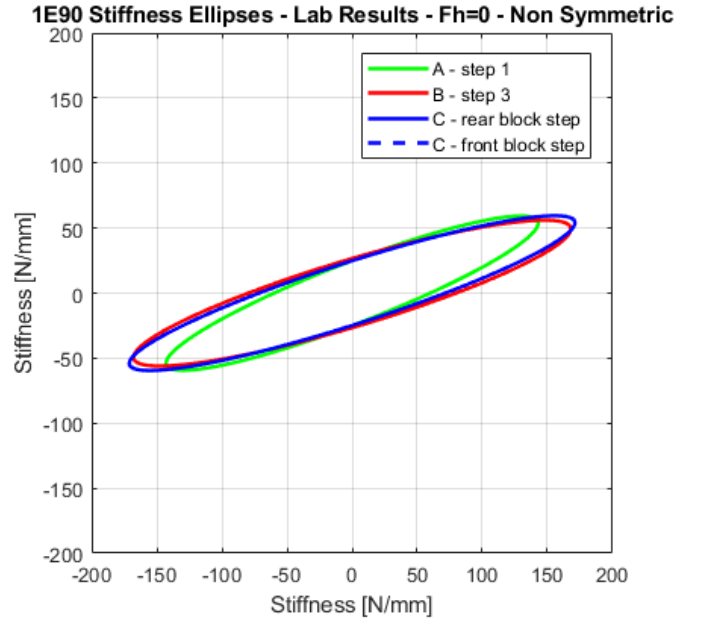

Figure 7.8: Experimental results of the stiffness ellipses (for the non symmetric matrices) of the prosthesis 1E90 for the 3 different contact points for the assumption $f_H = 0$.. A (in green) is the contact point of step 1, B (in red) is the contact point of step 3, and C (in blue) is the contact point of both, rear and front block steps. The lines represent the direction of the force at each of the steps. The green line represents the force direction at step 1; the red, at step 3; the solid blue, at the rear block step; and the dotted blue line, at the front block step.

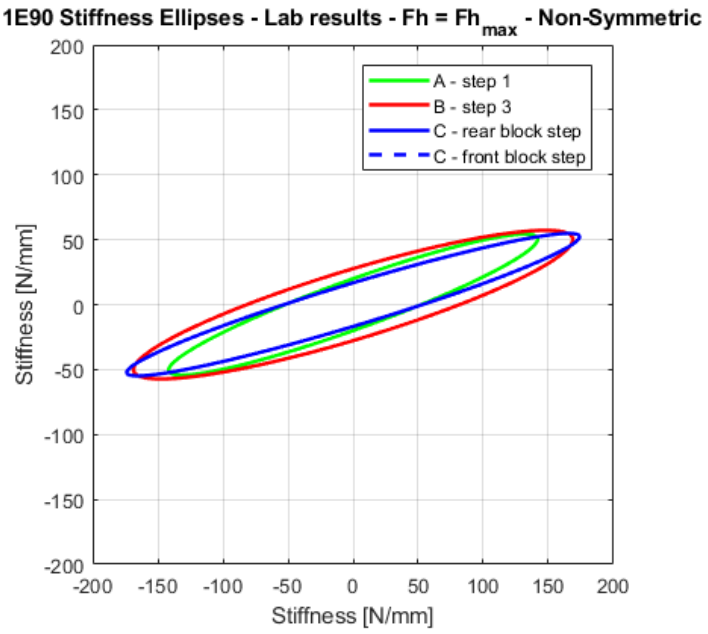

Figure 7.9: Experimental results of the stiffness ellipses (for the non symmetric matrices) of the prosthesis 1E90 for the 3 different contact points for the assumption $f_H = f_{Hmax}$.. A (in green) is the contact point of step 1, B (in red) is the contact point of step 3, and C (in blue) is the contact point of both, rear and front block steps. The lines represent the direction of the force at each of the steps. The green line represents the force direction at step 1; the red, at step 3; the solid blue, at the rear block step; and the dotted blue line, at the front block step.

It is observed that the orientation of the ellipses changes with respect to the results of the FEM simulations. rho is now negative, as it is now measured clockwise with respect to the y axis, while ρ was positive in the FEM results. This is a result of constraining the horizontal displacement, u_H, and will be further analyzed in the discussion in Section 8. It can also be observed that no relevant differences are found between the 2 f_H assumptions.

Thus, the symmetric component of the stiffness matrices was used to correct for the asymmetry and to create the stiffness ellipses [22]. The symmetric component of the stiffness matrix is calculated as follows:

$$\begin{bmatrix} k_{xx} & (k_{xy}+k_{yx})/2 \\ (k_{xy}+k_{yx})/2 & k_{yy} \end{bmatrix} \tag{7.13}$$

The symmetric matrices for each prosthesis and contact point are shown below, for the 2 different assumptions explained in Section 2.5: $f_H = 0$ and $f_H = f_{Hmax}$.

$$K_{AG11-step1-f_H=0} = \begin{bmatrix} 161.72 & -15.47 \\ -15.47 & -22.8 \end{bmatrix} \tag{7.14}$$

$$K_{AG11-step3-f_H=0} = \begin{bmatrix} 123.09 & -20.95 \\ -20.95 & 18.02 \end{bmatrix} \tag{7.15}$$

$$K_{AG11-block-f_H=0} = \begin{bmatrix} 208.34 & -51.08 \\ -51.08 & -40.77 \end{bmatrix} \tag{7.16}$$

$$K_{1E90-step1-f_H=0} = \begin{bmatrix} 127.42 & -3.2 \\ -3.2 & -2.56 \end{bmatrix} \tag{7.17}$$

$$K_{1E90-step3-f_H=0} = \begin{bmatrix} 123.44 & -30.37 \\ -30.37 & -14.06 \end{bmatrix} \tag{7.18}$$

$$K_{1E90-block-f_H=0} = \begin{bmatrix} 142.06 & -18.78 \\ -18.78 & -9.76 \end{bmatrix} \tag{7.19}$$

$$K_{1E90-step1-f_{Hmax}} = \begin{bmatrix} 113.74 & -16.44 \\ -16.44 & -14.25 \end{bmatrix} \tag{7.20}$$

$$K_{1E90-step3-f_{Hmax}} = \begin{bmatrix} 125.95 & -28.6 \\ -28.6 & -12.83 \end{bmatrix} \tag{7.21}$$

$$K_{1E90-block-f_{Hmax}} = \begin{bmatrix} 108.07 & -45.63 \\ -45.63 & -30.57 \end{bmatrix} \tag{7.22}$$

The stiffness ellipses resulting from the corrected symmetric matrices of the AG11 and 1E90 are shown in Figures 7.10, 7.11, 7.12, and 7.13.

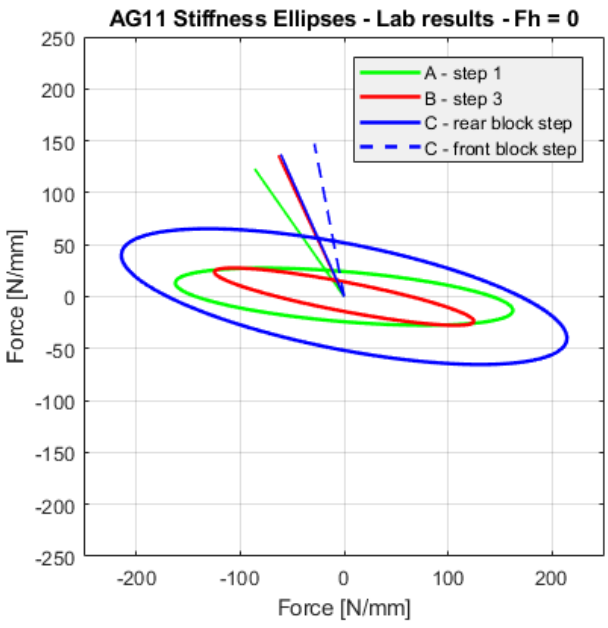

Figure 7.10: Experimental results of the stiffness ellipses of the prosthesis AG11 for the 3 different contact points for the assumption $f_H = 0$.. A (in green) is the contact point of step 1, B (in red) is the contact point of step 3, and C (in blue) is the contact point of both, rear and front block steps. The lines represent the direction of the force at each of the steps. The green line represents the force direction at step 1; the red, at step 3; the solid blue, at the rear block step; and the dotted blue line, at the front block step.

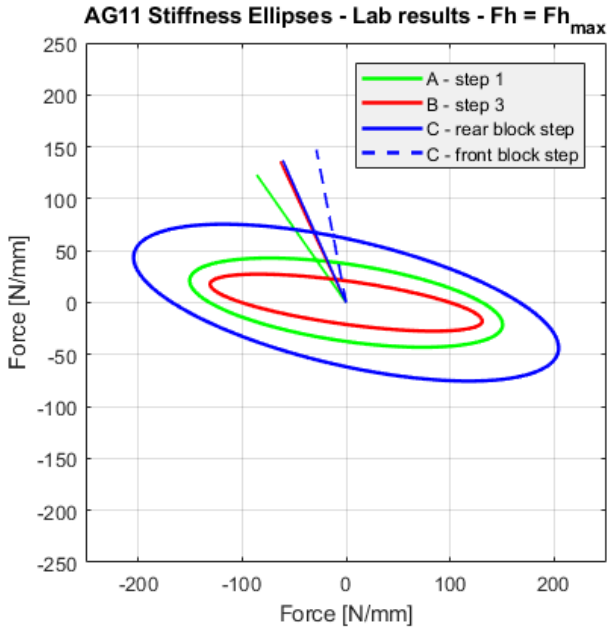

Figure 7.11: Experimental results of the stiffness ellipses of the prosthesis AG11 for the 3 different contact points for the assumption $f_H = f_{Hmax}$.. A (in green) is the contact point of step 1, B (in red) is the contact point of step 3, and C (in blue) is the contact point of both, rear and front block steps. The lines represent the direction of the force at each of the steps. The green line represents the force direction at step 1; the red, at step 3; the solid blue, at the rear block step; and the dotted blue line, at the front block step.

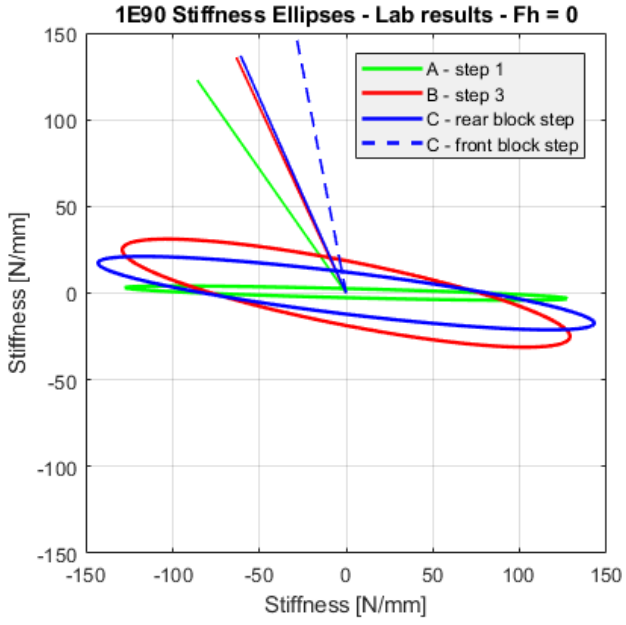

Figure 7.12: Experimental results of the stiffness ellipses of the prosthesis 1E90 for the 3 different contact points for the assumption $f_H = 0$.. A (in green) is the contact point of step 1, B (in red) is the contact point of step 3, and C (in blue) is the contact point of both, rear and front block steps. The lines represent the direction of the force at each of the steps. The green line represents the force direction at step 1; the red, at step 3; the solid blue, at the rear block step; and the dotted blue line, at the front block step.

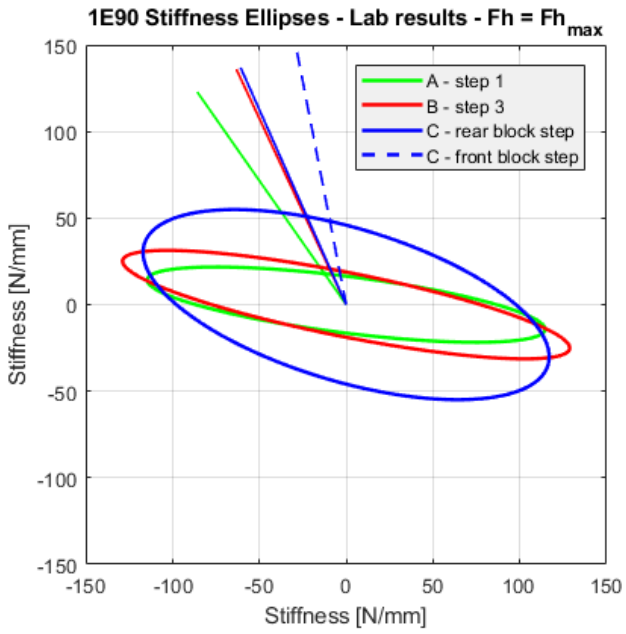

Figure 7.13: Experimental results of the stiffness ellipses of the prosthesis 1E90 for the 3 different contact points for the assumption $f_H = f_{Hmax}$.. A (in green) is the contact point of step 1, B (in red) is the contact point of step 3, and C (in blue) is the contact point of both, rear and front block steps. The lines represent the direction of the force at each of the steps. The green line represents the force direction at step 1; the red, at step 3; the solid blue, at the rear block step; and the dotted blue line, at the front block step.

A representation of the ellipses on each of the contact points is seen in Figures 7.14 and 7.15.

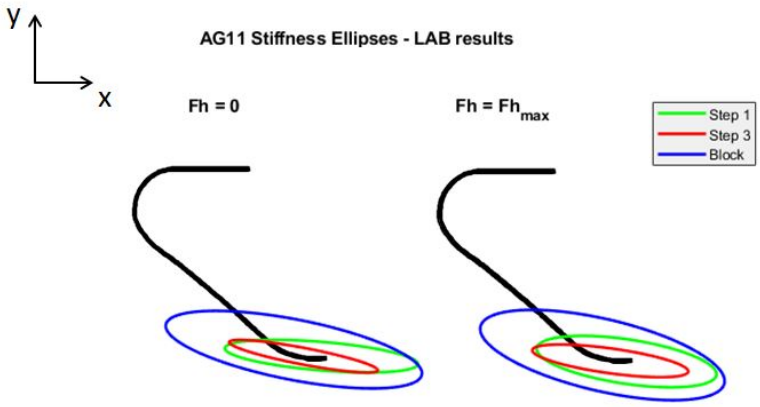

Figure 7.14: Representation of stiffness ellipses of step 1, step 3 and block contact points of the AG11, obtained from the test bench results for both assumptions: $f_H = 0$ and $f_H = f_{Hmax}$.

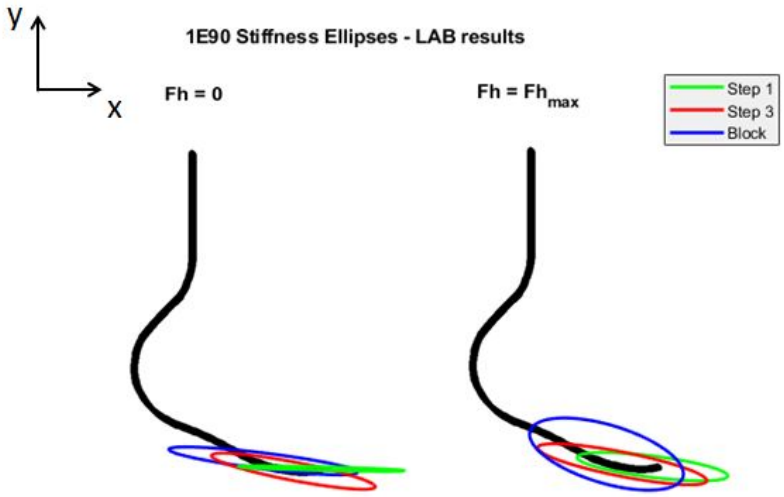

Figure 7.15: Representation of stiffness ellipses of step 1, step 3 and block contact points of the 1E90, obtained from the test bench results for both assumptions: $f_H = 0$ and $f_H = f_{Hmax}$.

It is observed that, after correcting the stiffness matrices, considerable differences are visible between the 2 f_H assumptions, mostly for the case of the 1E90.

The directional stiffness, orientation, and maximum and minimum stiffness values of the AG11 and 1E90 tests can be seen in Tables 7.3 and 7.4 below.

	Directional Stiffness [N/mm]		ρ [degrees]		K max [N/mm]		K min [N/mm]	
	AG11	1E90	AG11	1E90	AG11	1E90	AG11	1E90
Step 1	31.10	3.27	85.24	88.59	163.01	127.49	24.08	2.64
Step 3	17.22	25.42	79.13	78.08	127.19	129.86	14.00	20.47
Rear block step	61.35	14.03	78.85	83.05	218.41	144.35	50.83	12.05
Front block step	54.64	12.66	78.85	83.05	218.41	144.35	50.83	12.05

Table 7.3: Directional stiffness, orientation (rho, measured anticlockwise with respect to the y axis), maximum stiffness (major axis) and minimum stiffness (minor axis) of the AG11 and 1E90 stiffness ellipses at the 3 different contact points. These results were obtained from the tests, assuming $f_H = 0$.

	Directional Stiffness [N/mm]		ρ [degrees]		K max [N/mm]		K min [N/mm]	
	AG11	1E90	AG11	1E90	AG11	1E90	AG11	1E90
Step 1	47.71	21.86	81.53	82.80	152.21	115.82	37.02	16.33
Step 3	24.65	22.79	82.13	78.80	132.20	131.62	20.81	18.49
Rear block step	73.82	55.69	76.89	73.32	209.63	121.74	60.25	44.25
Front block step	65.47	44.08	76.89	73.32	209.63	121.74	60.25	44.25

Table 7.4: Directional stiffness, orientation (rho, measured anticlockwise with respect to the y axis), maximum stiffness (major axis) and minimum stiffness (minor axis) of the AG11 and 1E90 stiffness ellipses at the 3 different contact points. These results were obtained from the tests, assuming $f_H = f_{Hmax}$.

From Tables 7.3 and 7.4 it can be observed that, for the 1E90, the directional stiffness of the step 1 contact point at the kinematics given at this step is slightly smaller than that of the

step 3. On the contrary, for the case of the AG11, the opposite happens and the directional stiffness is higher at step 1 than at step 3. As for the block contact point, it can be seen that the stiffness at the block steps is also considerably increased in the AG11 compared to the 1E90.

This time no relation can be found between the orientation of the ellipse, the maximum and minimum stiffness, and the location of the deformation area. Only for the cases of the AG11 if $f_H = 0$, and for the 1E90 if $f_H = f_{Hmax}$, ρ, i.e. the direction of the maximum stiffness, decreases as the contact point is closer to the deformation point. Moreover, the anisotropy of these ellipses is decreased compared to the FEM results.

As for the comparison between the 2 horizontal force assumptions, big differences are perceived. It can be noticed that increasing f_H tends to decrease anisotropy and change the orientation of the ellipses by decreasing ρ. Moreover, due to the bigger vertical distance between the contact point and the deformation point in the case of the AG11 as seen in Figure 4.5, the effect of adding the f_H should further increase the differences between the experimental results of the AG11 for the different f_H assumptions compared to the 1E90. That is, bigger discrepancies should be found comparing the AG11 results from Tables 7.3 and 7.4, than comparing the 1E90 results in these tables. However, it is for the case of the 1E90 that the biggest discrepancies between the 2 horizontal force assumptions are found.

Table 7.5 shows the results of the FEM simulations. It is observed that big discrepancies are found between the simulations and the experimental results. This is due to the differences between the simulation and test conditions. While no constraints were set in the displacement of the contact point in the simulations, the horizontal displacement of the contact point was constrained ($u_H = 0$) in the tests. This led to a different behavior of the RPs. Moreover, the results differ more for the case of the 1E90 than the AG11 because the prosthesis simulated in FEM was not an exact model of the 1E90. Thus, the shape and lamination of the model differ from those of the real 1E90. Therefore, the FEM simulations cannot be validated with these tests.

	Directional Stiffness [N/mm]		ρ [degrees]		K max [N/mm]		K min [N/mm]	
	AG11	1E90	AG11	1E90	AG11	1E90	AG11	1E90
Step 1	23.61	23.68	54.63	63.80	323.2	78.96	7.87	11.92
Step 3	18.94	23.70	52.02	55.07	384.95	140.70	8.61	12.00
Rear block	20.72	28.07	50.42	52.15	428.53	157.7	9.22	13.41
Front block	14.52	20.28	50.42	52.15	428.53	157.7	9.22	13.41

Table 7.5: Directional stiffness, orientation (rho, measured anticlockwise with respect to the y axis), maximum stiffness (major axis) and minimum stiffness (minor axis) of the AG11 and 1E90 stiffness ellipses at the 3 different contact points. These results were obtained from the FEM simulations.

8

DISCUSSION

This chapter will discuss the main results obtained from this research project, which involved the validation of:
- the proposed design of a variable stiffness prosthesis, the AG11.
- the proposed method for the characterization of RPs.

8.1. AG11: THE NEW VARIABLE STIFFNESS PROSTHESIS

In this section several considerations regarding the new design will be discussed, and the future steps for the development of this design are proposed.

8.1.1. VALIDATION OF THE AG11

The main goal of this project was to design a variable stiffness prosthesis that provided a higher stiffness at step 1 compared to step 3. This goal was achieved as seen in Figure 8.1 below.

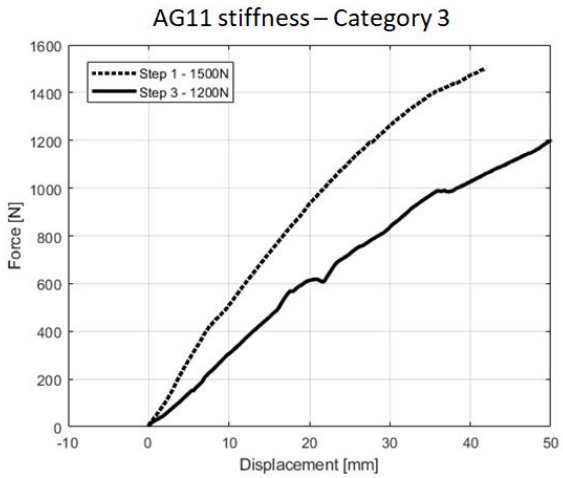

Figure 8.1: Test bench results of the stiffness for the prosthesis 1E90 in step 1 and step 3. A higher stiffness at step 1 is noticed.

Moreover, the results of the 2D stiffness also seem to validate the new design, as observed in Table 8.1. Due to the differences in the simulations and test set-up constraints, clear discrepancies are visible between the FEM and the test results. However, they both fulfill the main goal of the project, showing a successful tuning of the stiffness values at steps 1 and 3.

	FEM model	Test (f_H=0)	Test (f_H=f_{Hmax})
Step 1	23.61 N/mm	‘31.09 N/mm	49.71 N/mm
Step 3	18.94 N/mm	17.22 N/mm	24.65 N/mm

Table 8.1: Comparison of directional stiffness for steps 1 and 3 for AG11.

Table 8.1 shows the stiffness values for AG11 retrieved from the FEM model and the test on the prototype for step 1 and step 3. The test results are divided for the case of $f_h = 0$ and $f_h = f_{hmax}$, as explained in section 2.5. Even if the magnitude of the directional stiffness cannot be validated, it is clearly visible how the three results are consistent between each other, representing the same trend between the two steps.

8.1.2. ATHLETE-AG11 INTERACTION

To ensure an optimal use of the proposed design, consistent running kinematics (i.e. drive and shin angles) are demanded from the athlete. Running with constant kinematics is crucial due to the sensitivity of the design to changes in the drive and shin angles.

In order to quantify this sensitivity, a sensitivity analysis was carried out. This analysis was based on the deviations used for the definition of the new shape, seen in Appendix D. Tables 8.2 and 8.3 show the results of the sensitivity analysis for step 1 and step 3.

Table 8.2: Sensitivity study on the force orientation for step 1 for AG11, for the FEM model and the prototype modelled with $f_h = 0$ and $f_h = f_{hmax}$.

	$\gamma = 37.72^o$	$\gamma = 35^o$	$\gamma = 32.28^o$
CAD	27.28 N mm	23.60 N mm	20.84 N mm
LAB fh=0	32.36 N mm	31.09 N mm	29.98 N mm
LAB fh=fhfmax	51.83 N mm	49.70 N mm	47.82 N mm

Table 8.3: Sensitivity study on the force orientation for step 3 for AG11, for the FEM model and the prototype modelled with $f_h = 0$ and $f_h = f_{hmax}$.

	$\gamma = 27.97^o$	$\gamma = 25^o$	$\gamma = 22.03^o$
CAD	21.10 N mm	18.94 N mm	17.21 N mm
LAB fh=0	17.90 N mm	17.22 N mm	16.63 N mm
LAB fh=fhfmax	25.50 N mm	24.65 N mm	23.90 N mm

It is observed that, by changing the direction of the force applied on the prosthesis by $\pm 2.72^o$ for step 1 and $\pm 2.97^o$ for step 3, the changes in stiffness are proportional to the angle of the force, showing considerable variations between the different angles. For this reason, if the athlete does not step with the right drive and shin angles, it will result in an unexpected change of the stiffness.

However, it is expected that professional paralympic athletes run with consistent kinematics [23]. This design could also serve as an indicator of their consistency running, and

could even influence their kinematics by optimally adapting them to make the most of their tuned prostheses.

Since the shape and stiffness along the steps is changed with this new design, a learning and adaptation process is expected from the athletes before they are able to make the optimum use of this design.

8.1.3. FUTURE STEPS FOR THE DEVELOPMENT OF THE AG11

Due to the promising results obtained for the AG11, a list of future steps to further develop this design is proposed.

ITERATION OF THE DESIGN

As mentioned in Section 2.1.2, the kinematics used for the design of the AG11 were taken from videos and photos of Oscar Pistorius. Thus, it is suggested to measure the GRF and shin angle of the athletes, and iterate the design considering the new parameters. It should be considered that, unless a general pattern is found in all the athletes, the design should be optimized and fitted for each athlete individually. Moreover, once the ideal stiffness values are known, the design has to be tuned accordingly. The new prototype should then be tested by athletes on the field, and the design should be iterated until an optimum design for the athlete is reached.

FIELD TESTING

In order to know the real behavior of RPs, field tests are needed. By means of force plates the GRF could be measured. Making use of the optic fiber technology, the stiffness and shin angle could also be retrieved. Moreover, the change of stiffness during rollover could be understood. This is difficult to predict now due to the fact that both, deflection and rollover, occur simultaneously after initial contact. Thus, field testing with the optic fiber technology could greatly enhance our understanding on the behavior of RPs in the field.

RP WEIGHT REDUCTION

Since the deformation point of the AG11 is further from the contact points compared to the 1E90, a thicker lamination was needed to provide the same stiffness as other current RPs. This considerably increases the weight of the prostheses. Several researches assert that the mass of RPs has a considerable effect on joint kinetics or kinematics during stance and swing phase [24, 25]. If the mass of RPs is increased, a higher muscular work is required and more energy is spent in the leg swing [21]. Moreover, increasing the mass leads to slower leg swings, leading to longer swing times, and lower stride frequencies [26]. Thus, in order to reduce the weight of this design, the use of a sandwich composite is proposed. This material is made by attaching two thin but stiff skins of carbon fiber to a lightweight but thick core, which could be made of foam. Since the carbon fiber layers are the furthest from the neutral axis, the high stiffness is maintained, while decreasing the overall weight of the structure.

OPTIMIZATION OF THE LAMINATION

The desired bending and torsional stiffness should be found, and the lamination should be chosen accordingly. It should be considered that there is only straight running in 100 meters races, but races from 200 meters on also include curve running. It could be possible that a decreased torsional stiffness is more suitable for curve running. Thus, different torsional stiffness may be desired for the different races, what leads to different prosthesis laminations too.

OPTIMIZATION OF GRF DIRECTION

Current prosthetic companies design prostheses that return a GRF as vertical as possible. This is achieved by modifying the lamination as explained in Chapter 3. From the performance perspective, the vertical GRF should be large enough to counteract gravity, and it is the horizontal GRF that should be as large as possible. A high horizontal GRF is preferred to increase forward propulsion [27], since it decreases aerial times and increases the step frequency. However, a GRF with a large horizontal component, also results in a backwards moment around the CoM. This moment causes a fast raise of the CoM, what limits forward acceleration. Bearing this in mind, it is suggested to match the direction of the GRF with the drive angle, in order to direct the GRF towards the CoM, optimizing the acceleration performance. Thus, the GRF direction is a parameter that could be introduced in the iterations, in order to analyze the effect of the shape and stiffness of the prostheses on both, the GRF direction and drive angle. This way, the optimum shape that aligns them both could be found.

MANUFACTURING CONSIDERATIONS

A better prototype production in order to avoid the bobbly surfaces and the unexpected increased thickness is suggested. The use of prepreg instead of dry lamination, followed by curing at the autoclave would ensure the best finish and properties of the prostheses.

8.2. VALIDATION OF TESTING METHODOLOGY

In this section the validity of the proposed testing methodology will be discussed, and the future steps needed for the proper characterization of RPs will be recommended.

As a consequence of the presence of friction, the conditions of the tests were not matched to those of the FEM simulations. The friction present in the tests did not allow the horizontal displacement of the contact point. Thus, the FEM simulations could not be validated. In order to investigate the contribution of the displacement constraint on the stiffness matrix, the same conditions as in the tests were simulated in FEM for the step 1 contact point, constraining the horizontal displacement of this point. From this simulation a non symmetric stiffness matrix for the step 1 contact point was obtained, as seen below.

$$K_{AG11-step1-u_H=0} = \begin{bmatrix} 506.68 & -285.35 \\ 209.18 & 185.7 \end{bmatrix} \tag{8.1}$$

This simulation is in accordance with the tests and predicts the non symmetric matrices retrieved from the tests.

Figure 8.2 shows the FEM results of the modulus of the displacement of the AG11 if the horizontal displacement of the contact point is constrained, and Figure 8.3, if the displacement is not constrained. It is observed that buckling happens if the horizontal displacement is constrained.

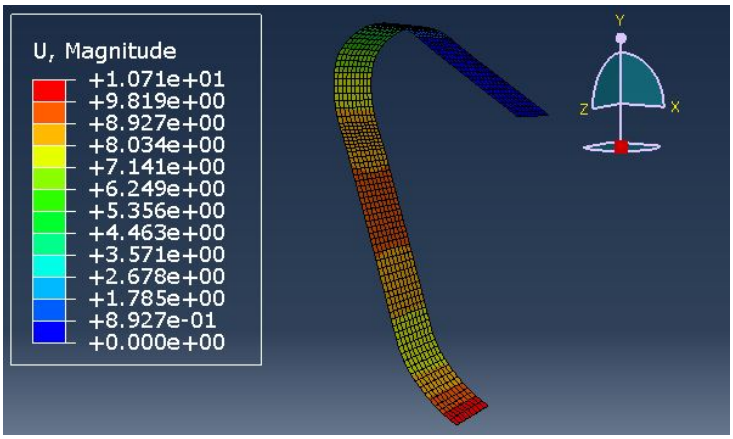

Figure 8.2: Modulus [mm] of the displacements in the modelled AG11 constrained at the contact point.

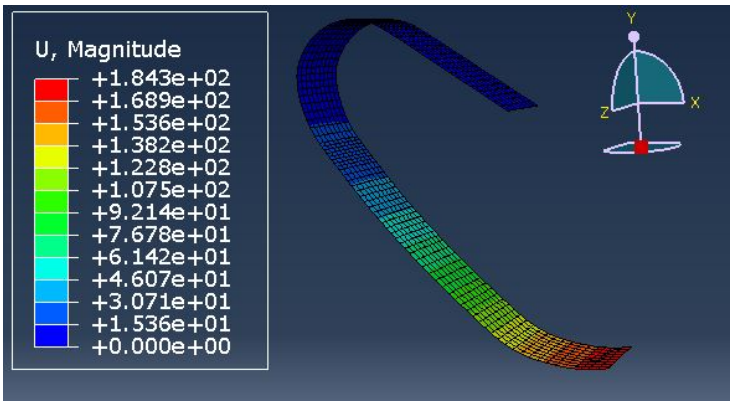

Figure 8.3: Modulus [mm] of the displacements in the modelled AG11 without any constraint at the contact point.

Figures 8.4 and 8.5 show, respectively, the horizontal and vertical displacements resulting from the constrained simulation, and Figures 8.6 and 8.7, those of the non constrained simulations. The buckling in the constrained simulations can be noticed by the observed unusual negative horizontal displacement in the middle part of the prosthesis, which is not present in the non constrained simulations, and is therefore a result of constraining the two ends of the prosthesis.

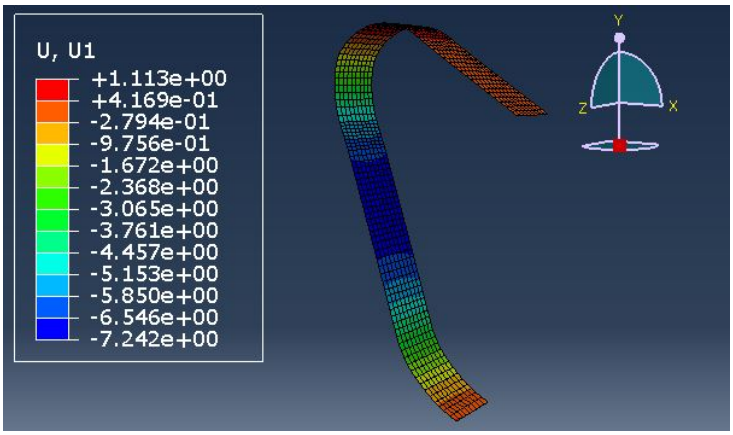

Figure 8.4: Displacement [mm] in the modelled AG11 in the horizontal direction, constrained at the contact point at step 1.

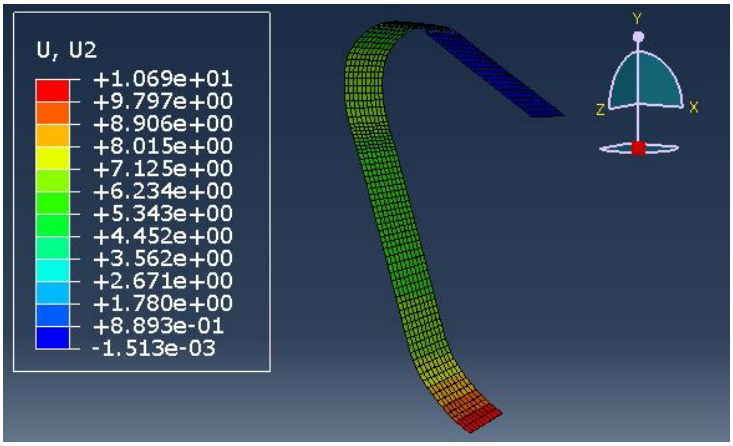

Figure 8.5: Displacement [mm] in the modelled AG11 in the vertical direction, constrained at the contact point.

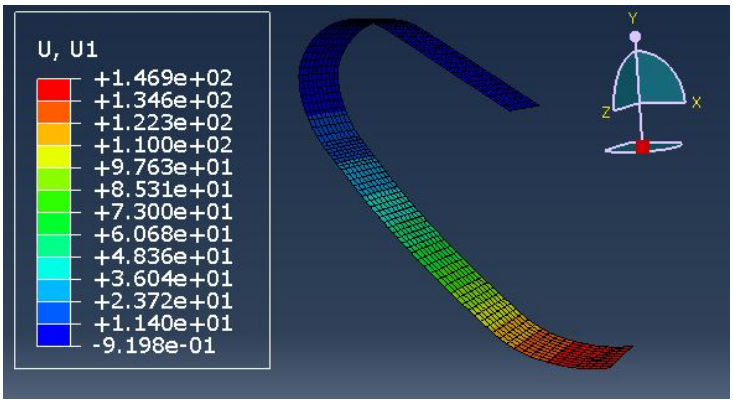

Figure 8.6: Displacement [mm] in the modelled AG11 in the horizontal direction, with no constraints in the contact point.

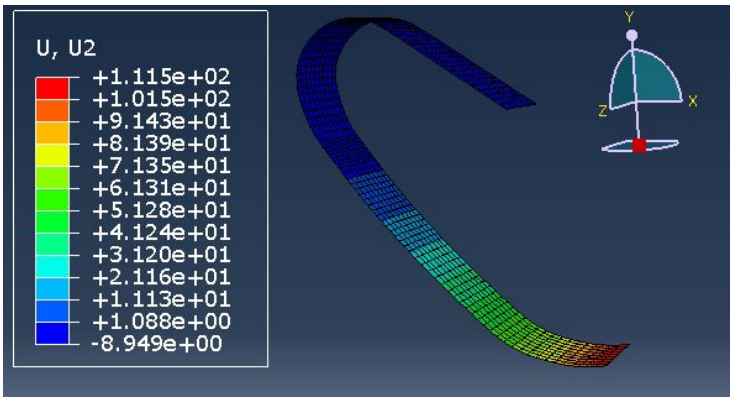

Figure 8.7: Displacement [mm] in the modelled AG11 in the vertical direction, with no constraints in the contact point.

In order to correct for this phenomenon, the symmetric component of the stiffness matrix was calculated.

$$K_{AG11-step1-u_H=0-sym} = \begin{bmatrix} 506.68 & -38.08 \\ -38.08 & 185.7 \end{bmatrix} \tag{8.2}$$

Figure 8.9 shows the stiffness ellipses of the non symmetric and the corrected matrices of the constrained simulation. The same behavior as in the performed tests is observed: the non symmetric matrix leads to an ellipse with a negative ρ, while the corrected matrix results in an ellipse with positive ρ.

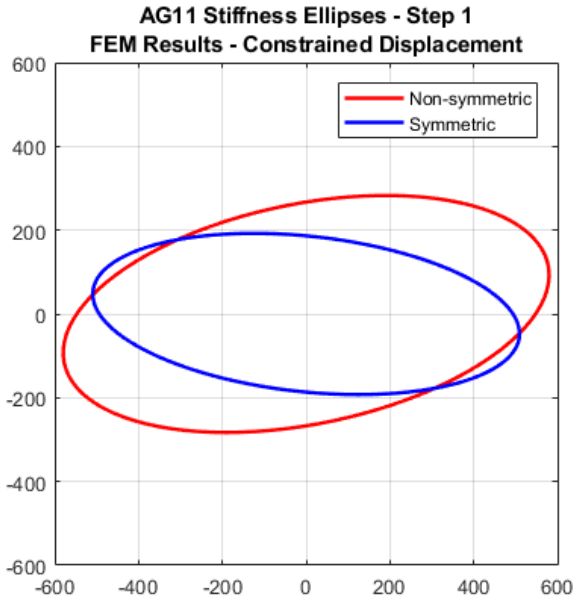

Figure 8.8: Comparison between symmetric and non-symmetric stiffness ellipses from FEM simulation. The AG11 CAD model is used at step 1. The non-symmetric stiffness matrix is represented by the red ellipse, the symmetric stiffness matrix by the ellipse in blue.

Figure 8.8 compares the stiffness ellipses of the step 1 contact point resulting from the FEM simulations with (solid line) and without (dotted line) constraint. It can be seen that the

corrected stiffness matrix does not lead to the same ellipse obtained from the unconstrained simulation.

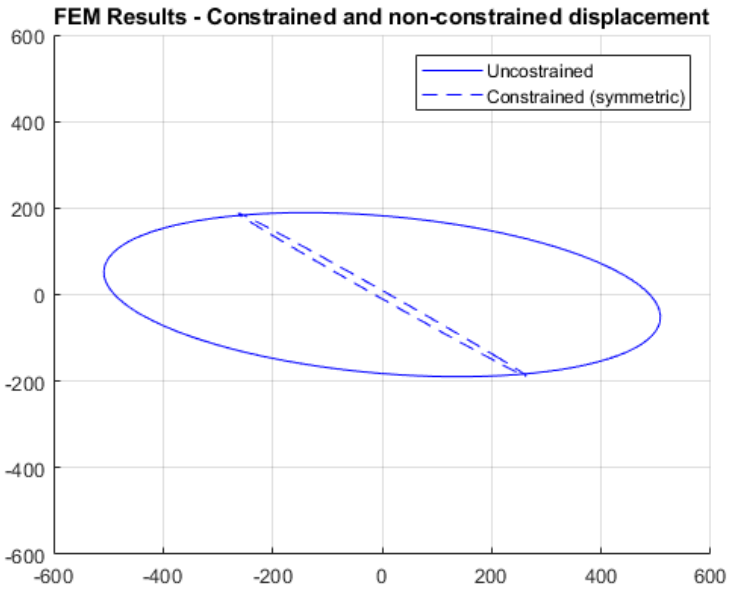

Figure 8.9: Stiffness ellipses from the FEM simulation with and without constraints on the horizontal displacement. The AG11 CAD model is used at step 1.

These results suggest that constraining the displacement of the contact point and correcting the non symmetric stiffness matrices using the symmetric component is not a valid method for the characterization of RPs. Besides this, it is still possible to observe from the tests results that, even if the stiffness ellipses are retrieved by constraining the horizontal displacement, the directional stiffness is still higher at step 1 than at step 3.

8.2.1. FUTURE STEPS FOR THE CHARACTERIZATION OF RPS

TEST SET UP FOR RP CHARACTERIZATION

It was initially believed that clamping the prostheses would be the best way to characterize them. In this project it was shown that this leads to buckling of the structure, what results in non symmetric stiffness ellipses and inhibits a proper characterization of the RPs. Thus, testing the RPs without constraining the displacement of the contact point is suggested. For this, the friction of the slider should be minimized. It was noticed that the slider used during the tests provided too much friction because one of the wheels was not rotating, but simply translating. Thus, by using a slider with properly rotating wheels, the friction would considerably decrease and a proper characterization of the RPs could be carried out.

NOISE REDUCTION

The presence of noise decreases the accuracy of the measurements. In order to approximate as much as possible a linear behavior, and also limited by the friction force, very small displacements were used (between 0.5 and 2 mm of vertical displacement). Considering that the noise level was around 0.2 mm (as observed in Figure 8.10), it is expected to be a major contributor to errors in the retrieval of the stiffness matrices.

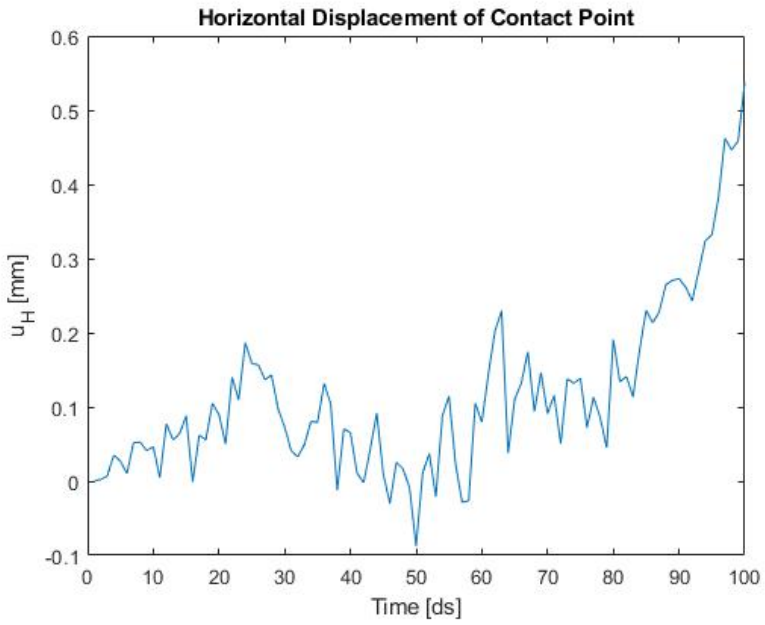

Figure 8.10: Noise in horizontal displacement DIC measurements.

In order to reduce the weight of the noise on the measurements, two solutions are proposed. The first one consists of reducing the noise in the measurements by having a better focus, more light, and bigger speckles. The second one consists of putting the cameras closer to the contact point. Due to the big dimensions of the prostheses, in order to fit the full structure in the pictures, the cameras had to be placed far from the prostheses. Thus, placing some cameras closer to the main area of interest of the RPS, bigger speckles and a better focus could automatically be obtained without the need of better cameras. Since recordings of the whole structure are also needed to compute the vertical displacement, the use of two sets of cameras is suggested, placing one in front and one behind the prosthesis, as seen in Figure 8.11.

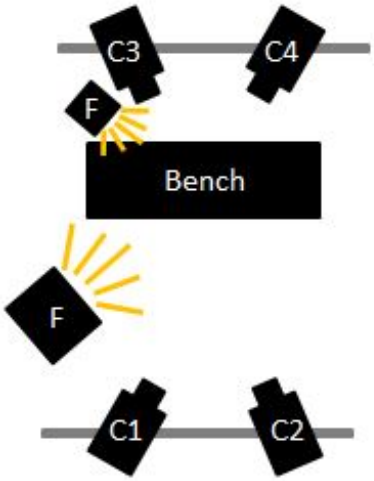

Figure 8.11: Suggested new DIC set-up. The use of 2 camera sets is recommended. One set (C1-C2) should be put far from the bench in order to capture the whole structure in the recordings, while the second set (C3-C4) should be put close to the contact point in order to properly record its displacement.

A proper synchronization of both camera sets, as well as with the test bench, is required. It must be considered that now different flash units will be required, what means that a proper positioning of these units is important to avoid backlighting, which would reduce the visibility of the speckles.

STATISTICAL VALIDATION

The use of a little amount of data sets could also be a source of error. Thus, increasing the number of tests done for each configuration (the configurations used are seen in Table 7.2) would lead to a more robust characterization of the prostheses with a high statistical significance.

9

CONCLUSION

The two goals of this project were: 1. to design a new variable stiffness prosthesis, and 2. to create a new methodology for the characterization, i.e. stiffness ellipse retrieval, of RPs.

Current prosthetic companies successfully make use of the Deflection Direction Method in order to tune the deflection direction of their RPs. Inspired by this method, a new method was created (the Deformation Point Method), which allows the tuning of the location of the deformation point in order to provide a variable stiffness in the different acceleration steps, which is dependent on the kinematics of the athlete.

While current prosthesis provide a higher stiffness at step 3 than at step 1, the AG11 proved to successfully provide a higher stiffness at step 1 than at step 3. Unlike the inverse prosthesis, the AG11 provides a positive horizontal GRF. Since the deformation point is located posterior to the contact point, a deflection in the positive horizontal direction is obtained.

Regarding the interaction with the athlete, it is known that the compliance of current RPs hamper the acceleration performance of BTAs. With the AG11, the stiffness during the first steps is increased, what leads to a higher forward propulsion by decreasing contact times and increasing GRFs and step frequencies. It must be considered that a learning process is required from the athlete in order to make the best use of the new design. But after the required design iterations and a successful learning process of the athlete, the new design will result in considerable improvements on the acceleration performance, and thus, in the total 100 meters time.

Finally, regarding the second goal of this project, the methodology proposed for the retrieval of the stiffness matrices and ellipses cannot be concluded to be a valid methodology for the characterization of RPs. It is thus recommended that the characterization of RPs is carried out without constraining the displacement of the contact point.

Appendices

A

INVERSE PROSTHESIS

The determination of the direction of the GRF of the inverse prosthesis can be observed in Figure A.1, and it is compared to the GRF direction provided by a forward prosthesis seen in Figure A.2. For the sake of the validity of the comparison, the same contact point with respect to the stump (same distance d between contact point and stump) was chosen for the inverse and for the forward prostheses representation. Rollover and blade deformations were not considered.

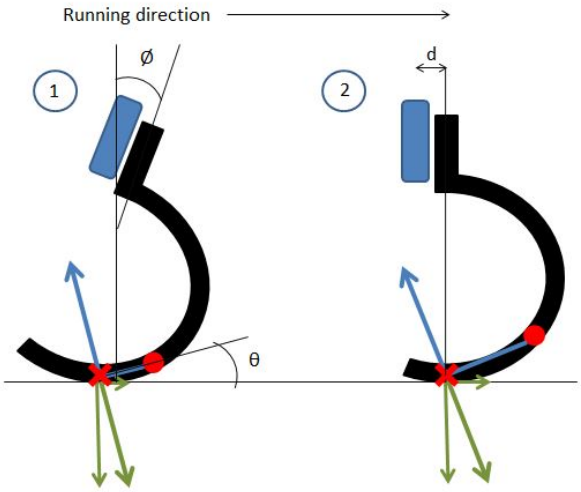

Figure A.1: Representation of GRF on an inverse prosthesis. d is the distance between the contact point and the stump. Situation 1 describes the initial contact at a start step and situation 2, at a steady step. The red dot is the deflection point of the prosthesis, the red cross is the contact point, Θ is the angle between the ground and the line containing the contact and the deflection point, the blue arrow is the deformation direction, the green thick arrow is the force exerted by the spring on the ground, and the green thin arrows are the horizontal and vertical components of the force exerted by the spring on the ground. Following Newton's third law, the GRF will be equal and opposite to the force exerted by the spring on the ground; thus, the direction of the GRF matches the deformation direction of the contact point. It is observed that the force returned to the athlete has a horizontal component opposite to the running direction.

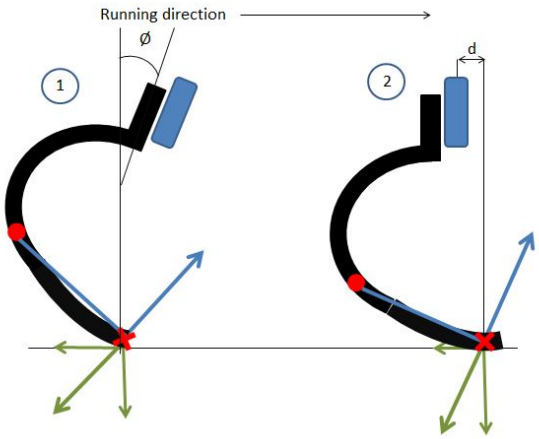

Figure A.2: Representation of GRF on a steady step with a forward prosthesis. d is the distance between the contact point and the stump. Situation 1 describes the initial contact at a start step and situation 2, at a steady step. The red dot is the deflection point of the prosthesis, the red cross is the contact point, the blue arrow is the deformation direction, the green thick arrow is the force exerted by the spring on the ground, and the green thin arrows are the horizontal and vertical components of the force exerted by the spring on the ground. Following Newton's third law, the GRF will be equal and opposite to the force exerted by the spring on the ground; thus, the direction of the GRF matches the deformation direction of the contact point. It is observed that the force returned to the athlete has a horizontal component in the running direction.

It can be observed in Figure A.1 that the force returned to the athlete has a horizontal component opposite to the running direction. For this negative horizontal force to be avoided the contact and deflection points should be aligned, i.e. Θ in Figure A.1 should be zero. This would mean that the deflection point is also the contact point, what is not possible; moreover, in this situation then the GRF would be completely vertical. Since the contact point cannot be on the right side (for a running direction to the right) of the deflection point, no positive horizontal force from the ground is possible for the case of the inverse prosthesis. As noticeable looking at Figure A.2, the force returned to the athlete wearing a forward prosthesis has a horizontal component in the running direction. This happens because the contact point is on the right side of the deflection point (for a running direction to the right).

In order to validate these hypotheses, the inverse prosthesis was modelled in Abaqus. The model is shown in Figure A.3.

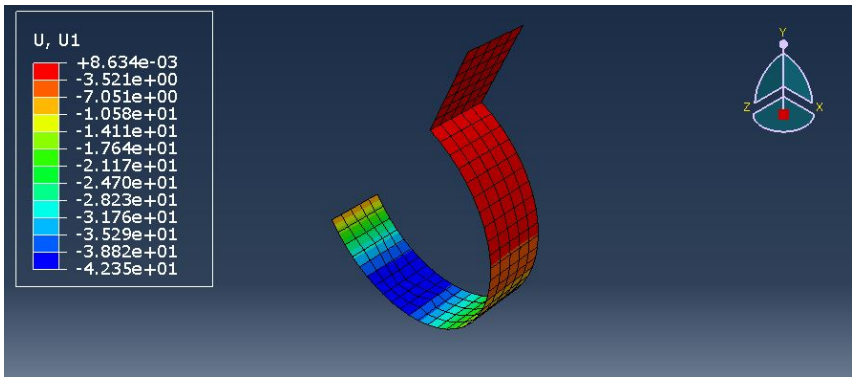

Figure A.3: Inverse prosthesis model. The results of the negative horizontal displacement are shown.

The directional stiffness and the direction of the deformation of the contact point were

calculated. The latter which had to be measured with respect to the global reference frame in the real position of the prosthesis (see Figure A.4(b)). For this, knowing that the simulations were run in the configuration shown in A.4(a), the deformation direction had to be rotated back an angle equal to the drive angle, as seen in A.4(b).

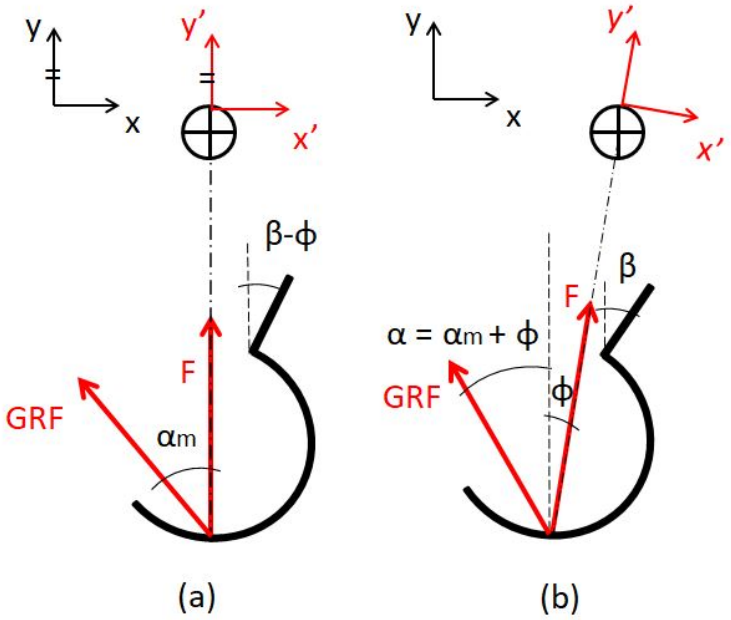

Figure A.4: (a) Rotation of the system to match the local reference frame defined by the force direction with the global reference frame. These are the conditions set for the simulations; thus, α_m (<0) is the deformation direction of the contact point resulting from the simulation. (b) Representation of the real positioning of the prosthesis at the initial contact point. α_m has to be rotated an angle ϕ (the drive angle) in order to obtain the deformation direction given in the real situation. The angle α is measured from the vertical and it is positive if clockwise.

The results of the FEM simulations of 1D stiffness, k, and GRF direction, α, for step 1 and steady step are shown in Table A.1.

	k [N/mm]	α [deg]
Step 1	126.04	-23.98
Steady step	28.63	-39.02

Table A.1: 1D stiffness and GRF direction provided by the inverse prosthesis at step 1 and steady step.

B

Shin and Drive Angles

In the human body, when standing in the anatomical position, the CoM is located anterior to the second sacral vertebra. Its location changes for the case of amputees, due to the loss of their limbs. For the case of BTAs the CoM is located at the connection between the lumbar and thoracic vertebrae. The CoM position of healthy subjects and amputee subjects is depicted in Figure B.1 below.

Figure B.1: Diagrammatic representation of the influence of amputation of lower extremities of the height of the CoM [28].

Based on this, the drive angle, together with the shin angle, of the block steps, the first two start steps and a steady were measured from pictures of Oscar Pistorius.

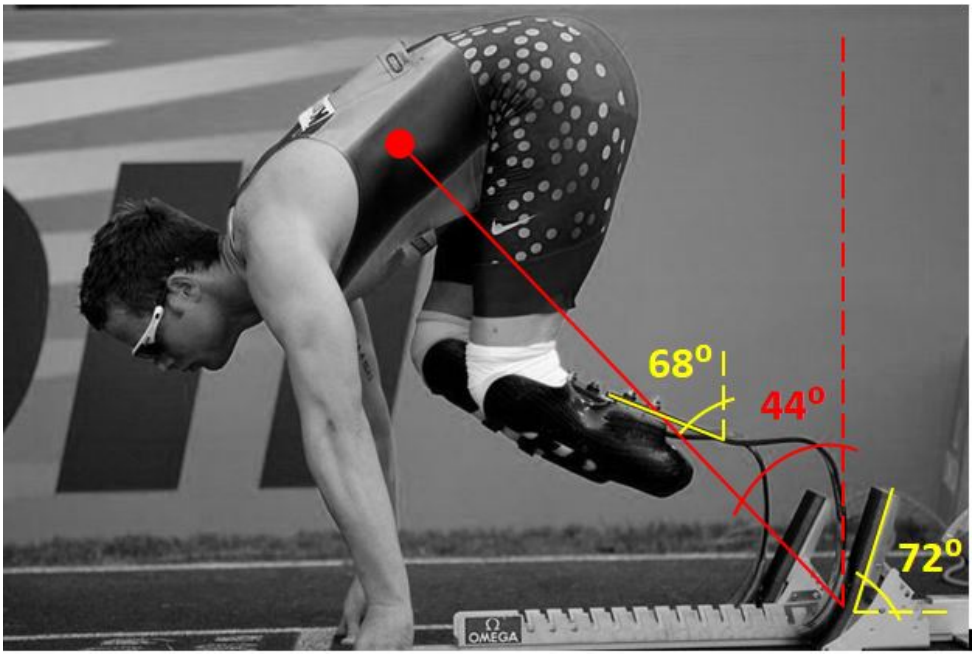

Figure B.2: Shin, drive and block angles at rear block step.

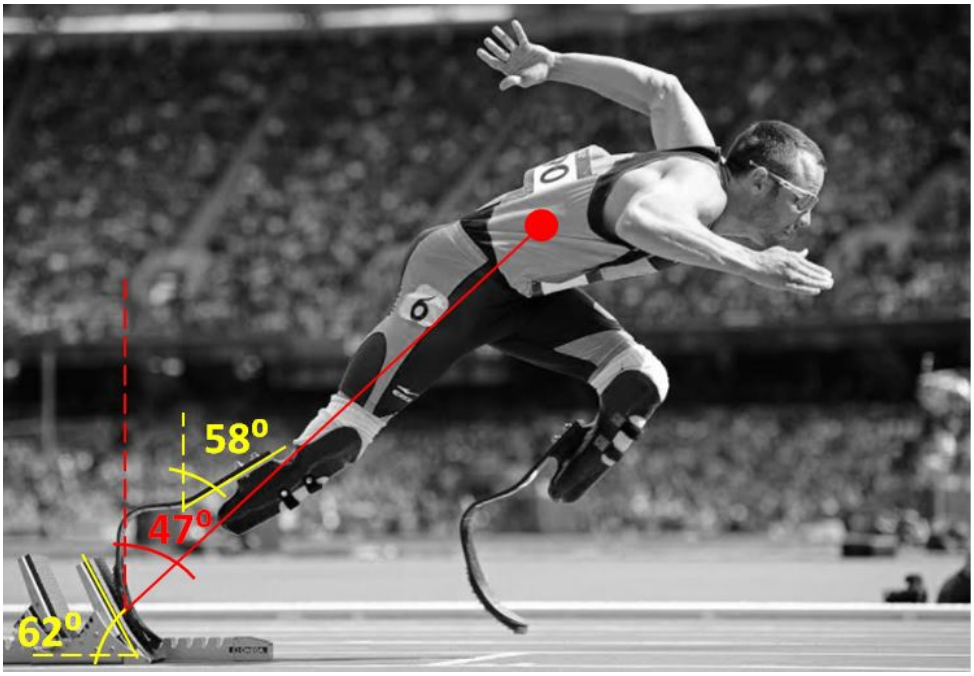

Figure B.3: Shin, drive and block angles at front block step.

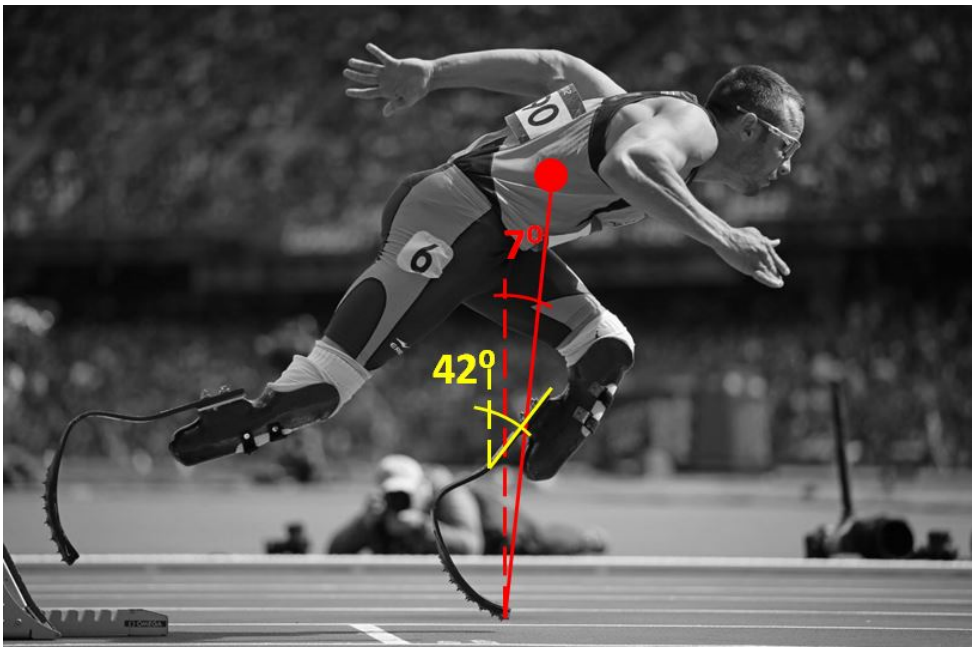

Figure B.4: Shin and drive angles at step 1.

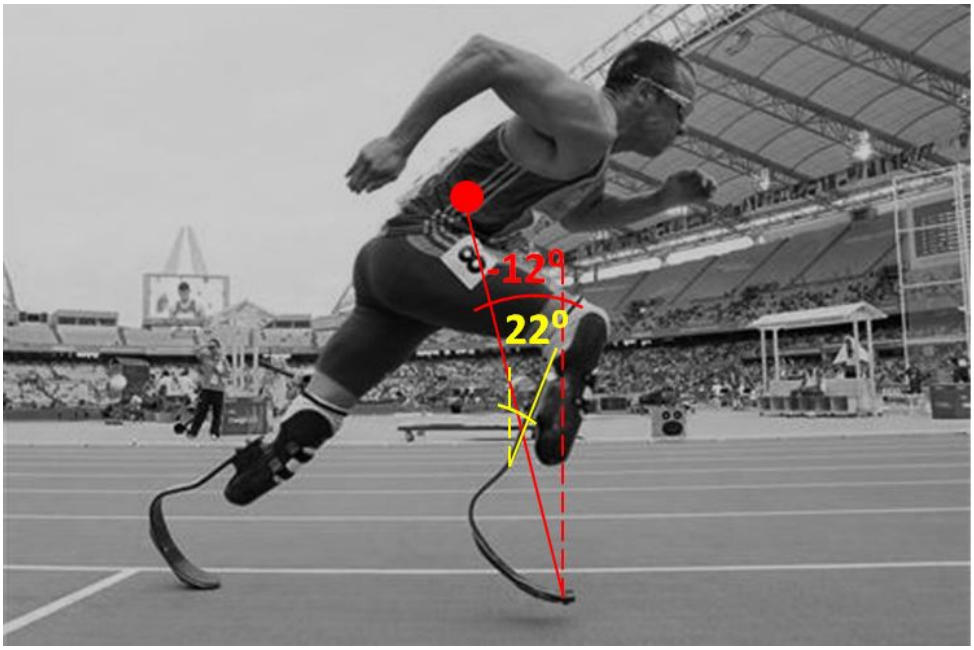

Figure B.5: Shin and drive angles at step 2.

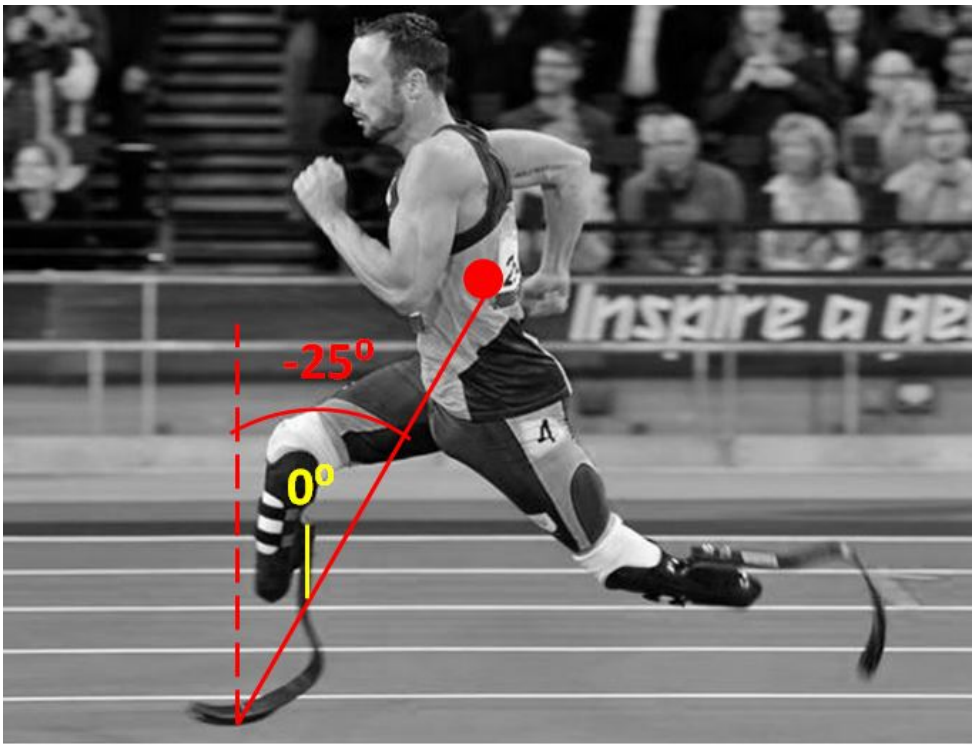

Figure B.6: Shin and drive angles at step 3.

C

MODEL TO FIND THE DEFLECTION POINT

```
1
2  clear all
3  close all
4  clc
5
6  %Variables
7  GRADIENT= 5;
8  Ftot=1; %Normalized
9  drive_start=7; % Drive angle starting position [deg]
10 shin_start=42; % Shin angle starting position[deg]
11 drive_steady=-25; % Drive angle steady position [deg]
12 shin_steady=0; % Shin angle steady position [deg]
13
14 gamma_a=-shin_start+drive_start; %[deg]
15 gamma_b=-shin_steady+drive_steady; %[deg]
16
17 % Refrence for green color
18 palegreen=[154;255;154]/255;
19
20 dh=30.4; % Horizontal distance A-B (mm)
21 dv=4.46; % Vertical distance A-B   (mm)
22 Fa_v=Ftot*cosd(gamma_a); %Force      (Newton)
23 Fa_h=Ftot*sind(gamma_a); %Force      (Newton)
24 Fb_v=Ftot*cosd(gamma_b); %Force      (Newton)
25 Fb_h=Ftot*sind(gamma_b); %Force      (Newton)
26
27 %%% Less importan settings to change
28 % extremes of the plot (in mm)
29 xstart=-50;
30 xend= 350;
31 ystart=0;
32 yend=500;
33 % max and min values for A-B distance (in mm, horizontal and vertical)
```

```
34 min_dv=0;
35 max_dv=50;
36 min_dh=0;
37 max_dh=50;
38 %% Different values dh and dv
39
40 if GRADIENT==1 %Original shape
41     dh=36.71;
42     dv=7.04;
43 end
44
45 if GRADIENT==2 %C1 long
46     dh=36.71;
47     dv=7.04;
48 end
49
50 if GRADIENT==3 %C1 medium
51     dh=25.9;
52     dv=2.98;
53 end
54
55 if GRADIENT ==4 %C1 short
56     dh=0;
57     dv=0;
58 end
59
60 if GRADIENT ==5 %C2 long
61     dh=30.4;
62     dv=4.49;
63 end
64
65 if GRADIENT ==6 %C2 medium
66     dh=18.18;
67     dv=1.19;
68 end
69
70 if GRADIENT ==7 %C2 short
71     dh=0;
72     dv=0;
73 end
74 %% function
75 m=(Fa_v-Fb_v)/(Fb_h-Fa_h);
76 q=(Fa_v*dh-Fa_h*dv)/(Fb_h-Fa_h);
77
78 fin = @(xi) m*xi+q;
79 x=linspace(-150,xend);
80
```

```
%% gradient Plot
Diff_Moment= @(dbh,dbv) (Fb_v*dbh+Fb_h*dbv)-(Fa_v*(dbh+dh) + Fa_h *(dbv
    -dv)) ;
[X,Y] = meshgrid(xstart:xend, 0:yend);

%% Sensitivity study
drive_start_dev=1.7;
shin_start_dev=2.13;
drive_steady_dev=1.86;
shin_steady_dev=2.31;

% Propagation of uncertainties
start_dev=sqrt(shin_start_dev^2+drive_start_dev^2);
steady_dev=sqrt(shin_steady_dev^2+drive_steady_dev^2);

%%
% lower line - best
Fa_v1=Ftot*cosd(gamma_a-start_dev); %Force      (Newton)
Fa_h1=Ftot*sind(gamma_a-start_dev); %Force      (Newton)
Fb_v1=Ftot*cosd(gamma_b+steady_dev); %Force      (Newton)
Fb_h1=Ftot*sind(gamma_b+steady_dev); %Force      (Newton)
m1=(Fa_v1-Fb_v1)/(Fb_h1-Fa_h1);
q1=(Fa_v1*dh-Fa_h1*dv)/(Fb_h1-Fa_h1);

fin1 = @(xi) m1*xi+q1;

% Upper line - worst
Fa_v2=Ftot*cosd(gamma_a+start_dev); %Force      (Newton)
Fa_h2=Ftot*sind(gamma_a+start_dev); %Force      (Newton)
Fb_v2=Ftot*cosd(gamma_b-steady_dev); %Force      (Newton)
Fb_h2=Ftot*sind(gamma_b-steady_dev); %Force      (Newton)
m2=(Fa_v2-Fb_v2)/(Fb_h2-Fa_h2);
q2=(Fa_v2*dh-Fa_h2*dv)/(Fb_h2-Fa_h2);

fin2 = @(xi) m2*xi+q2;


% intermediate line1
Fa_v3=Ftot*cosd(gamma_a+start_dev); %Force      (Newton)
Fa_h3=Ftot*sind(gamma_a+start_dev); %Force      (Newton)
Fb_v3=Ftot*cosd(gamma_b+steady_dev); %Force      (Newton)
Fb_h3=Ftot*sind(gamma_b+steady_dev); %Force      (Newton)
m3=(Fa_v3-Fb_v3)/(Fb_h3-Fa_h3);
q3=(Fa_v3*dh-Fa_h3*dv)/(Fb_h3-Fa_h3);

fin3 = @(xi) m3*xi+q3;

```

```
127 % intermediate line2
128 Fa_v4=Ftot*cosd(gamma_a-start_dev); %Force      (Newton)
129 Fa_h4=Ftot*sind(gamma_a-start_dev); %Force      (Newton)
130 Fb_v4=Ftot*cosd(gamma_b-steady_dev); %Force      (Newton)
131 Fb_h4=Ftot*sind(gamma_b-steady_dev); %Force      (Newton)
132 m4=(Fa_v4-Fb_v4)/(Fb_h4-Fa_h4);
133 q4=(Fa_v4*dh-Fa_h4*dv)/(Fb_h4-Fa_h4);
134
135 fin4 = @(xi) m4*xi+q4;
136
137
138 %% plot
139 f = figure;
140 ax = axes('Parent',f,'position',[0.13 0.36 0.97 0.6]); % absolute
    position plot
141
142 %POINT B
143 axM=plot(200,400,'s','MarkerFaceColor',palegreen,'MarkerEdgeColor',
    palegreen,'Markersize',5);
144
145 hold on
146 % Area of non-existence point C
147 h = area(x,fin(x),'FaceColor',[1,1,1]);
148
149
150 % Gradient map
151 if GRADIENT>=1
152     Z=Diff_Moment(X,Y);
153     Z(Z<=0)=0;
154     imagesc(X(1,:),Y(:,1),Z);
155     colormap('cool')
156     se=colorbar;
157     ylabel(se, 'Mb - Ma')
158     % Area of non-existence point C
159     h = area(x,fin(x),'FaceColor',[1,1,1]);
160
161     if GRADIENT==1
162
163         xc_o=161.69;
164         yc_o=61.15;
165
166     end
167     if GRADIENT==2
168         xc_o=161.69;
169         yc_o=61.15;
170         pointCo=plot(xc_o,yc_o,'x','MarkerFaceColor','b','
            MarkerEdgeColor','b','LineWidth',2.5,'MarkerSize',9);
```

```
171
172         xc_i = 222.54;
173         yc_i = 95.88;
174         pointC1=plot(xc_i,yc_i,'square','MarkerFaceColor','b','
                MarkerEdgeColor','b','LineWidth',2.5,'MarkerSize',5);
175     end
176     if GRADIENT==3
177         xc_i = 222.54;
178         yc_i = 95.88;
179         pointC=plot(xc_i,yc_i,'square','MarkerFaceColor','b','
                MarkerEdgeColor','b','LineWidth',2.5,'MarkerSize',5);
180     end
181     if GRADIENT ==4
182
183         xc_a = 222.54;
184         yc_a = 95.88;
185         pointC=plot(xc_a,yc_a,'square','MarkerFaceColor','b','
                MarkerEdgeColor','b','LineWidth',2.5,'MarkerSize',5);
186     end
187     if GRADIENT ==5
188         xc_a=315.57;
189         yc_a=216.87;
190
191         pointC=plot(xc_a,yc_a,'^','MarkerFaceColor','b','
                MarkerEdgeColor','b','LineWidth',2.5,'MarkerSize',5);
192     end
193     if GRADIENT ==6
194         xc_a=315.57;
195         yc_a=216.87;
196
197         pointC=plot(xc_a,yc_a,'^','MarkerFaceColor','b','
                MarkerEdgeColor','b','LineWidth',2.5,'MarkerSize',5);
198     end
199
200 end
201
202 %perturbation line 2
203 h1=plot (x,fin1(x),'g--');
204 h2=plot (x,fin2(x),'k--');%upper dotted line
205 h3=plot (x,fin3(x),'b--');
206 h4=plot (x,fin4(x),'r--');
207 y = ones(length(x));
208 y = y*315;
209 line = plot(x,y,'k-','LineWidth',2); %upper limit
210 % POINT B
211 axB=plot(0,0,'ko','Markersize',5,'MarkerFaceColor','r');
212 % POINT A
```

```
213 axA= plot(-dh,dv,'ko','Markersize',5,'MarkerFaceColor','g');
214 if GRADIENT==0
215     h1=plot (x,fin1(x),'c--'); %lower dotted line
216     h3=plot (x,fin3(x),'b--'); %lower dotted line
217     h4=plot (x,fin4(x),'r--'); %upper dotted line
218     legend([axB axA axM h2],{'Point B', 'Point A','M_{a}<M_{b}','
            perturbation line 2'},'Location', 'northeastoutside')
219 end
220 if GRADIENT==1
221
222    legend([axB axA h2],{'Point B', 'Point A','Perturbation line 2'},'
          Location', 'northeastoutside')
223     title('Region of Existence point C')
224 end
225 if GRADIENT==2
226     legend([axB axA h2 pointCo pointC1],{'Point B', 'Point A','
            perturbation line 2', 'Point C Original','Point C1'},'Location',
             'northeastoutside')
227     title('Region of Existence point C - Variation 1')
228 end
229 if GRADIENT==3
230     legend([axB axA h2 pointC],{'Point B', 'Point A','perturbation line
            2', 'Point C1'},'Location', 'northeastoutside')
231     title('Region of Existence point C - Variation 2')
232 end
233 if GRADIENT==4
234     legend([axB axA h2 pointC],{'Point B', 'Point A','perturbation line
            2', 'Point C1'},'Location', 'northeastoutside')
235     title('Region of Existence point C - Variation 3')
236 end
237 if GRADIENT==5
238     legend([axB axA h1 h2 h3 h4 pointC],{'Point B', 'Point A','1','
            perturbation line 2','3','4', 'Point C2'},'Location', '
            northeastoutside')
239     title('Region of Existence point C - New Shape 1')
240 end
241 if GRADIENT==6
242     legend([axB axA h2 pointC],{'Point B', 'Point A','perturbation line
            2', 'Point C2'},'Location', 'northeastoutside')
243     title('Region of Existence point C - New Shape 2')
244 end
245
246 set(gca,'color',palegreen)
247
248 hold off
249 set (gca,'Xdir','reverse')
250 xlim([xstart,xend]);
```

```
251 ylim([ystart,yend]);  % Extension axis
252 xlabel('d_B_H [mm]')
253 ylabel('d_B_V [mm]')
```

D

DETERMINATION OF DEVIATIONS

Due to the sensitivity of the model to changes in the drive and shin angle, some deviations in these angles were introduced.

Considering that the drive angle is defined by the position of the CoM, the value of the deviation of the drive angle was chosen so that the horizontal displacement of the CoM at each of the steps was inside a range of 6 cm, i.e. ±3cm with respect to the reference position. Similarly, assuming a perfect alignment (0 degrees) between the prosthesis and the shank, the shin angle is determined by the position and flexion of the knee. Thus, the value of the deviation of the shin angle was chosen so that the horizontal displacement of the CoM at each of the steps was inside a range of 4 cm, i.e. ±2cm with respect to the reference position. Thus, the following model could be used to calculate both deviations for the step 1 and step 3.

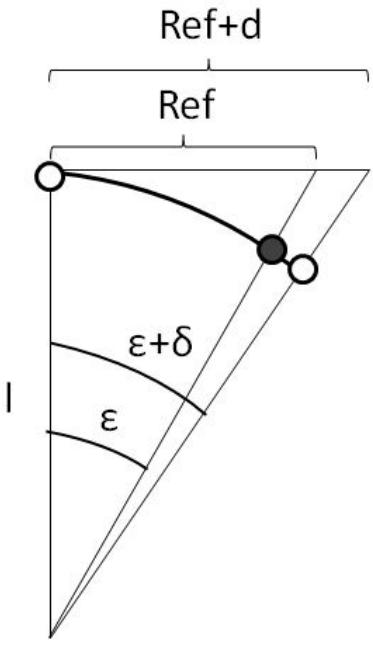

Figure D.1: Representation of the deviations, δ, of the shin and drive angles, here represented as ϵ. The black dot represents either the CoM or the knee of the athlete. The trajectory of the dot is also shown.

From Figure D.1 the following expressions are deduced:

$$Ref = l\,tan(\epsilon) \tag{D.1}$$

$$Ref + d = l\,tan(\epsilon + \delta) \tag{D.2}$$

$$(\epsilon + \delta) = atan\frac{Ref + d}{l} \tag{D.3}$$

From here, knowing the height of the CoM [29] and of the knee [30], the deviations for the step 1 and steady step shin and drive angles were calculated. The results are shown below.

$$\delta\phi_A = \pm 1.7^\circ \tag{D.4}$$

$$\delta\phi_B = \pm 1.86^\circ \tag{D.5}$$

$$\delta\beta_A = \pm 2.13^\circ \tag{D.6}$$

$$\delta\beta_B = \pm 2.31^\circ \tag{D.7}$$

The deviations of ϕ and β are assumed to be uncorrelated and can therefore be propagated to retrieve the uncertainty of γ with the following rule: given that γ is a combination of sums and differences, the uncertainties add in quadrature, as seen below.

$$\delta\gamma = \sqrt{(\delta\phi)^2 + (\delta\beta)^2} \tag{D.8}$$

Thus, the deviations for the direction of the force are obtained as follows:

$$\delta\gamma_1 = \sqrt{(\delta\phi_1)^2 + (\delta\beta_1)^2} = \pm 2.72^\circ \tag{D.9}$$

$$\delta\gamma_3 = \sqrt{(\delta\phi_3)^2 + (\delta\beta_3)^2} = \pm 2.97^\circ \tag{D.10}$$

E

Laminate Design Rules and Play-Drop Design Guidelines

1. Stacking sequences should be symmetric about the mid-plane.
2. Whenever possible, stacking sequences should be balanced, with the same number of $+\theta$ and $-\theta$ degrees plies.
3. At least 3 different ply orientations should be used.
4. 10% rule: it is required that each laminate contains at least 10% of each orientation used.
5. The difference between orientations of two consecutive plies should not exceed 45 degrees.
6. No 0 degree ply should be placed on the lower and upper surfaces of the laminate.
7. Covering plies on the lower and upper surfaces of the laminate should not be dropped.
8. No more than 2 plies should be stopped at the same increment of thickness.
9. A continuous ply should be kept every 3 consecutive dropped plies (not fulfilled on the design). 10. Maximum taper slope: the minimal stagger distance (the length of the increment of thickness) is about 8 times the thickness of the dropped plies.

F

FEM Model

F.1. Creating the Model

The FEM (Finite Element Modelling) program used to recreate an original prosthesis is Abaqus/Standard from Dassault Systemes. The purpose of this model is to measure the 1D stiffness at each of the aforementioned steps to better understand the behavior of current running prostheses. For this, the following steps were taken in Abaqus: first, a part with the contour of the prosthesis was created; second, the material and its mechanical properties were chosen; third, the composite lamination was created; fourth, the part was meshed; and fifth, the boundary conditions were imposed.

F.1.1. Creating the Part

A 3D deformable shell part was created, by extruding the 2D shape of the contour of the prosthesis. The model created was based on the blade 1E90 from Ottobock. Both shapes (the 1E90 and the created model) can be seen in Figure F.1 below.

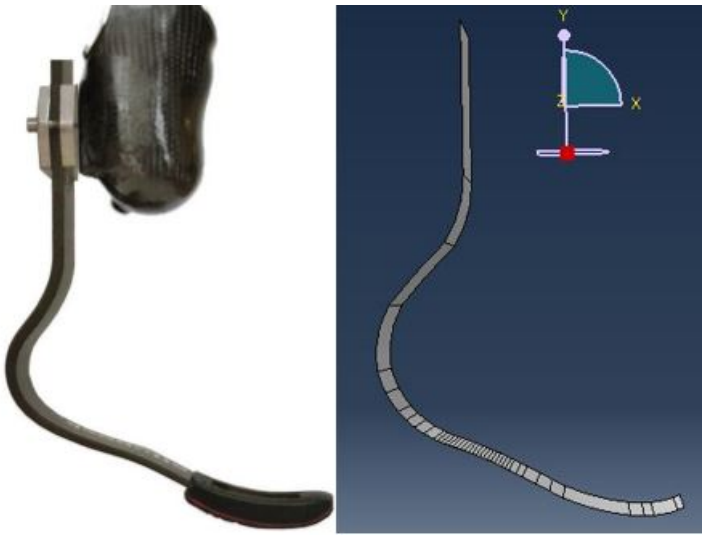

Figure F.1: On the right: prosthesis 1E90 from Ottobock. On the left: created shell element imitating Ottobock's 1E90.

The dimensions of the 1E90 were not known. Since the Paralympic committee imposes the rule that RPs cannot be longer than what the biological leg would be [4], the dimensions of the model were directly copied from the Cheetah foot by Ossur, which were known [21].

F.1.2. CREATING THE LAMINATION

In order to create ply drops on the Abaqus model, several partitions were created on the shell, and a different lamination was assigned to each area. This is explained by Figure F.2. The same lamination with the dropped plies as in Figure 2.7 is shown, but now also the partitions are depicted. These partitions allow to divide the whole laminate in different sections. In this way, a different lamination can be assigned to each section.

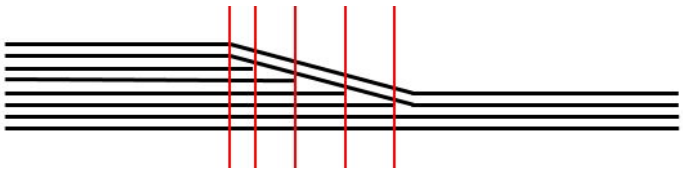

Figure F.2: Illustration of the partitions created in the Abaqus shell to simulate dropping plies. Creating 5 partitions divides the laminate in 6 different sections, what allows to choose a different lamination for each of the sections in Abaqus. The first section starting from the left is assigned 8 plies; the second section, 7 plies; the third section, 6 plies; and so on. This is how the ply drops were mimicked in Abaqus.

The multiple partitions created along the full length of the prosthesis can be seen in Figure F.3. The lines in the shell correspond to the partitions of the model. Some of these partitions were automatically generated by Abaqus, as a result of extruding a noncontinuous sketch; other partitions were manually created to gradually drop plies along the prosthesis. The latter ones are located in the area with the highest density of partitions, making this area the main (?) deflection area of the whole prosthesis.

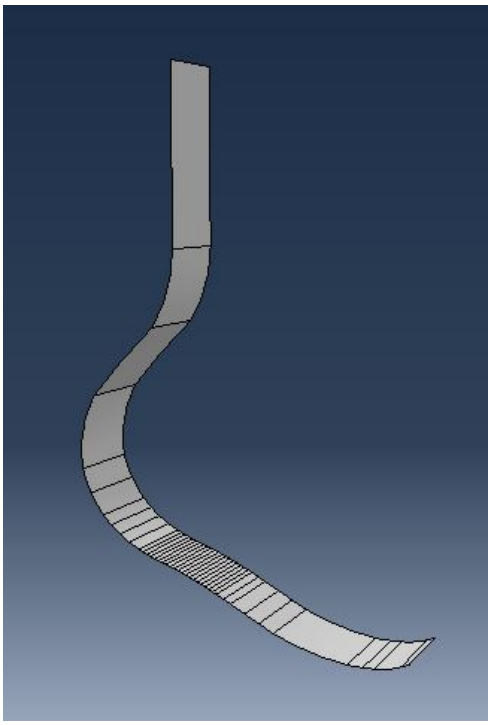

Figure F.3: Shell of the Abaqus model of an original prosthesis with the multiple partitions, both the automatically and the manually generated. The plies were dropped only in the area with the highest density of partitions, making this area the deflection point of the whole prosthesis.

Based on trial an error, the lamination was tuned until a bending stiffness under the conditions of the static compression tests of 17.1N/mm was achieved. This final lamination is a symmetric, balanced lamination, with plies in 3 different directions (0, +45, and -45 degrees). As previously mentioned, this lamination explained in detail in Appendix J.

F.1.3. MESHING THE PART

The available element types to mesh a shell are three: quadrilateral (S4), quadrilateral with reduced integration (S4R) and triangular (A3). Triangular elements provide the mesh with more nodes than quadrilateral elements, what increases the accuracy of the results but requires more computation time. Table F.1 shows the results of the bending stiffness simulated under static compression test conditions of the model mimicking an original prosthesis.

Element type	Bending stiffness [N/mm]	%
A3	38.39	0
S4	38.17	0.57
S4R	38.03	0.95

Table F.1: Mesh element type analysis.

Since the difference in bending stiffness was less than 1%, it was decided to use S4R shell elements to reduce computation times.

The size of the mesh also determines the accuracy of the results. To find a balance between results accuracy and computing resources, a convergence analysis was carried out.

The results are shown in Table F.2 below.

Global element size	Total number of elements	Bending stiffness [N/mm]
30	98	16.5
20	220	17.11
15	325	17.1089
10	664	17.1077
8	873	17.1065

Table F.2: Mesh size convergence analysis.

Based on these results, the chosen mesh attributes are shown in Table F.3.

Type of element	S4R
Total number of elements	325
Global size element	15

Table F.3: Mesh attributes of the RP models.

F.1.4. SETTING THE BOUNDARY CONDITIONS

For the simulations, the upper shank was encastred ($\Delta x = \Delta y = \Delta z = 0$), mimicking the attachment to the stump. The force was applied on the corresponding contact point for each of the steps analysed. The magnitude of the forces at each step are shown below, in Table F.4 [9].

Block steps	**Start steps**	**Steady steps**
1.5xBW	3xBW	3.5xBW

Table F.4: GRFs measured at the block steps, start steps and steady steps [7].

The force and boundary conditions set can be observed in Figure F.4.

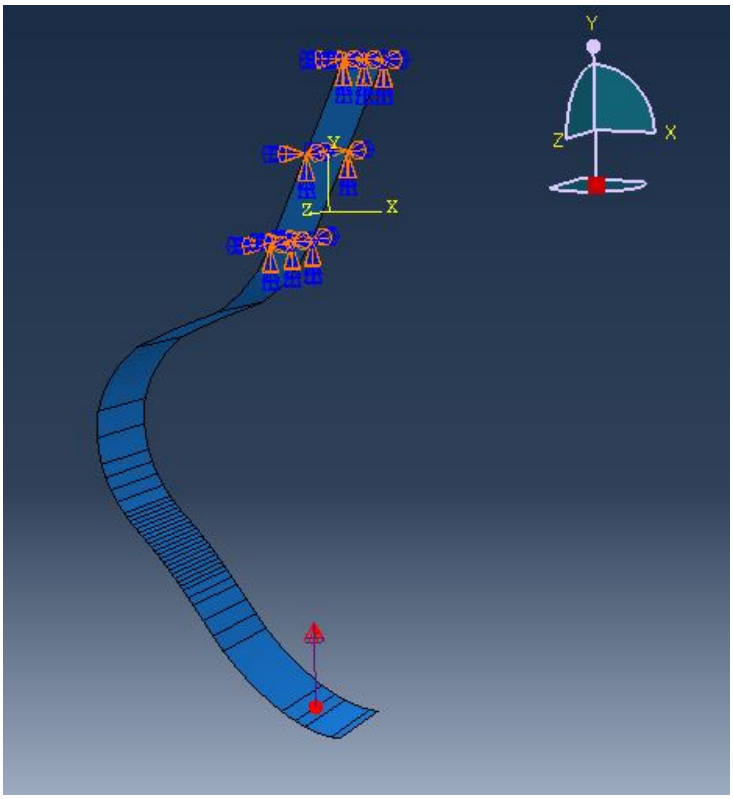

Figure F.4: Boundary conditions of the Abaqus model of an original prosthesis: vertical force applied on the contact point and encastred stump. The reason for the rotation of the prosthesis and the vertical force is explained in the following section.

G

DRAWINGS

The drawings of the original prosthesis, the new shape and the mold are shown in this appendix.

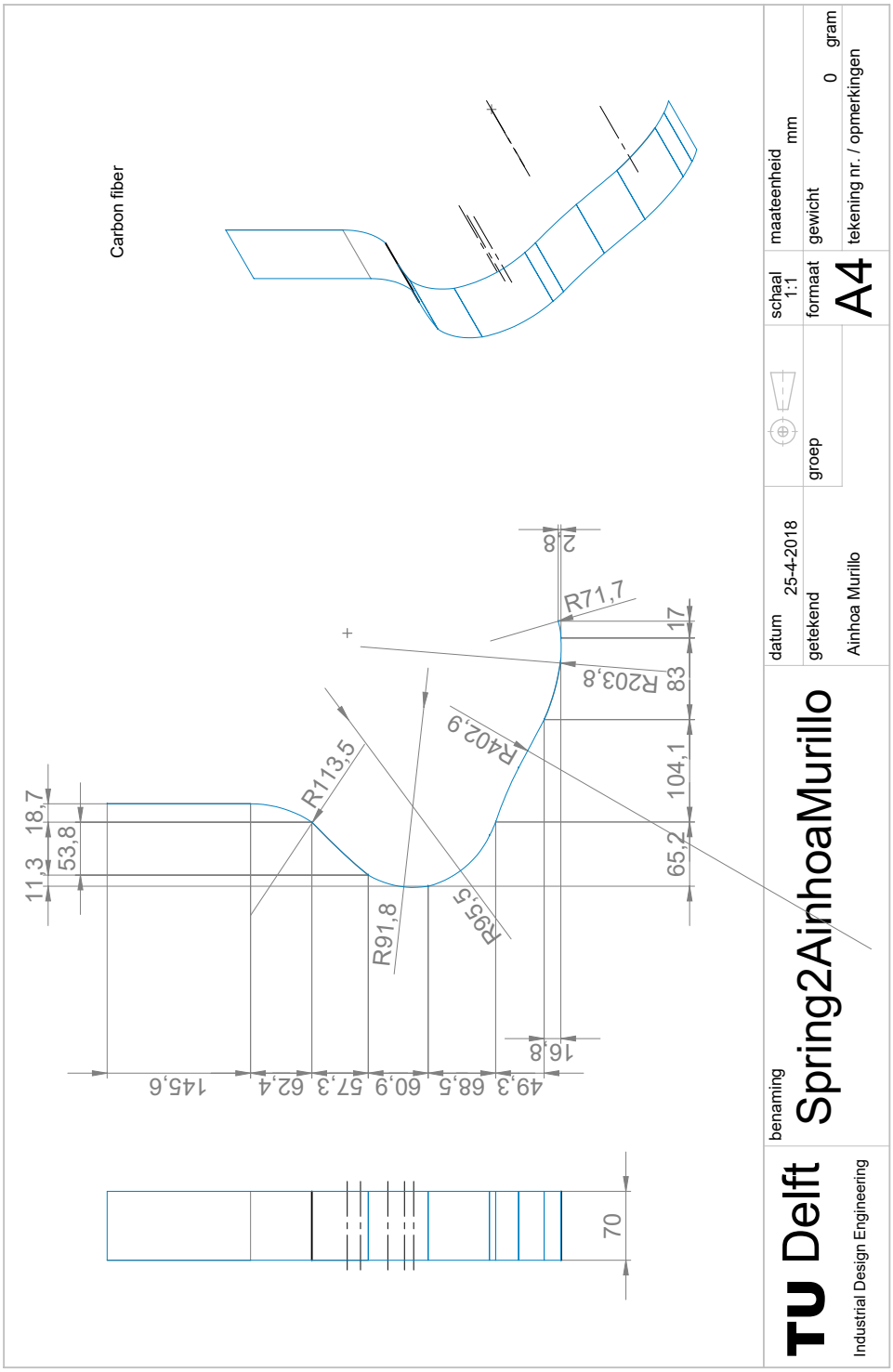
Carbon fiber
11,3
18,7
53,8
R113,5
R91,8
R95,5
R402,9
R203,8
R71,7
2,8
16,8
17
83
104,1
65,2
49,3
68,5
60,9
57,3
62,4
145,6
70
TU Delft
Industrial Design Engineering
benaming
Spring2AinhoaMurillo
datum 25-4-2018
getekend
Ainhoa Murillo
groep
schaal 1:1
formaat A4
maateenheid mm
gewicht 0 gram
tekening nr. / opmerkingen
SOLIDWORKS Educational Product. For Instructional Use Only.

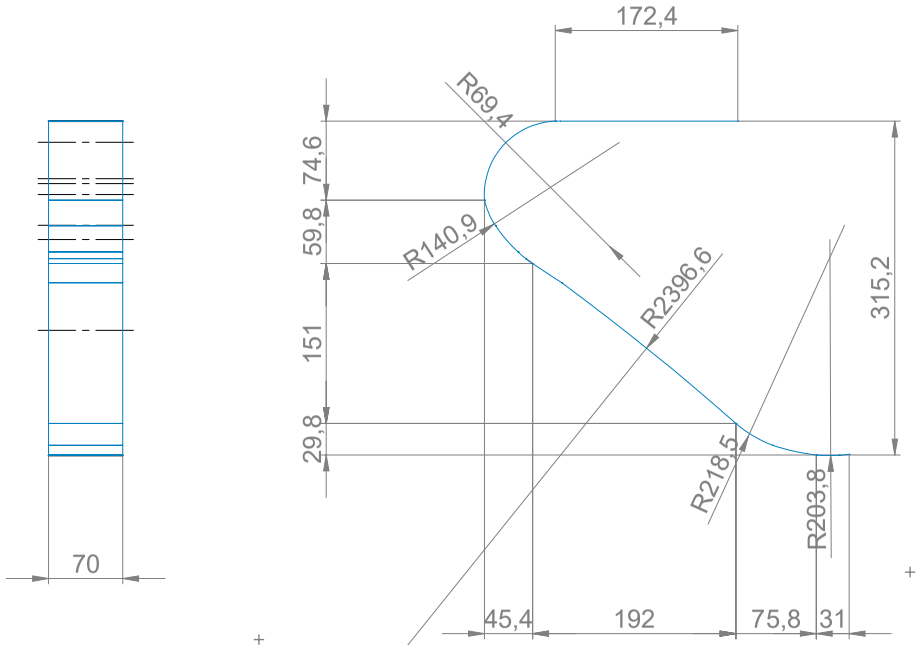

Mat.: Material <not specified>
Aantal: << >>

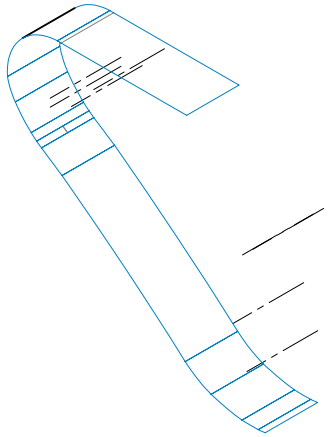

TU Delft Industrial Design Engineering	benaming C3Spring	datum 28-5-2018	schaal 1:1	maateenheid mm
		getekend <<(achter)namen & studienummers>>	groep <<dagdeel>>	formaat A4	gewicht 0 gram
				tekening nr. / opmerkingen <<tekeningnummer>>

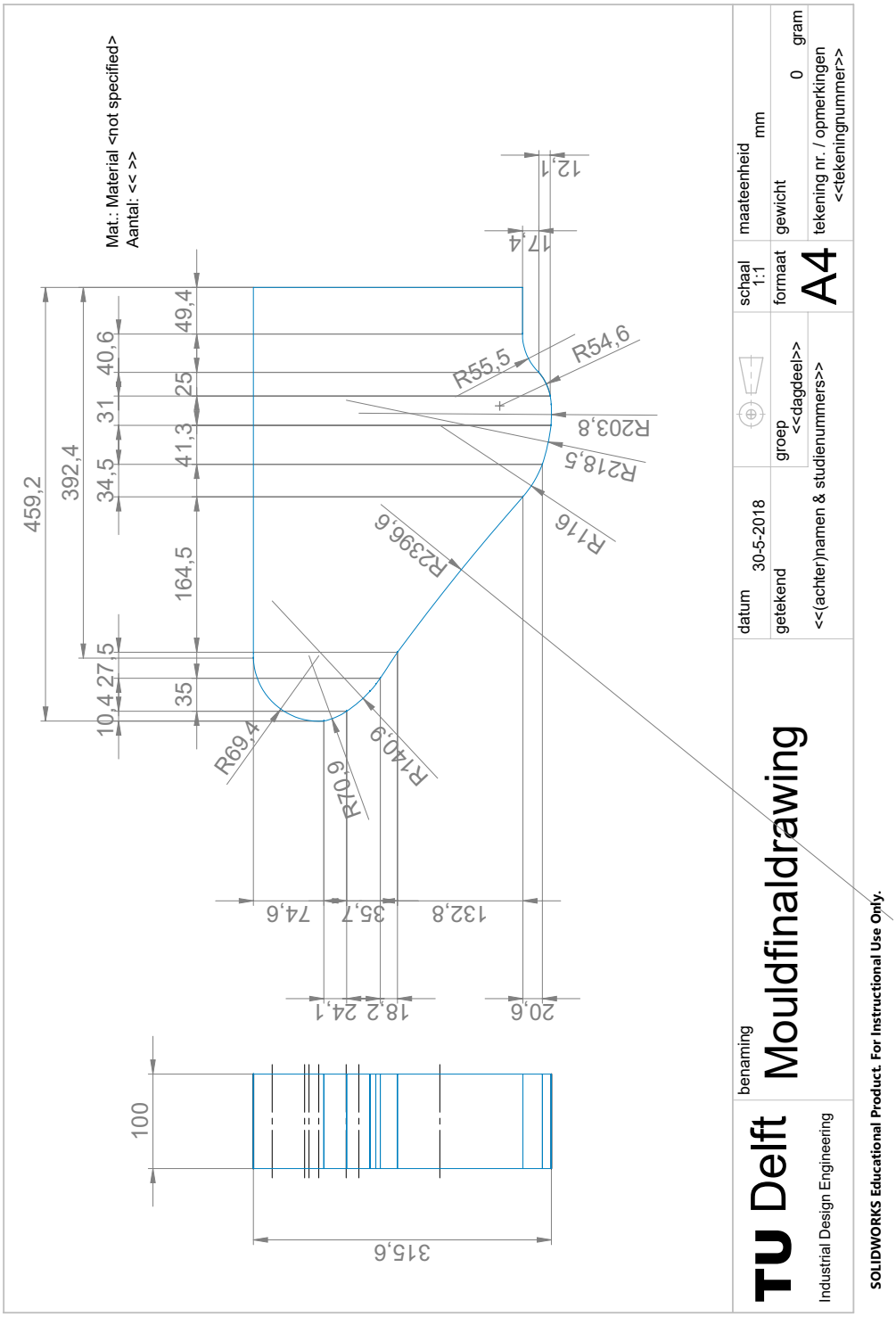
Mat.: Material <not specified>
Aantal: << >>
459,2
392,4
10,4
27,5
34,5
40,6
31
49,4
25
41,3
35
164,5
12,1
17,4
R55,5
R54,6
R203,8
R218,5
R116
R239,6
R69,4
R70,9
R140,9
74,6
35,7
132,8
18,2
24,1
20,6
100
315,6
TU Delft
Industrial Design Engineering
benaming
Mouldfinaldrawing
datum 30-5-2018
getekend
<<(achter)namen & studienummers>>
groep <<dagdeel>>
schaal 1:1
formaat A4
maateenheid mm
gewicht 0 gram
tekening nr. / opmerkingen
<<tekeningnummer>>
SOLIDWORKS Educational Product. For Instructional Use Only.

H

MOMENTS AROUND DEFLECTION POINT

Due to the linearity of the perceived stiffness, the force magnitude was not considered for the calculation of the moments around the deflection point. Knowing the direction of the force at step 1 and step 3, as well as the horizontal and vertical distances between the deflection point and the contact points, the moment created at each step was calculated as follows:

$$M_A = F_{AV} d_{AH} + F_{AH} d_{AV} \tag{H.1}$$

$$M_B = F_{BV} d_{BH} + F_{BH} d_{BV} \tag{H.2}$$

Where:

$$F_{AV} = cos(\gamma_A) \tag{H.3}$$

$$F_{AH} = sin(\gamma_A) \tag{H.4}$$

$$F_{BV} = cos(\gamma_B) \tag{H.5}$$

$$F_{BH} = sin(\gamma_B) \tag{H.6}$$

The shank of the prosthesis was aligned with the y axis of the global reference frame, i.e. the shin angle, β, was made zero (as observed in Figure 3.6). Thus, the angles γ are defined as follows:

$$\gamma_1 = \phi_1 - \beta_1 = -35^\circ \tag{H.7}$$

$$\gamma_3 = \phi_3 - \beta_3 = -25^\circ \tag{H.8}$$

Where β is the shin angle, and ϕ is the drive angle.

These expressions lead to the following results:

$$M_1 = 131.48 Nmm \tag{H.9}$$

$$M_3 = 120.7 Nmm \tag{H.10}$$

I

BUCKLING AND FAILURE ANALYSIS OF NEW PROSTHESIS

The absence of buckling and failure in the structure under the maximum force applied (3,5xBW) had to be ensured.

To analyze the existence of buckling in the new shape, 3 different points in the deflected part of the prosthesis were chosen, which are shown in Figure I.1 below.

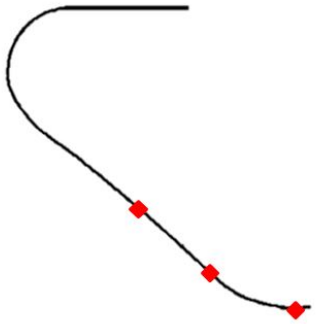

Figure I.1: Points in the deflected area of the new prosthesis chosen for buckling analysis. 3 points can be distinguished, starting from left: high point, middle point and low point.

A constant displacement of these points or a convergence of the variation of the displacement given at each consecutive force step would ensure the absence of buckling. For this, the applied force was divided in 7 steps through which the force was applied. Step 1 and step 3 were analysed.

Figures I.2 and I.3 show the linear relation between displacement and force for step 1 and steady step.

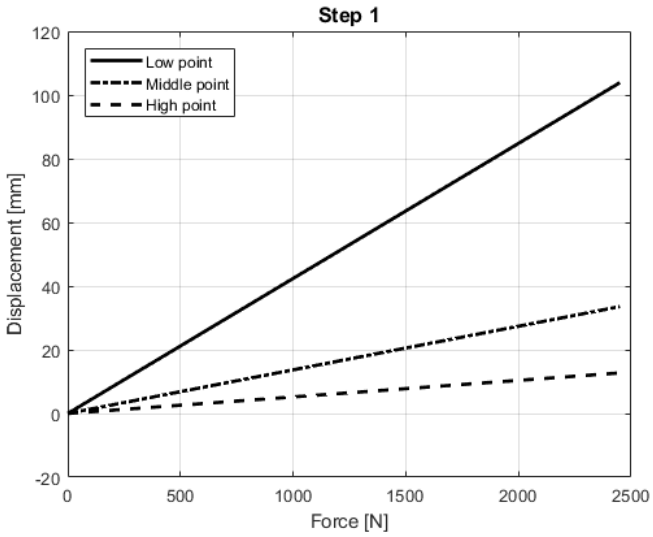

Figure I.2: Linear displacement-force relation of each point (high, medium and low) under an increasing force applied at the step 1 contact point.

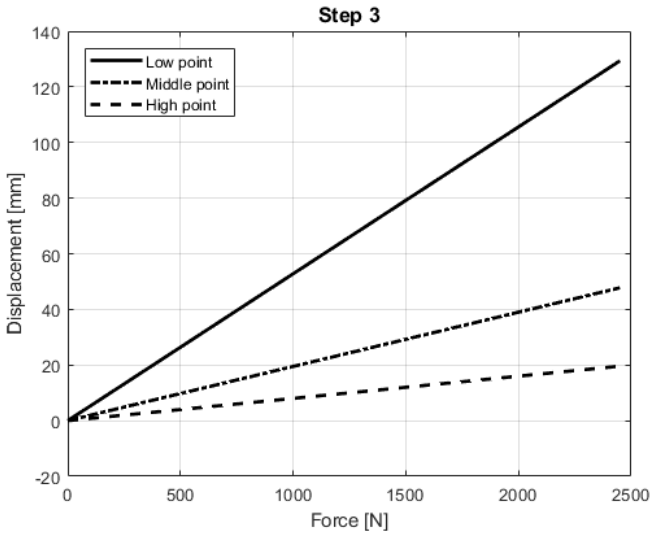

Figure I.3: Linear displacement-force relation of each point (high, medium and low) under an increasing force applied at the step 3 contact point.

Therefore, if the variation in the displacement from one force step to the next one is plotted (see Figures I.4 and I.5), it can be observed that no buckling is present in this design under a force of 3.5xBW, since the variation in displacement immediately converges.

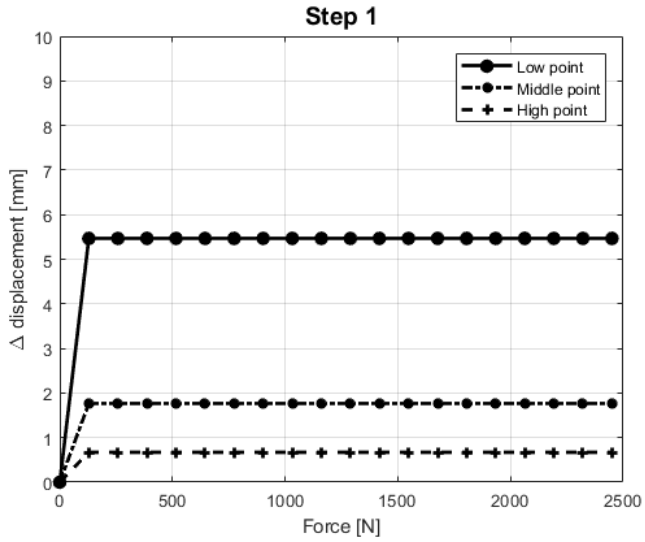

Figure I.4: Displacement variation of each point (high, medium and low) for an increasing force at the step 1 contact point.

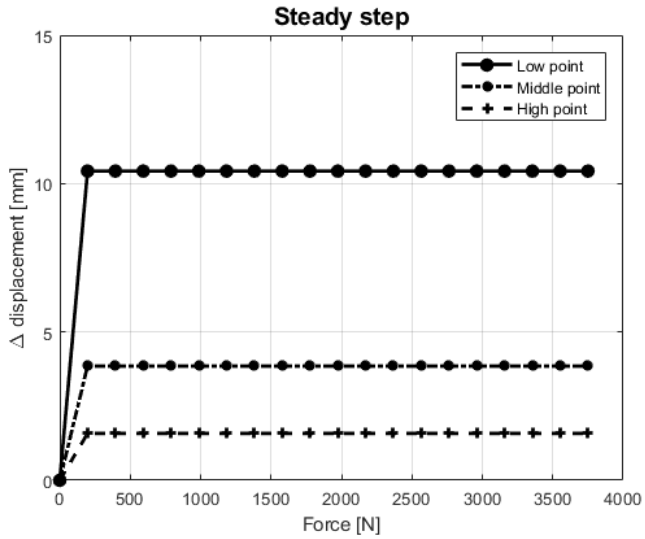

Figure I.5: Displacement variation of each point (high, medium and low) for an increasing force at the steady step contact point.

For the failure analysis, the Tsai Hill criterion was used. Figure **??** shows the Abaqus results of the simulations. It can be observed that failure index in the laminate does not reach 1, what ensures that no laminate failure is present under the maximum load.

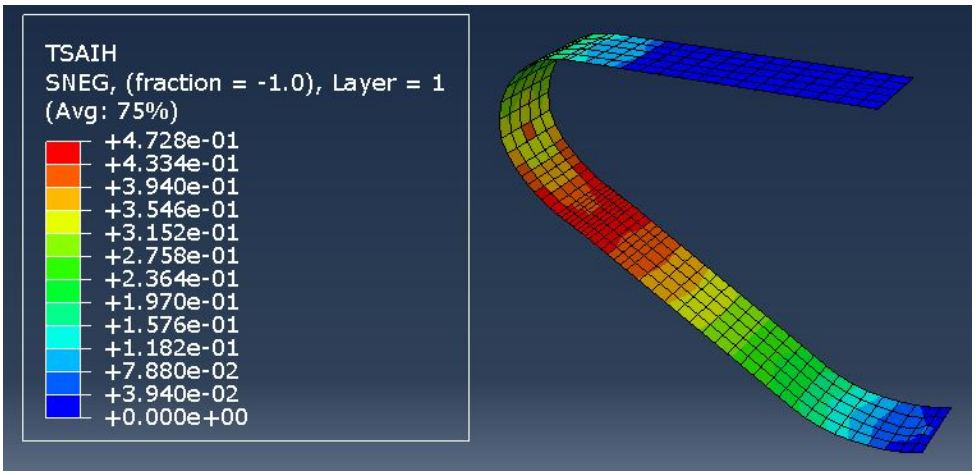

Figure I.6: Displacement variation of each point (high, medium and low) for an increasing force at the steady step contact point.

The material properties used for the failure analysis are shown in Table I.1 below.

Tensile Stress Fiber Direction	1000 MPa
Compression Stress Fiber Direction	1000 MPa
Tensile Stress Transversal Direction	28 MPa
Compression Stress Transversal Direction	138 MPa

Table I.1: Carbon fiber failure properties [31].

J

Carbon Fibre Lamination

The lamination of the model of the original prosthesis is shown in Figure J.1. The table shows each ply of the laminate in order, from inner to outer surface. The column *'Direction (deg)'* defines the direction of each ply. It can be observed that 3 different directions were used (0, +45, and -45) in order to fulfill the 10% rule. No 0 degrees plies were placed at the outer or inner surfaces, and 0 degrees plies were put in between +45 and -45 to avoid a difference bigger than 45 degrees between orientations of two consecutive plies. The advised symmetric and balanced lamination is also observed. The column *'Length (mm)'* defines the total length of each ply. The total length of the 1E90 model is 682mm. But tt can be noticed that not all the plies have the full length of 682mm. This happens because some of the plies are dropped, i.e. don't go from top to bottom of the prosthesis, in order to define the deformation point. The column *'Width (mm)'* defines the total width of each ply, which is the same for all. The column *'Layers'* tells the amount of plies with all the previous characteristics that are stacked together in the lamination. The column *'Thickness (mm)'* defines the thickness of each ply. Finally, the column *'Area (mm2)'* shows the total area of each ply.

All the lamination rules in Appendix E were fulfilled but number 9 (a continuous ply should be kept every 3 consecutive dropped plies). All the dropped layers were put in the middle to avoid delamination, just like the prosthetic company Ottobock does it.

Similarly, the laminations of the modelled AG11 and the built prototype of the AG11 are shown in Figures J.2 and J.3 respectively.

Prosthesis	Direction (°)	Length (mm)	Width (mm)	Layers	Thickness (mm)	Area (mm2)
Model 1E90	45	682	70	1	0,16	47740
	0	682	70	1	0,16	47740
	-45	682	70	1	0,16	47740
	0	682	70	1	0,16	47740
	45	682	70	1	0,16	47740
	0	682	70	1	0,16	47740
	-45	682	70	1	0,16	47740
	0	682	70	1	0,16	47740
	45	682	70	1	0,16	47740
	0	682	70	1	0,16	47740
	-45	682	70	1	0,16	47740
	0	682	70	4	0,16	190960
	0	461,5	70	1	0,16	32305
	0	456,5	70	1	0,16	31955
	0	451,5	70	1	0,16	31605
	0	446,5	70	1	0,16	31255
	0	441,5	70	1	0,16	30905
	0	436,5	70	1	0,16	30555
	0	431,5	70	1	0,16	30205
	0	426,5	70	1	0,16	29855
	0	421,5	70	1	0,16	29505
	0	416,5	70	1	0,16	29155
	0	411,5	70	1	0,16	28805
	0	406,5	70	1	0,16	28455
	0	401,5	70	1	0,16	28105
	0	396,5	70	1	0,16	27755
	0	391,5	70	1	0,16	27405
	0	386,5	70	1	0,16	27055
	0	381,5	70	1	0,16	26705
	0	376,5	70	1	0,16	26355
	0	371,5	70	1	0,16	26005
	0	366,5	70	1	0,16	25655
	0	361,5	70	1	0,16	25305
	0	356,5	70	1	0,16	24955
	0	376,5	70	1	0,16	26355
	0	371,5	70	1	0,16	26005
	0	366,5	70	1	0,16	25655
	0	361,5	70	1	0,16	25305
	0	356,5	70	1	0,16	24955
	0	682	70	4	0,16	190960
	-45	682	70	1	0,16	47740
	0	682	70	1	0,16	47740
	45	682	70	1	0,16	47740
	0	682	70	1	0,16	47740
	-45	682	70	1	0,16	47740
	0	682	70	1	0,16	47740
	45	682	70	1	0,16	47740
	0	682	70	1	0,16	47740
	-45	682	70	1	0,16	47740
	0	682	70	1	0,16	47740
	45	682	70	1	0,16	47740
				57	**9,12**	**2190335**

Figure J.1: Lamination of model of the 1E90.

Prosthesis	Direction (°)	Length (mm)	Width (mm)	Amount	Thickness (mm)	Area (mm2)
AG11	45	724	70	1	0,16	50680
	0	724	70	1	0,16	50680
	-45	724	70	1	0,16	50680
	0	724	70	1	0,16	50680
	45	724	70	1	0,16	50680
	0	724	70	1	0,16	50680
	-45	724	70	1	0,16	50680
	0	724	70	1	0,16	50680
	45	724	70	1	0,16	50680
	0	724	70	1	0,16	50680
	-45	724	70	1	0,16	50680
	0	724	70	1	0,16	50680
	45	724	70	1	0,16	50680
	0	724	70	1	0,16	50680
	-45	724	70	1	0,16	50680
	0	724	70	11	0,16	557480
	0	366	70	1	0,16	25620
	0	361	70	1	0,16	25270
	0	356	70	1	0,16	24920
	0	351	70	1	0,16	24570
	0	346	70	1	0,16	24220
	0	341	70	1	0,16	23870
	0	336	70	1	0,16	23520
	0	331	70	1	0,16	23170
	0	326	70	1	0,16	22820
	0	321	70	1	0,16	22470
	0	316	70	1	0,16	22120
	0	311	70	1	0,16	21770
	0	724	70	10	0,16	506800
	-45	724	70	1	0,16	50680
	0	724	70	1	0,16	50680
	45	724	70	1	0,16	50680
	0	724	70	1	0,16	50680
	-45	724	70	1	0,16	50680
	0	724	70	1	0,16	50680
	45	724	70	1	0,16	50680
	0	724	70	1	0,16	50680
	-45	724	70	1	0,16	50680
	0	724	70	1	0,16	50680
	45	724	70	1	0,16	50680
	0	724	70	1	0,16	50680
	-45	724	70	1	0,16	50680
	0	724	70	1	0,16	50680
	45	724	70	1	0,16	50680
				63	**10,08**	**2869020**

Figure J.2: Lamination of model of the AG11.

Prosthesis	Material	Direction (°)	Length (mm)	Width (mm)	Amount	Thickness (mm)
AG11	Fabric	45	724	70	1	0,26
	Fabric	45	724	70	1	0,26
	Fabric	45	724	70	1	0,26
	Fabric	45	724	70	1	0,26
	UD	0	724	70	10	0,26
	UD	0	366	70	1	0,26
	UD	0	361	70	1	0,26
	UD	0	356	70	1	0,26
	UD	0	351	70	1	0,26
	UD	0	346	70	1	0,26
	UD	0	341	70	1	0,26
	UD	0	336	70	1	0,26
	UD	0	331	70	1	0,26
	UD	0	326	70	1	0,26
	UD	0	321	70	1	0,26
	UD	0	316	70	1	0,26
	UD	0	311	70	1	0,26
	UD	0	724	70	9	0,26
	Fabric	45	724	70	1	0,26
	Fabric	45	724	70	1	0,26
	Fabric	45	724	70	1	0,26
	Fabric	45	724	70	1	0,26
					39	10,14

Figure J.3: Lamination of the prototype of the AG11.

K

RAW DATA

The raw data obtained from the DIC and test bench are shown in this appendix.

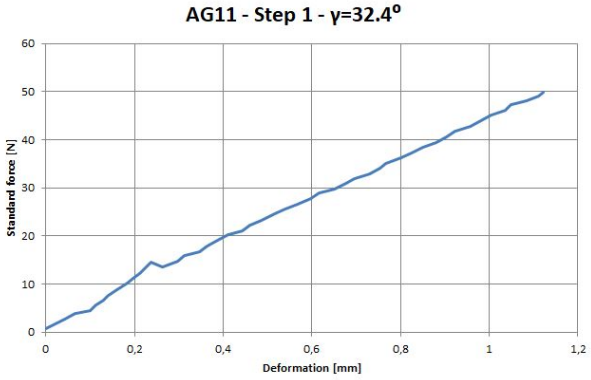

Figure K.1: AG11 - Step 1 - $\gamma = 32.4 deg$. Test bench vertical stiffness plot.

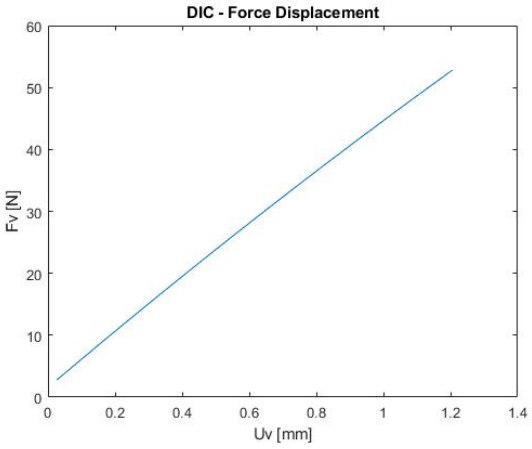

Figure K.2: AG11 - Step 1 - $\gamma = 32.4 deg$. DIC stiffness vertical plot.

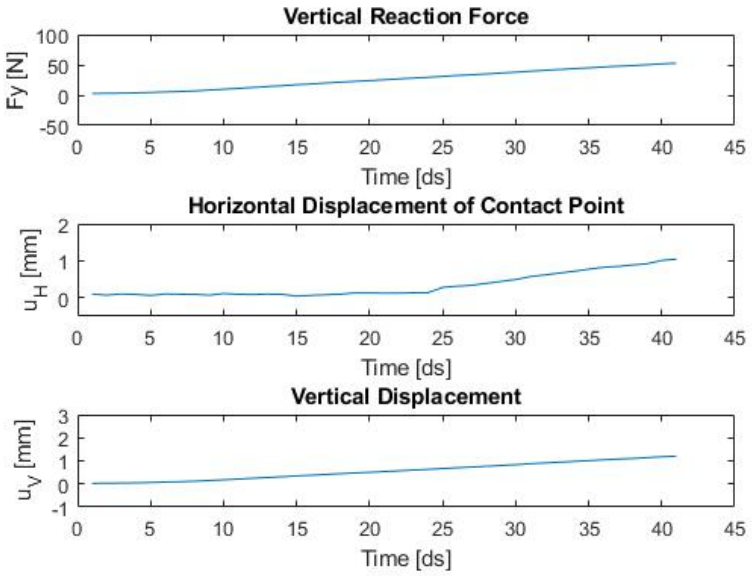

Figure K.3: AG11 - Step 1 - $\gamma = 32.4deg$. DIC vertical force, horizontal displacement and vertical displacement.

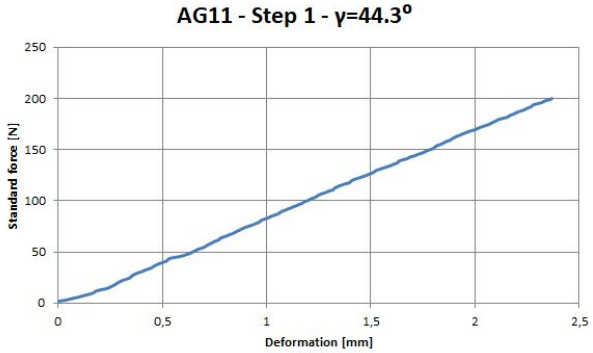

Figure K.4: AG11 - Step 1 - $\gamma = 44.3deg$. Test bench vertical stiffness plot.

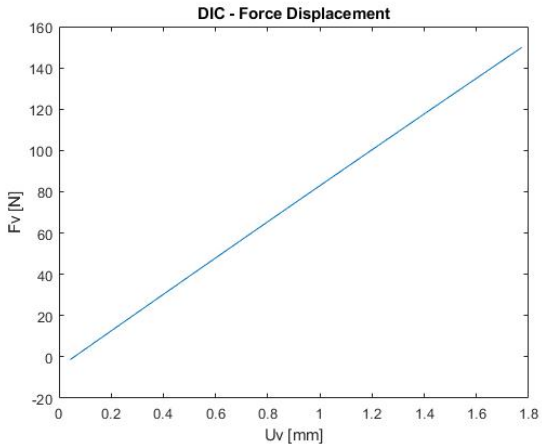

Figure K.5: AG11 - Step 1 - $\gamma = 44.3deg$. DIC stiffness vertical plot.

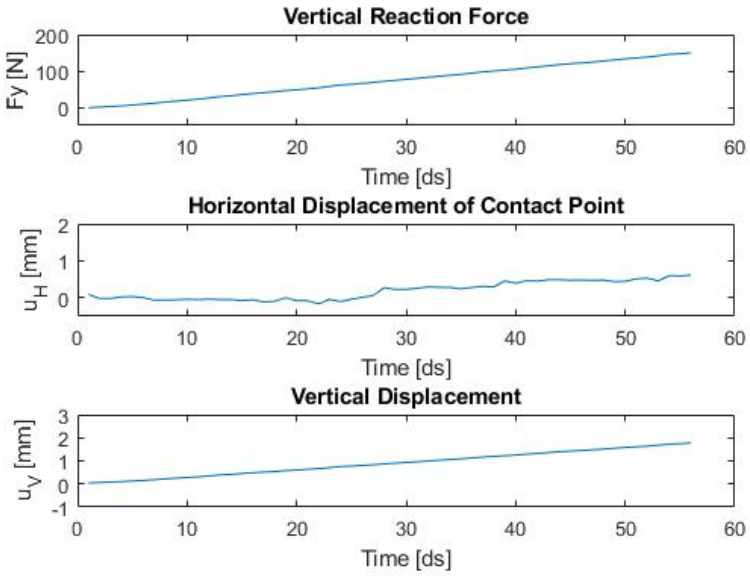

Figure K.6: AG11 - Step 1 - $\gamma = 44.3deg$. DIC vertical force, horizontal displacement and vertical displacement.

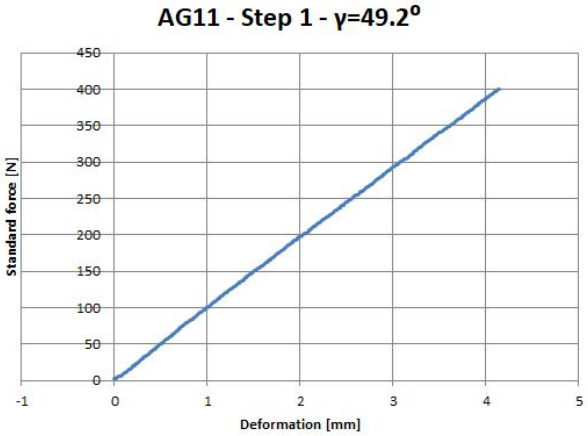

Figure K.7: AG11 - Step 1 - $\gamma = 49.2deg$. Test bench vertical stiffness plot.

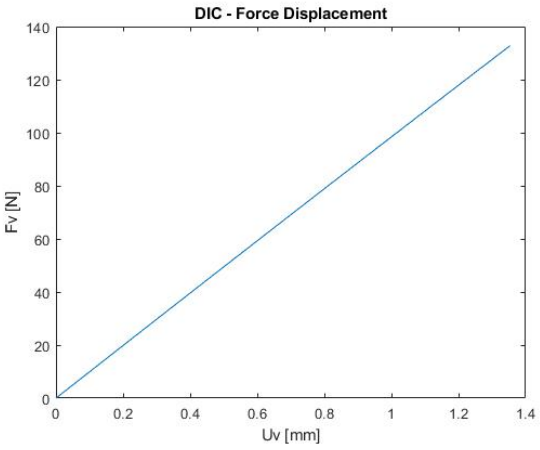

Figure K.8: AG11 - Step 1 - $\gamma = 49.2deg$. DIC stiffness vertical plot.

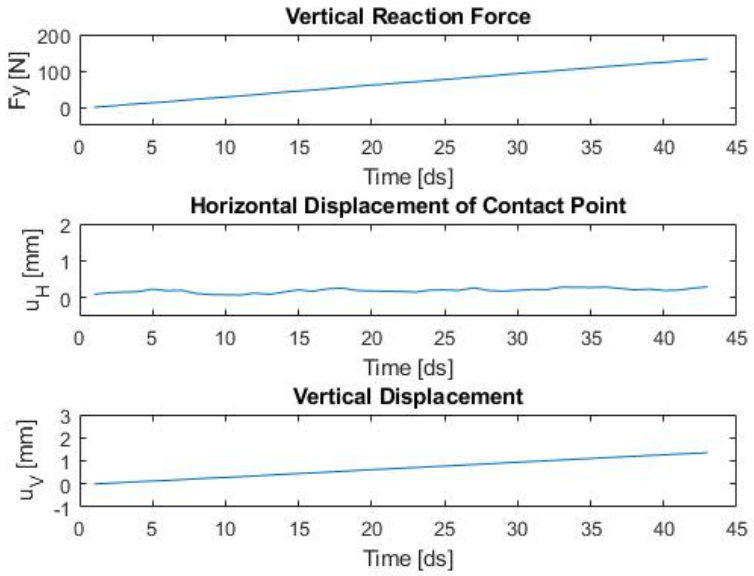

Figure K.9: AG11 - Step 1 - $\gamma = 49.2 deg$. DIC vertical force, horizontal displacement and vertical displacement.

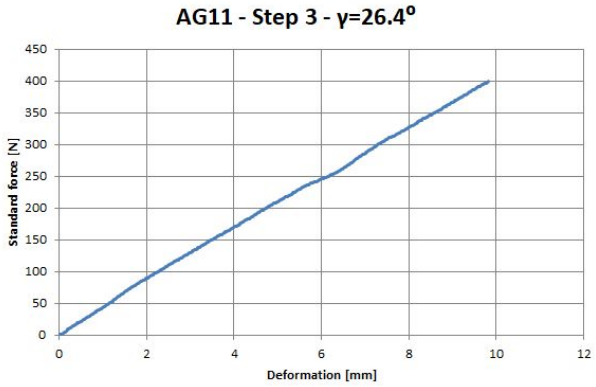

Figure K.10: AG11 - Step 3 - $\gamma = 26.6$. Test bench vertical stiffness plot.

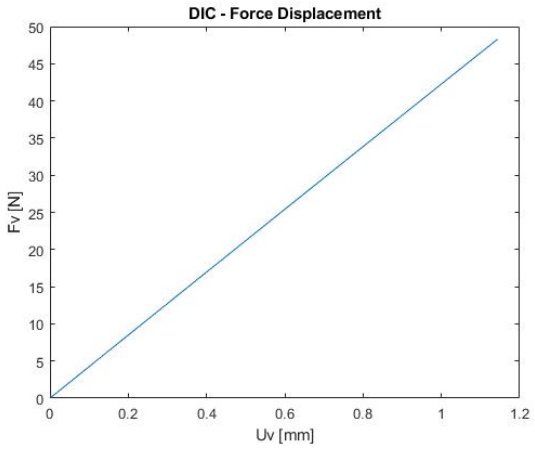

Figure K.11: AG11 - Step 3 - $\gamma = 26.6 deg$. DIC stiffness vertical plot.

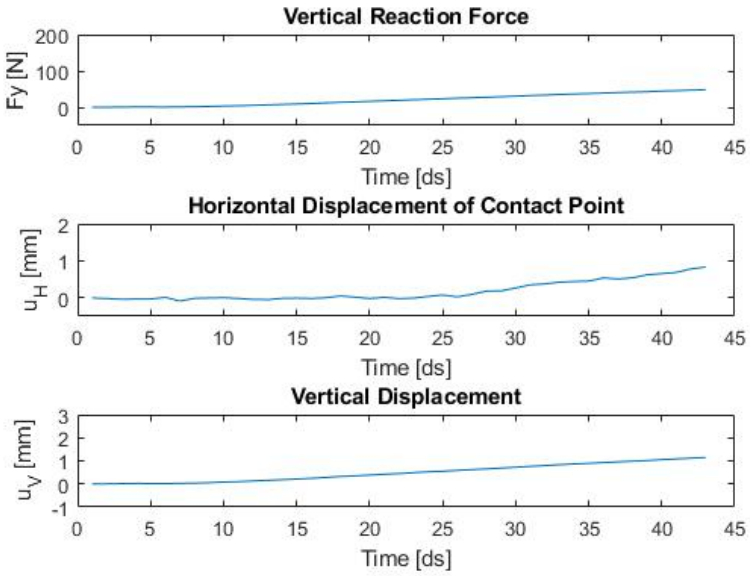

Figure K.12: AG11 - Step 3 - $\gamma = 26.6 deg$. DIC vertical force, horizontal displacement and vertical displacement.

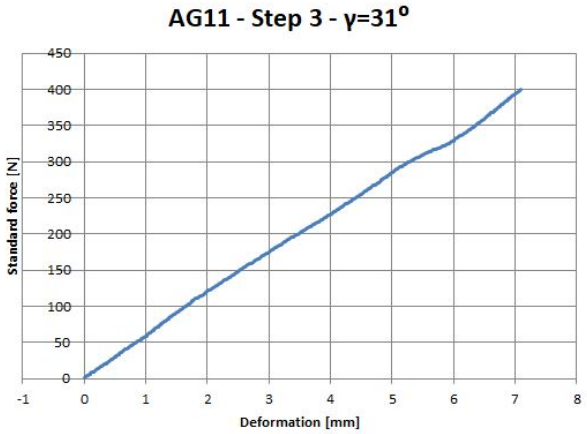

Figure K.13: AG11 - Step 3 - $\gamma = 31 deg$. Test bench vertical stiffness plot.

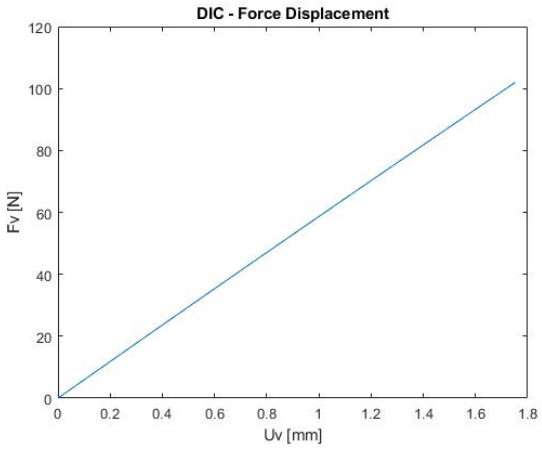

Figure K.14: AG11 - Step 3 - $\gamma = 31 deg$. DIC stiffness vertical plot.

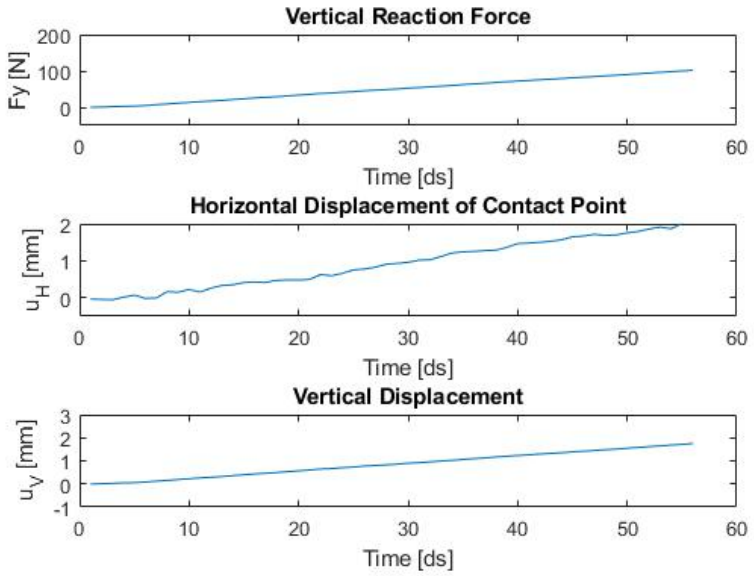

Figure K.15: AG11 - Step 3 - $\gamma = 31 deg$. DIC vertical force, horizontal displacement and vertical displacement.

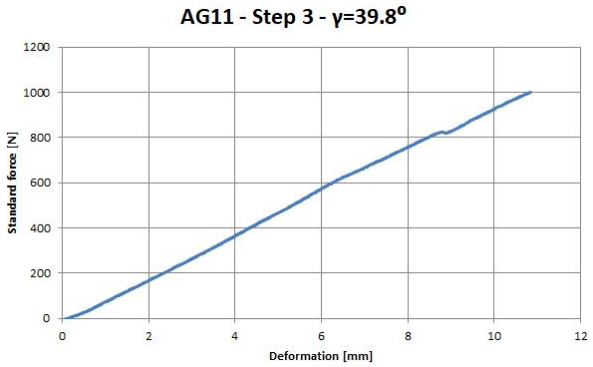

Figure K.16: AG11 - Step 3 - $\gamma = 39.8 deg$. Test bench vertical stiffness plot.

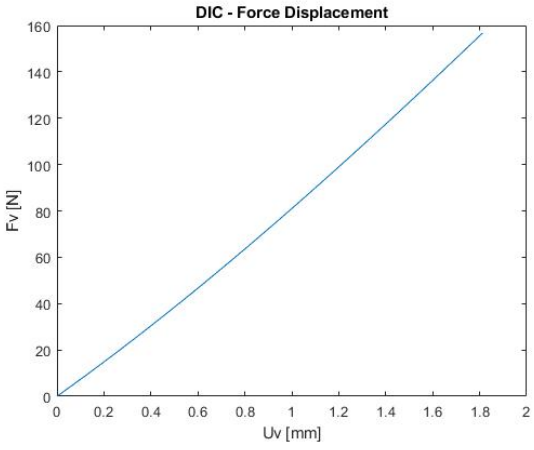

Figure K.17: AG11 - Step 3 - $\gamma = 39.8 deg$. DIC stiffness vertical plot.

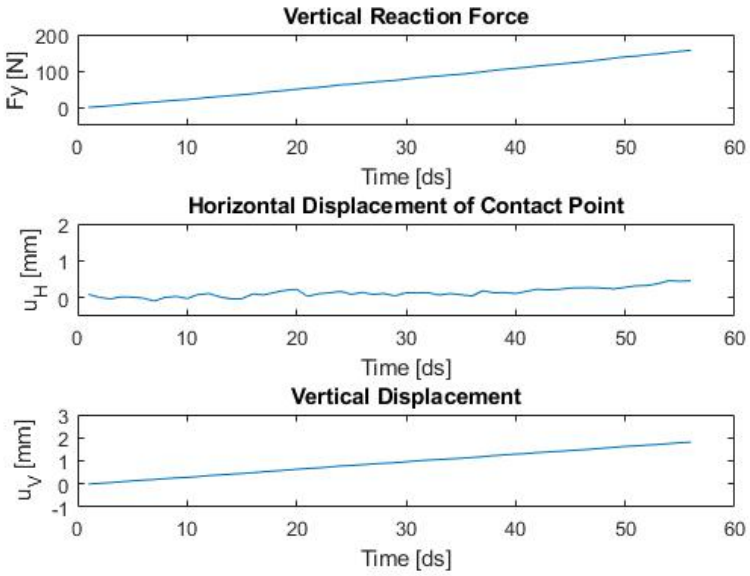

Figure K.18: AG11 - Step 3 - $\gamma = 39.8deg$. DIC vertical force, horizontal displacement and vertical displacement.

Figure K.19: AG11 - Block - $\gamma = 28.8deg$. Test bench vertical stiffness plot.

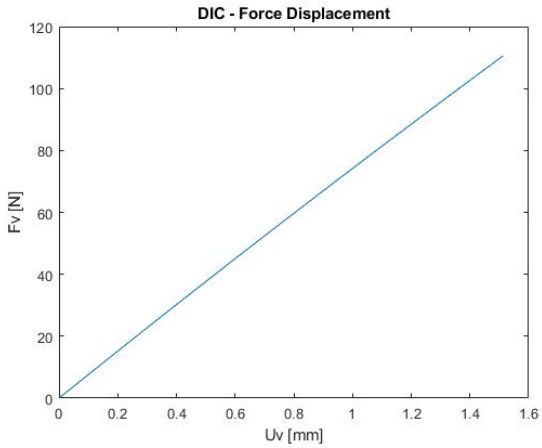

Figure K.20: AG11 - Block - $\gamma = 28.8 deg$. DIC stiffness vertical plot.

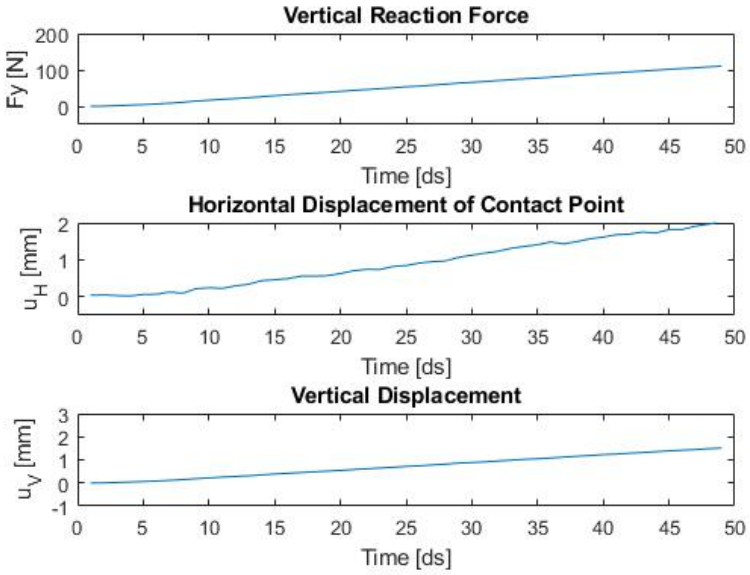

Figure K.21: AG11 - Block - $\gamma = 28.8 deg$. DIC vertical force, horizontal displacement and vertical displacement.

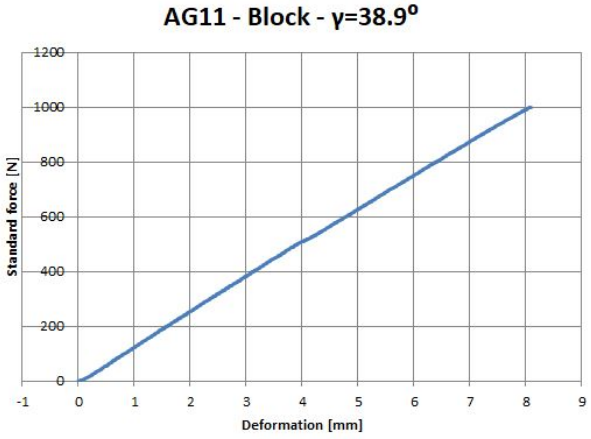

Figure K.22: AG11 - Block - $\gamma = 38.9 deg$. Test bench vertical stiffness plot.

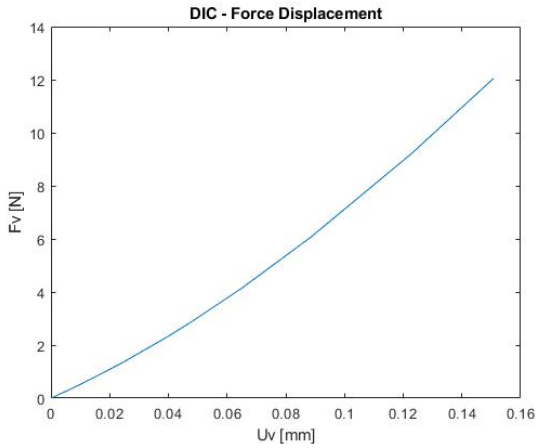

Figure K.23: AG11 - Block - $\gamma = 38.9deg$. DIC stiffness vertical plot.

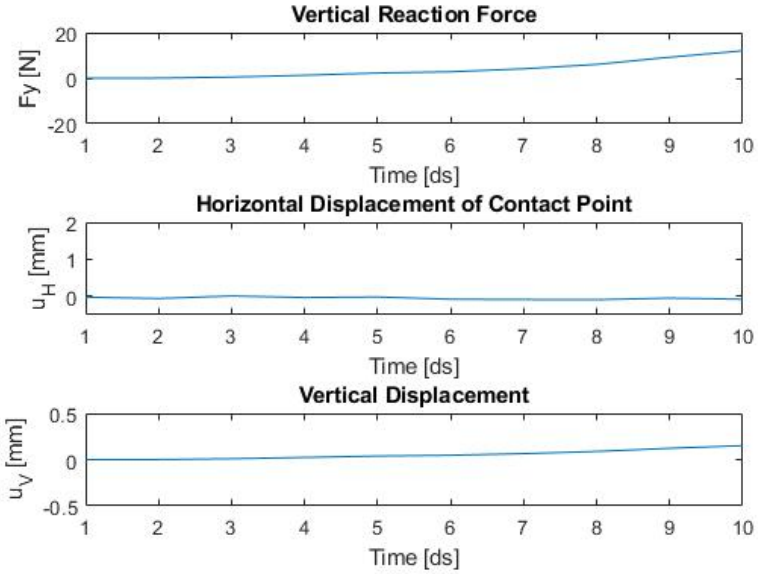

Figure K.24: AG11 - Block - $\gamma = 38.9deg$. DIC vertical force, horizontal displacement and vertical displacement.

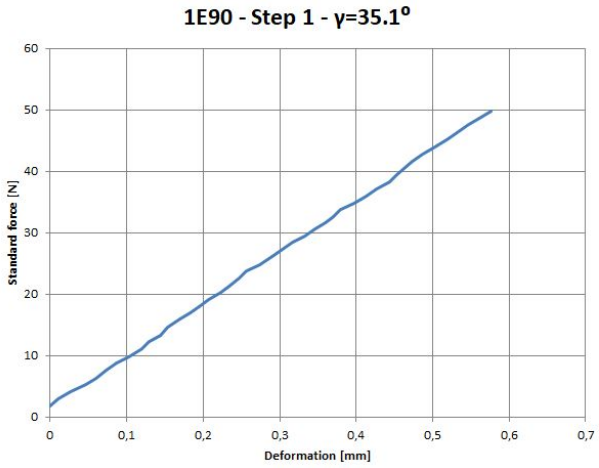

Figure K.25: 1E90 - Step 1 - $\gamma = 35.1 deg$. Test bench vertical stiffness plot.

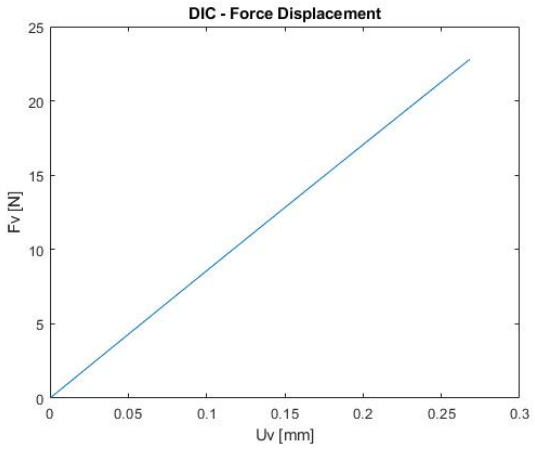

Figure K.26: 1E90 - Step 1 - $\gamma = 35.1 deg$. DIC stiffness vertical plot.

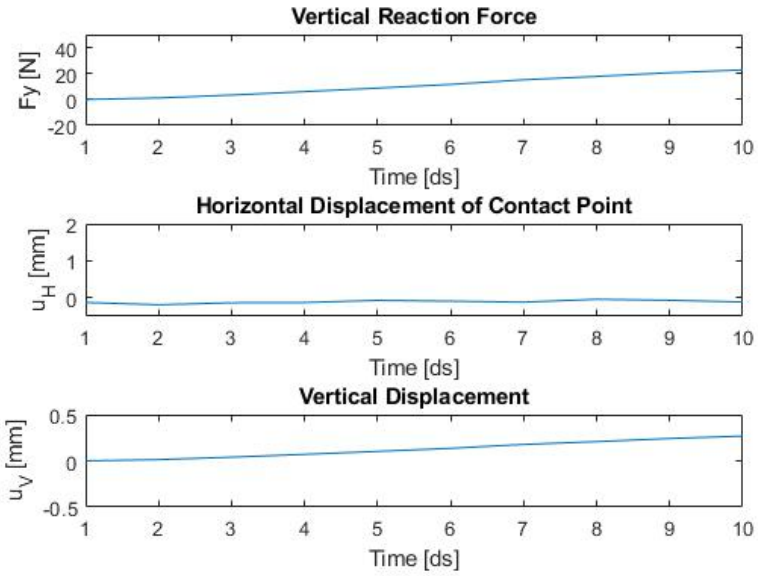

Figure K.27: 1E90 - Step 1 - $\gamma = 35.1 deg$. DIC vertical force, horizontal displacement and vertical displacement.

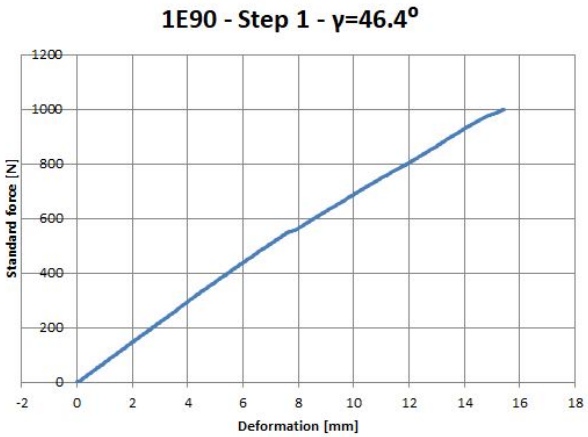

Figure K.28: 1E90 - Step 1 - $\gamma = 46.4 deg$. Test bench vertical stiffness plot.

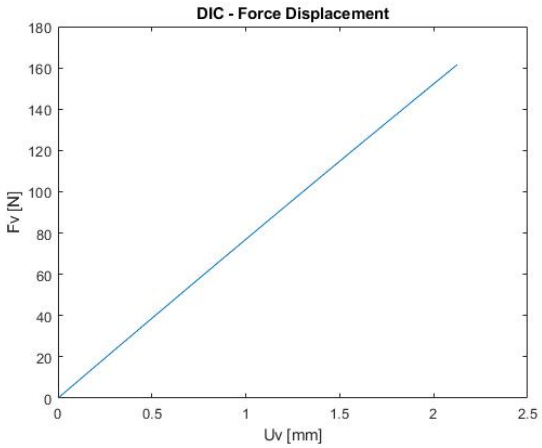

Figure K.29: 1E90 - Step 1 - $\gamma = 46.4 deg$. DIC stiffness vertical plot.

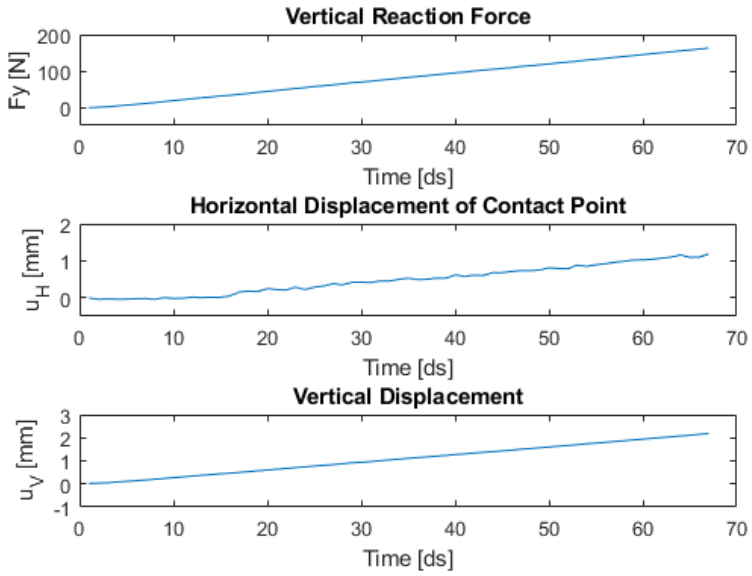

Figure K.30: 1E90 - Step 1 - $\gamma = 46.4 deg$. DIC vertical force, horizontal displacement and vertical displacement.

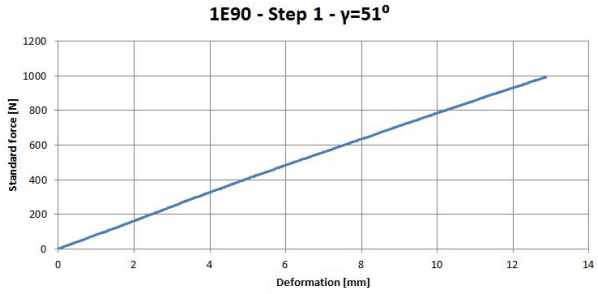

Figure K.31: 1E90 - Step 1 - $\gamma = 51 deg$. Test bench vertical stiffness plot.

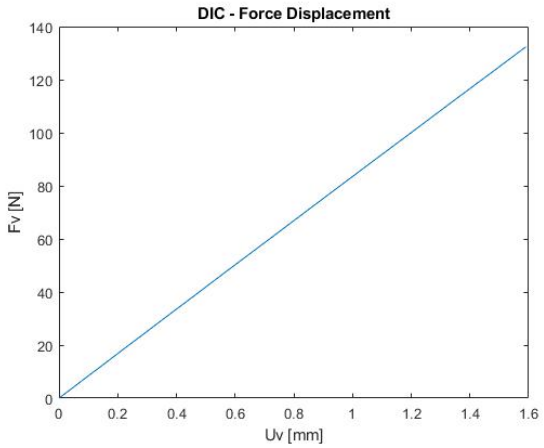

Figure K.32: 1E90 - Step 1 - $\gamma = 51 deg$. DIC stiffness vertical plot.

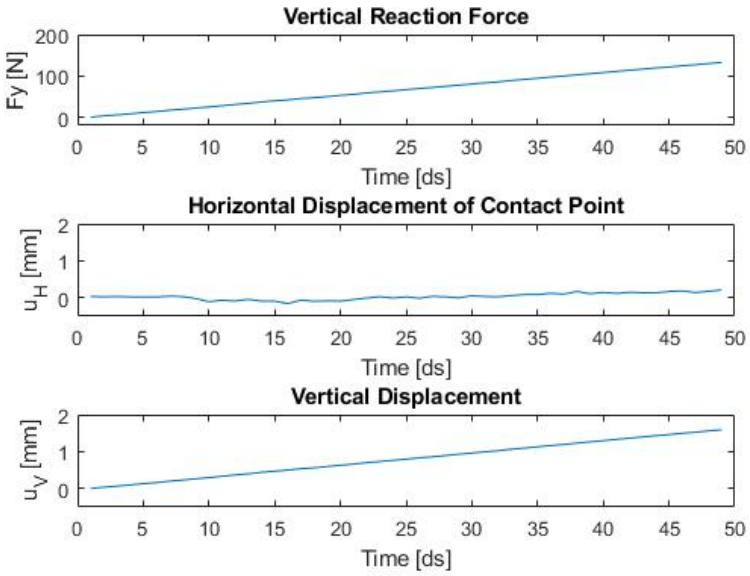

Figure K.33: 1E90 - Step 1 - $\gamma = 51 deg$. DIC vertical force, horizontal displacement and vertical displacement.

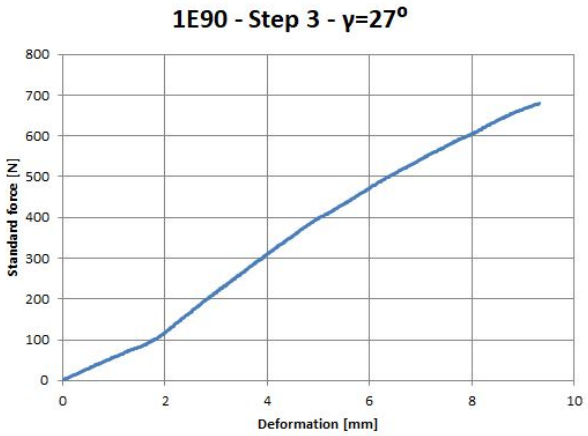

Figure K.34: 1E90 - Step 3 - $\gamma = 27 deg$. Test bench vertical stiffness plot.

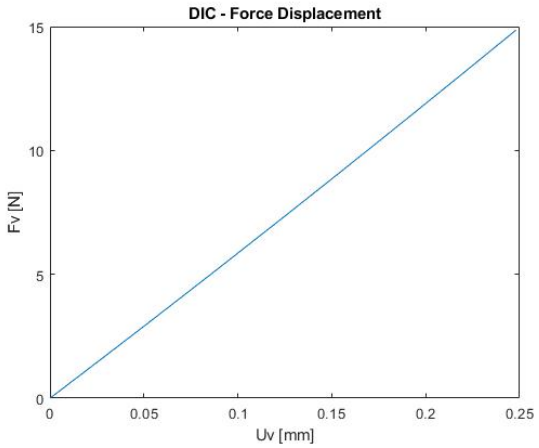

Figure K.35: 1E90 - Step 3 - $\gamma = 27 deg$. DIC stiffness vertical plot.

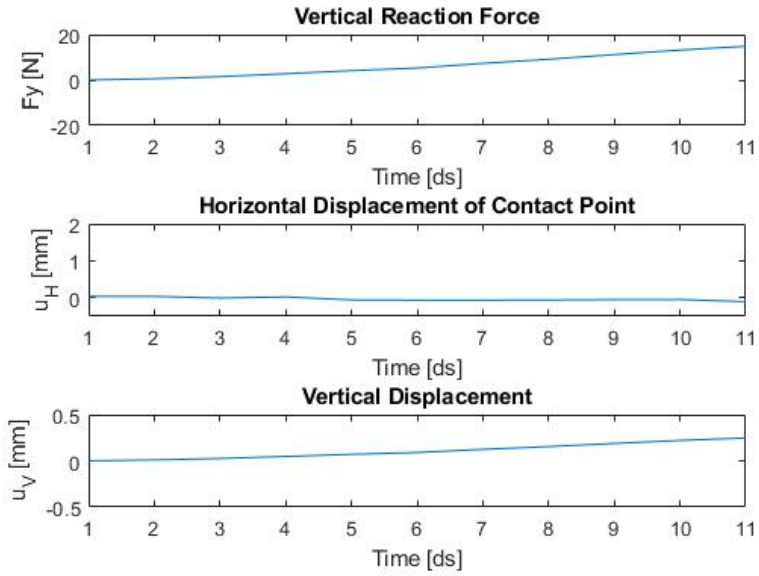

Figure K.36: 1E90 - Step 3 - $\gamma = 27deg$. DIC vertical force, horizontal displacement and vertical displacement.

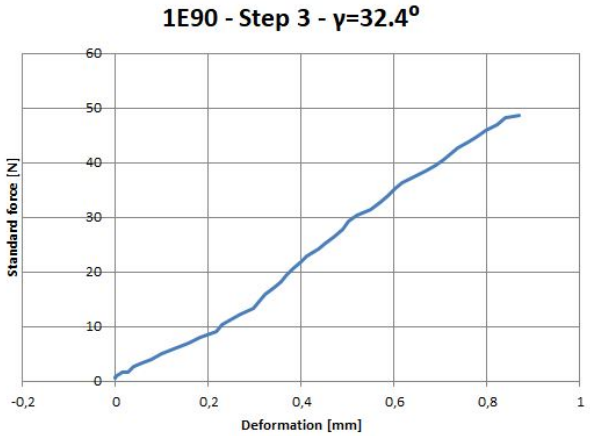

Figure K.37: 1E90 - Step 3 - $\gamma = 32.4deg$. Test bench vertical stiffness plot.

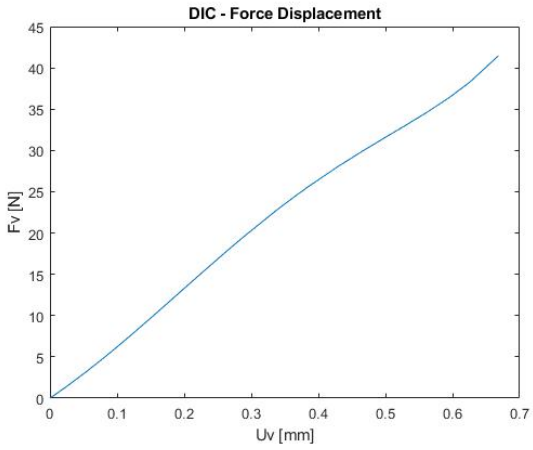

Figure K.38: 1E90 - Step 3 - $\gamma = 32.4deg$. DIC stiffness vertical plot.

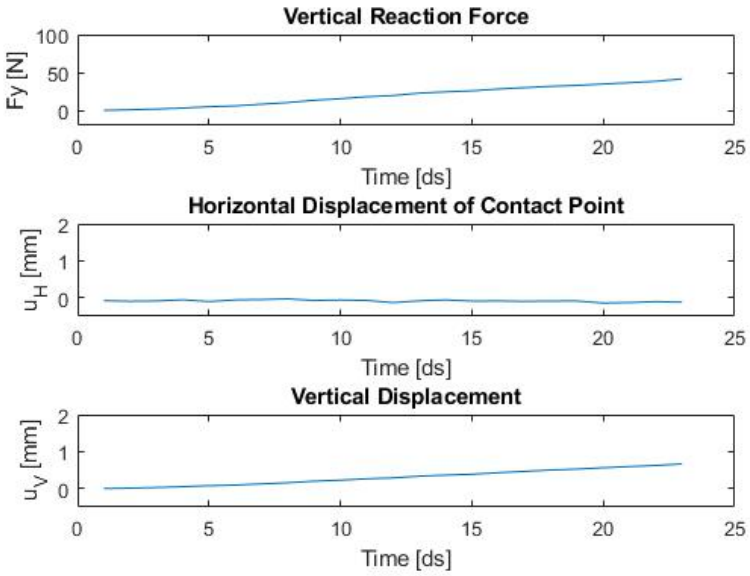

Figure K.39: 1E90 - Step 3 - $\gamma = 32.4 deg$. DIC vertical force, horizontal displacement and vertical displacement.

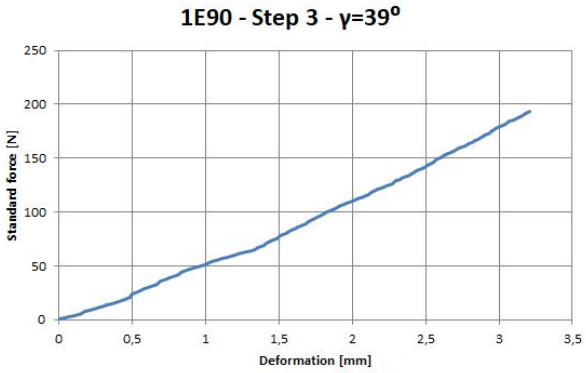

Figure K.40: 1E90 - Step 3 - $\gamma = 39 deg$. Test bench vertical stiffness plot.

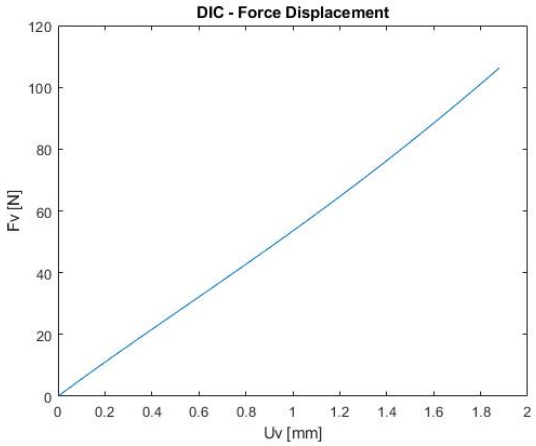

Figure K.41: 1E90 - Step 3 - $\gamma = 39 deg$. DIC stiffness vertical plot.

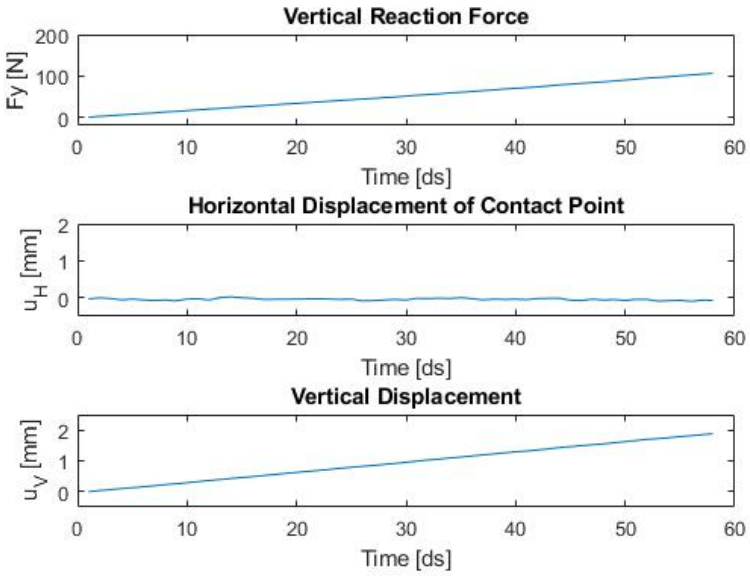

Figure K.42: 1E90 - Step 3 - $\gamma = 39deg$. DIC vertical force, horizontal displacement and vertical displacement.

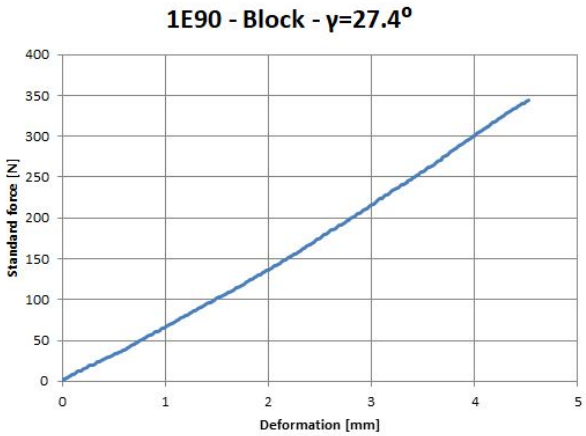

Figure K.43: 1E90 - Block - $\gamma = 27.4deg$. Test bench vertical stiffness plot.

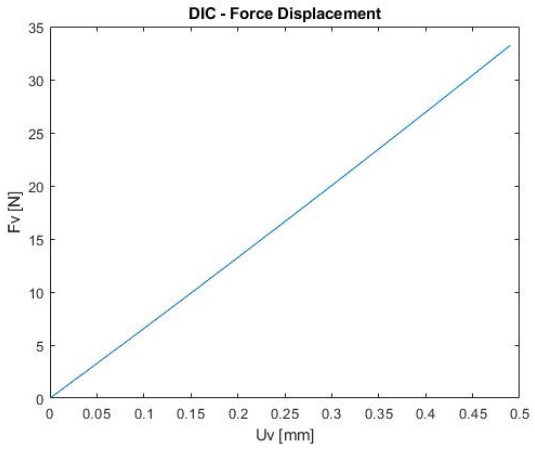

Figure K.44: 1E90 - Block - $\gamma = 27.4deg$. DIC stiffness vertical plot.

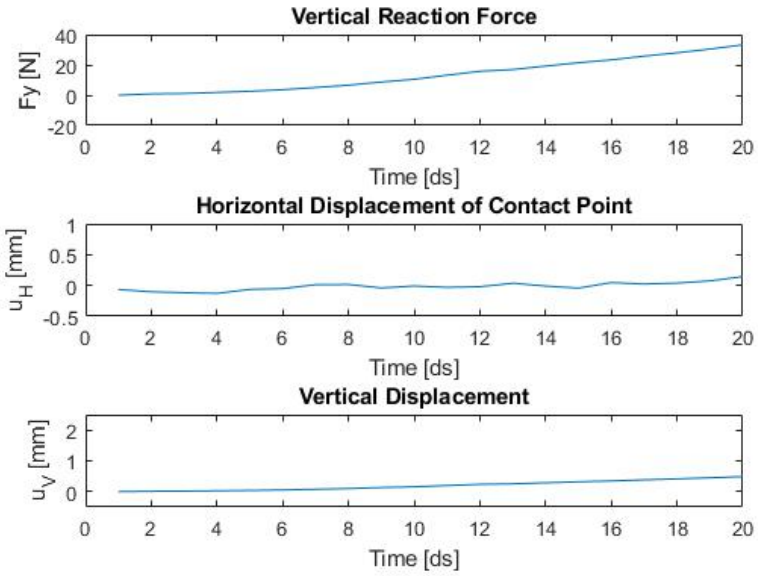

Figure K.45: 1E90 - Block - $\gamma = 27.4deg$. DIC vertical force, horizontal displacement and vertical displacement.

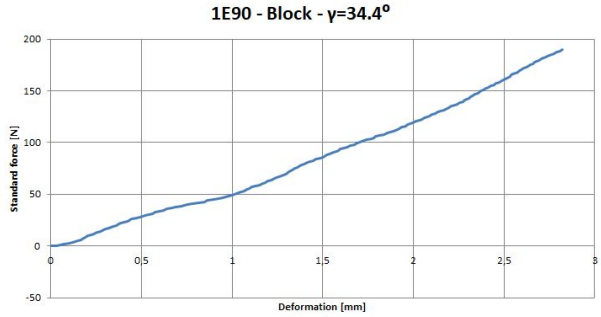

Figure K.46: 1E90 - Block - $\gamma = 34.4deg$. Test bench vertical stiffness plot.

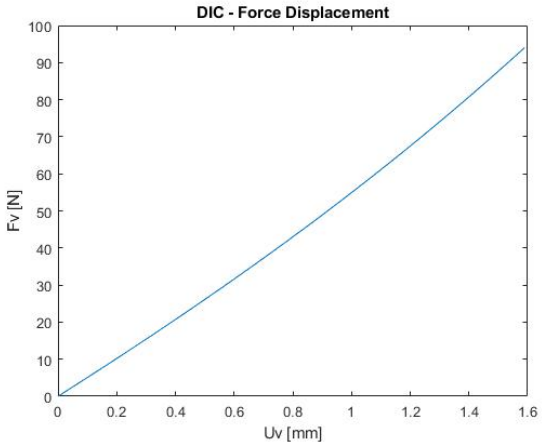

Figure K.47: 1E90 - Block - $\gamma = 34.4deg$. DIC stiffness vertical plot.

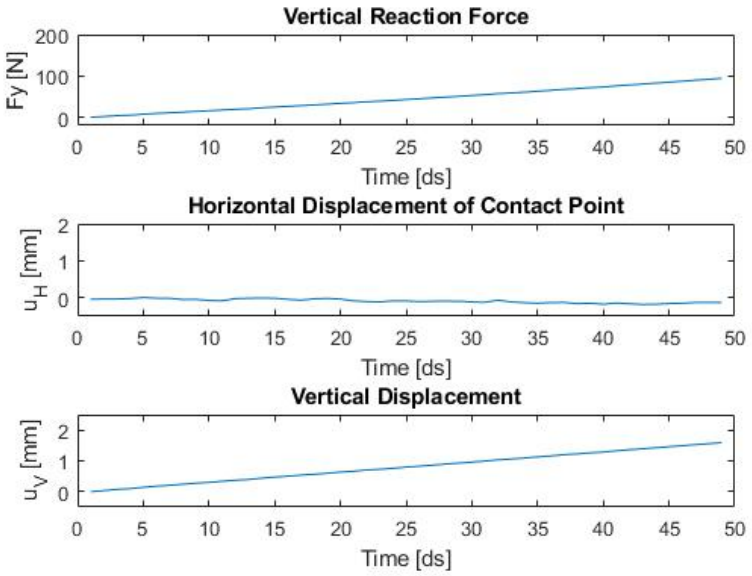

Figure K.48: 1E90 - Block - $\gamma = 34.4 deg$. DIC vertical force, horizontal displacement and vertical displacement.

Figure K.49: 1E90 - Block - $\gamma = 41.8 deg$. Test bench vertical stiffness plot.

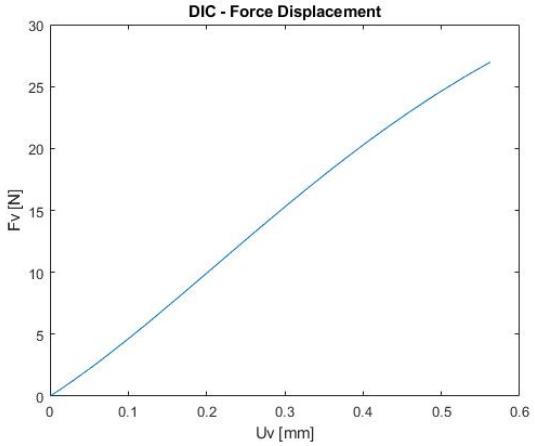

Figure K.50: 1E90 - Block - $\gamma = 41.8 deg$. DIC stiffness vertical plot.

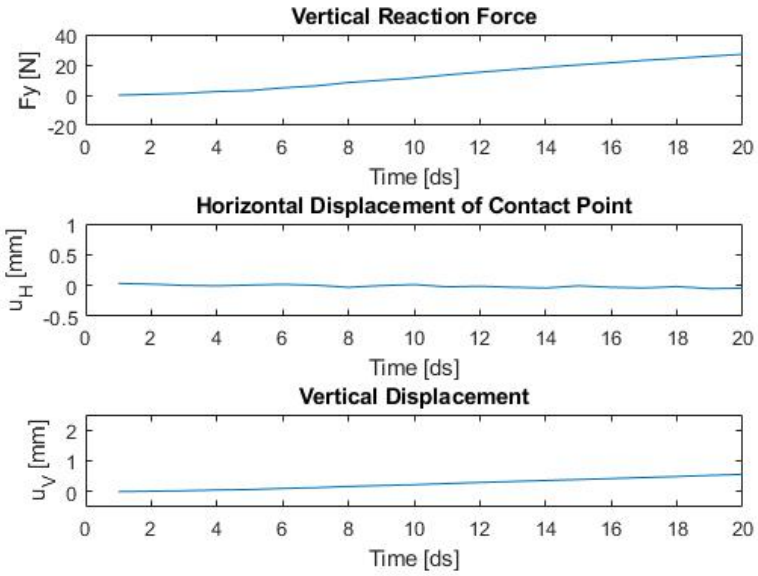

Figure K.51: 1E90 - Block - $\gamma = 41.8 deg$. DIC vertical force, horizontal displacement and vertical displacement.

BIBLIOGRAPHY

[1] L. Nolan, "Carbon fibre prostheses and running in amputees: A review," *European Foot and Ankle Surgery*, vol. 14, no. 3, pp. 125–129, 2008.

[2] J. Keogh, "Paralympic sport: an emerging area for research and consultancy in sports biomechanics," *Sports Biomechanics*, vol. 10, no. 3, pp. 234–253, 2011.

[3] J. Keogh et al., "Paralympic sports, the next frontier for sports science," vol. 1, no. 1, 2010.

[4] A. Grogan, "Paralympic technology," *Engineering and Technology*, vol. 23, no. 1, pp. 11–20, 1997.

[5] H. Hassani, M. Ghodsi, M. Shadi, S. Noroozi, and B. Dyer, "A statistical perspective on running with prosthetic lower-limbs: an advantage or disadvantage?" *J Sports*, vol. 2, pp. 76–84, 2014.

[6] L. Grobler, S. Ferreira, B. Vanwanseele, and E. Terblanche, "Characterisation of the responsive properties of two running-specific prosthetic models," *Prosthetics and Orthotics International*, pp. 1–8, 2016.

[7] C. McGowan, A. Grabowski, W. McDermott, H. Herr, and R. Kram, "Leg stiffness of sprinters using running-specific prostheses," *Journal of the Royal Society Interface*, 2012.

[8] M. Scholz, J. Blanchfield, L. Bloom, B. Coburn, M. Elkington, J. Fuller, M. Gilbert, S. Muflahi, M. Pernice, S. Rae, J. Trevarthen, S. White, P. Weaver, and I. Bond, "The use of composite materials in moderns orthopaedic medicine and prosthetic devices a review," *Composites Science and Technology*, vol. 71, pp. 1791–1803, 2011.

[9] O. B. H. GmBH, *Kurzanleitung für 3S80 Sportprothesen*. Duderstadt, 2014.

[10] K. Maćkala, "Optimisation of performance through kinematic analysis of the different phases of the 100 metres," *New Studies in Athletics*, vol. 2, pp. 7–16, 2007.

[11] M. Krzysztof and A. Mero, "A kinematics analysis of three best 100m performances ever," *J Human Kinetics*, vol. 36, pp. 149–160, 2013.

[12] H. Hassani, M. Ghodsi, M. Shadi, S. Noroozi, and B. Dyer, "An overview of the running performance of athletes with lower-limb amputation at the paralympic games 2004-2012," *J. Sports*, vol. 3, pp. 103–115, 2015.

[13] B. Gajer, C. Hanon, and C. Thepaut-Mathieu, "Velocity and stride parameters in the 400 metres," *New Studies in Athletics*, vol. 3, pp. 39–46, 2007.

[14] K. Mombaur, "A mathematical study of sprinting on artificial legs," *Modeling, Simulation and Optimization of Complex Processes*, pp. 157–168, 2012.

[15] H. Hobara, Y. Kobayashi, and M. Mochimaru, "Spatiotemporal variables of able-bodied and amputee sprinters in men's 100-m sprint," *International J Sports Medicine*, vol. 36, pp. 494–497, 2015.

[16] S. Willwacher, V. Herrmann, K. Heinrich, J. Funken, W. Potthast, and G. Bezodis, I Brüggemann, "Sprint start kinetics: Comparison of amputee and non-amputee sprinters," *PPaper accepted for the presentation at the XXXIII International Conference on Biomechanics in Sports, Portiers, France*, 2015.

[17] P. Taboga, A. Grabowski, P. di Prampero, and R. Kram, "Optimal starting block configuration in sprint running: a comparison of biological and prosthetic legs," *J. Applied Biomechanics*, vol. 30, pp. 381–389, 2014.

[18] S. Willwacher, V. Herrmann, K. Heinrich, J. Funken, G. Strutzenverger, J. Goldmann, B. Braunstein, A. Brazil, G. Irwin, W. Potthast, and G. Brugemann, "Sprint start kinetics of amputee and non-amputee sprinters," *PLoS ONE*, vol. 11, no. 11, 2016.

[19] S. Debaere, C. Delecluse, D. aerenhouts, F. Hagman, and I. Jonkers, "From block clearance to sprint: characteristics underlying an effective transition," *J of Sports Sciences*, vol. 31, no. 2, pp. 137–149, 2013.

[20] G. K. K. Jessica D., Ventura and N. Richard R., "The effect of prosthetic ankle energy storage and return properties on muscle activity in below-knee amputee walking," *Gait and Posture*, vol. 33, p. 220–226, 2011.

[21] G. Brüggemann, Arampatzis, and W. Emrich, F abd Potthast, "Biomechanics of double transtibial amputee sprinting using dedicated sprinting prostheses," *Sports Technology*, vol. 1, no. 4-5, pp. 220–227, 2008.

[22] M. Theodore E. and F. David W., "Characterization of multijoing finger stiffness: Dependence on finger posture and force direction," *IEEE Transactions on Biomedical Engineering*, vol. 45, 1998.

[23] G. Rabita, S. Dorel, J. Slawinski, E. Sàez-de Villarreal, A. Couturier, P. Samozino, and J.-B. Morin, "carbon fibrenics in world-class athletes: a new insight into the limits of human locomotion," *Scandinavian Journal of Medicine and Science in Sports*, vol. 25, pp. 583–594, 2015.

[24] B. Baum, M. Schultz, A. Tian, B. Shefter, E. Wolf, H. Kwon, and J. Shim, "Amputee locomotion: determining inertial properties of running-specific prostheses," *Archives of Physical Medicina and Rehabilitaion*, vol. 94, pp. 1776–1783, 2013.

[25] R. Selles, J. Bussmann, L. Klip, B. Speet, A. Van Soest, and H. Stam, "Adaptations to mass perturbations in transtibial amputees: kinetic or kinematic invariance?" *Archives of Physical Medicine and Rehabilitation*, vol. 85, pp. 2046–2052, 2004.

[26] P. Weyand, M. Bundle, C. McGowan, A. Grabowski, M. Brown, R. Kram, and H. Herr, "The fastest runner of artificial legs: different limbs, similar function?" *J. Applied Physiology*, vol. 107, pp. 903–911, 2009.

[27] M. Harland and J. Steele, "Biomechanics of the sprint start," *Sports Med.*, pp. 28–31, September 2012.

[28] F. Hellebrandt, "Influence of lower extremity amputation on stance mechanics," *JAMA*, vol. 142, no. 17, pp. 1353–1356, 1950.

[29] K. Deurenberg, Pand Bhaskaran and P. Lian, "Singaporean chinese adolescents have more subcutaneous adipose tissue than dutch caucasians of the same age and body mass index," *Asia Pac J Clin Nutr.*, vol. 12, no. 3, pp. 261–265, 2003.

[30] S. Agarwal, S. Zaidi, and S. Agarwal, "Correlation of body height by foot length and knee height measurements in population of north india," *International Journal of Anatomy and Research*, vol. 3, no. 3, pp. 1225–1229, 2015.

[31] A. Baldi, "Analisi di stati di sforzo tridimensionali nei laminati in composito: tecniche numeriche e criteri di rottura," *Tesi di Laurea, Politecnico di Milano*, 2006.